Summer 2023

Design, Modeling and Analysis of an AC-AC Dual Active Bridge Converter

Kartikeya Jayadurga Prasad Veeramraju
Missouri University of Science and Technology

Department: Electrical and Computer Engineering

DESIGN, MODELING AND ANALYSIS OF AN AC-AC DUAL ACTIVE BRIDGE CONVERTER

by

KARTIKEYA JAYADURGA PRASAD VEERAMRAJU

A DISSERTATION

Presented to the Graduate Faculty of the

MISSOURI UNIVERSITY OF SCIENCE AND TECHNOLOGY

In Partial Fulfillment of the Requirements for the Degree

DOCTOR OF PHILOSOPHY

in

ELECTRICAL ENGINEERING

2023

Approved by:

Dr. Jonathan W. Kimball, Advisor
Dr. Mehdi Ferdowsi
Dr. Pourya Shamsi
Dr. Maciej Zawodniok
Dr. Jonghyun Park

PUBLICATION DISSERTATION OPTION

This dissertation consists of the following three journal articles, formatted in the style used by the Missouri University of Science and Technology.

Paper I: A Single-Stage Bidirectional Soft-Switching AC-AC Converter Based on Dual Active Bridge Topology with Integrated Magnetics, found on Pages 6 – 37, is intended for submission to the *IEEE Transactions in Power Electronics*.

Paper II: An Extended Generalized Average Modeling Framework For Power Converters, found on Pages 38 – 69, has been published in the *IEEE Transactions in Power Electronics*.

Paper III: Dynamic Model Of Ac-ac Dual Active Bridge Converter Using The Extended Generalized Average Modeling Framework, found on Pages 70 – 91, is intended for submission to the *IEEE Transactions on Power Electronics*.

ABSTRACT

The Solid-State Transformer (SST) is gaining attention as an alternative to conventional iron-core transformers in the power electronic community. The power industry's increasing demands for smaller size, higher efficiency, and greater energy density have made the SST an attractive option. Among various power electronic converter topologies, the Dual Active Bridge (DAB) has become popular for its bidirectional power flow capability and galvanic isolation, primarily in the DC application space. Advancements in semiconductor technologies have introduced new bidirectional switches, opening avenues for novel SST topologies. This research investigates the application of the DAB as a single-stage SST and focuses on advancements in modeling, design, and control for ac-ac applications. Analytical expressions for phase shifts are derived, leading to the formulation of a design rule. Additionally, a real-time DSP based soft-switching algorithm is developed to meet the primary requirement of high-efficiency designs. The integration of DAB inductance in the transformer enhances energy density. However, dynamic modeling of the ac-ac DAB converter poses challenges, as it exhibits two distinct excitation frequencies that current modeling methods cannot adequately capture. To address this, an improved version of the Generalized Averaged Modeling (GAM) technique, called Extended-GAM (EGAM), is introduced. EGAM incorporates the multiplication of Double Fourier Series (DFS) signals, enabling the capture of multiple harmonics in converter dynamics. The algorithm is validated through harmonic truncation observations and a case study involving a single-phase inverter with LC filters. The EGAM technique is successfully applied to the ac-ac DAB converter, effectively handling its dynamic behavior and overcoming challenges posed by switching terms. Extensive simulations and hardware experiments validate the accuracy and effectiveness of the proposed EGAM modeling approach. These advancements contribute to precise modeling, efficient power flow control, and enhanced design of the ac-ac DAB converter, showcasing its potential as a Solid-State Transformer.

ACKNOWLEDGMENTS

I want to extend my sincere gratitude to Dr. Jonathan Kimball for allowing me to work and learn under his tutelage and for helping me acquire invaluable insights into power electronic design. I profoundly thank Dr. Mehdi Ferdowsi, Dr. Pourya Shamsi, Dr. Maciej Zawodniock, and Dr. Jonghyun Park for accepting to be my committee members.

Special thanks to Angshuman for always motivating me to excel. I also thank my labmates Alvaro, Arnold, and Oboreh for all their wonderful collaborative efforts. None of my accomplishments would have been possible if not for the encouragement of my parents, Dr. Yasodhara Veeramraju and Dr. Somasekhar Veeramraju. It would have been three excruciatingly tight years hadn't it been for your unwavering support and scientific enthusiasm.

I would like to thank the DOE Office of Electricity Energy Storage Program and Dr. Imre Gyuk for their generous financial support. Dr. Stan Atcitty and Dr. Jacob Mueller played an instrumental role in envisioning the AC-AC Dual Active Bridge project. This material is based upon work supported by the Department of Energy Vehicle Technologies Office under Award Number DE-EE0008449. This dissertation was prepared as an account of work sponsored by an agency of the United States Government. Neither the United States Government nor any agency thereof, nor any of their employees, makes any warranty, express or implied, or assumes any legal liability or responsibility for the accuracy, completeness, or usefulness of any information, apparatus, product, or process disclosed, or represents that its use would not infringe privately owned rights. Reference herein to any specific commercial product, process, or service by trade name, trademark, manufacturer, or otherwise does not necessarily constitute or imply its endorsement, recommendation, or favoring by the United States Government or any agency thereof. The views and opinions of the author expressed herein do not necessarily state or reflect those of the United States Government or any agency thereof.

TABLE OF CONTENTS

Page

SECTION

LIST OF ILLUSTRATIONS

Figure Page

SECTION

PAPER I

PAPER II

PAPER III

LIST OF TABLES

SECTION

1. INTRODUCTION

Generation, transmission and distribution are the three main functions in power system engineering. The proliferation of ac power systems can be attributed to transformers that make it possible to transmit large amounts of power through long-range transmission lines at high voltages, thereby leading to lower losses than a pure dc system. Conventional transformers operating at 60 Hz and higher power levels are often bulky and serve one purpose: transforming voltages. All the power converters interfacing with the transformer must finally interface to the transformer at 60 Hz and therefore must be designed as such. Transformers are also heavy and bulky to produce and transport. They are also challenging to set up in offshore transmission applications, increasing installation, maintenance, and assembly costs.

However, conventional transformers that operate at grid frequencies have very high efficiencies due to the simplicity of operation, mature low-frequency transformer design technology, and the absence of switching devices. The efficiency of a typical distribution level transformer can be as high as 99.5% [1], which is well above the specification of 97% [3] for distribution levels.

With the rapid progression of renewable energy sources, more and more connections are being made to the grid. Given the scale of the power being integrated, large transformers will be necessary for power integration. Therefore, it becomes infeasible to integrate grid frequency level transformers in remote locations. Therefore high power-dense solutions are desired. For the distribution level, reliable and straightforward circuit topologies are desired.

These inadequacies of conventional transformers give rise to the necessity of Solid State Transformers (SST). SSTs are becoming prevalent as the requirements for power distribution systems increase [1].

A comprehensive review on the design and challenges of SST [1, 4, 5, 6] classifies SST's into four broad categories, viz Type A (Figure 1.1), Type B (Figure 1.2), Type C (Figure 1.2), and Type D (Figure 1.3). Types B and C differ depending on whether the isolation is on low voltage or the high voltage side. Type D SSTs are generally used when LVDC and HVDC are both required.

Type A category of SSTs [7, 8, 9, 5, 10, 11, 12, 13] are generally simpler in construction and interface two ac grids without an intermediate dc link. A matrix converter type topology is proposed in [9], where 54 switches are needed for three-phase power flow regulation and control. This can lead to increased losses in the SST. As SSTs are required to have efficiencies in the ranges of 95%-98% [1], it can be difficult to reach these ranges with a higher number of switches. Novel three-phase topologies employing DABs are proposed to counteract the issue of higher switch counts[10, 14, 7, 11].

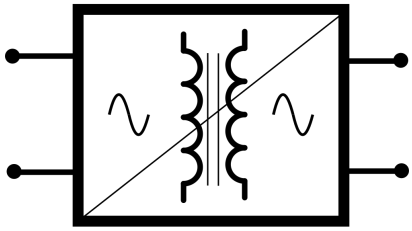

Figure 1.1. Type A SST [1]

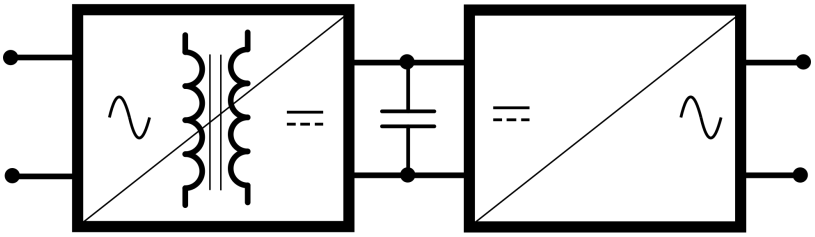

Figure 1.2. Type B and C SST[1]

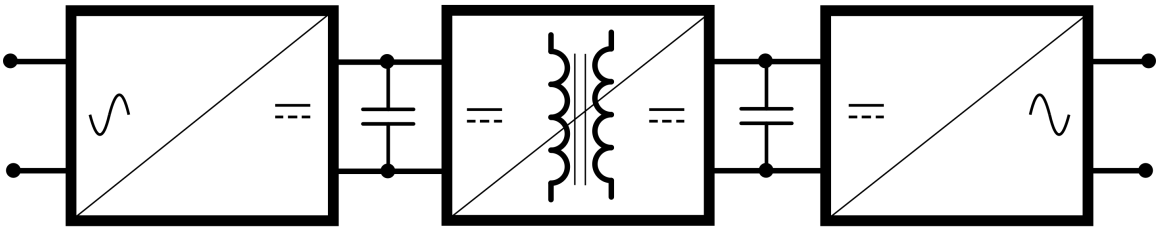

Figure 1.3. Type D SST[1]

1.1. RELIABILITY OF SSTS

SSTs installed on site are subjected to a range of temperatures and levels of humidity. Other types of stressors on the components are mechanical vibrations, pollution, lightning, radiation, and EMI. Among all these stressors, the industry widely believes temperature and humidity to be the most prominent stressors [2].

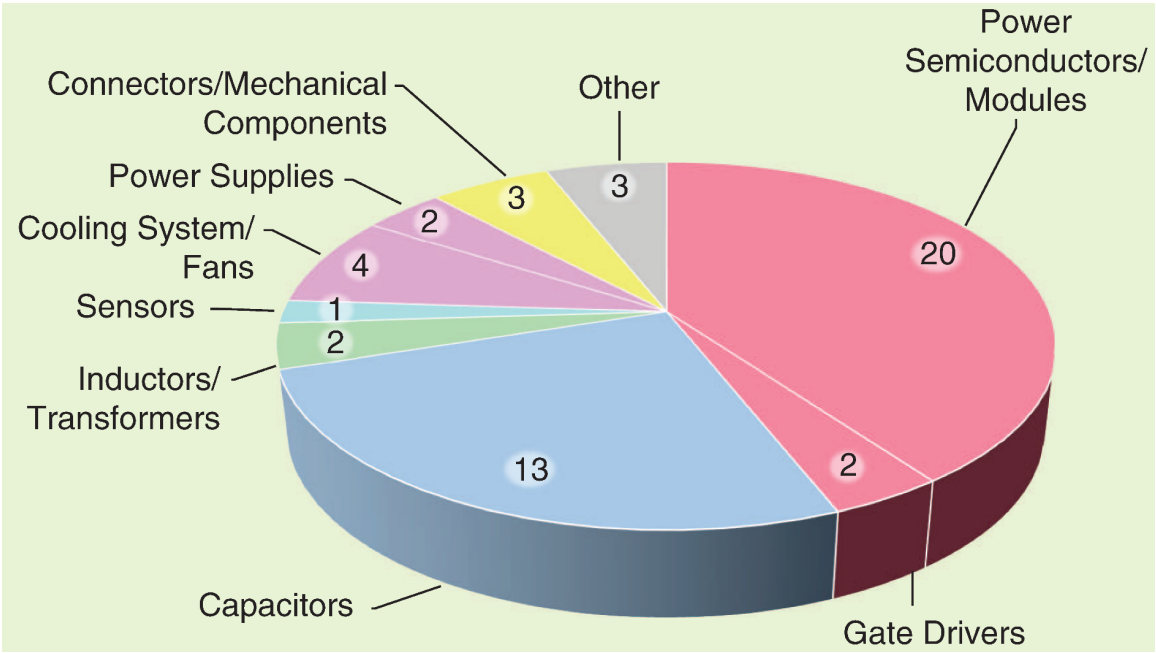

Figure 1.4. Industrial survey on components for reliability improvement [2]

An industry-wide survey on various components used in power electronic hardware was also conducted [2]. In the survey, semiconductor devices and capacitors were identified as the two major sources of reliability issues and where further research and development

were necessary. A breakdown of various components that need reliability hardening and improved lifetimes from an industrial perspective is given in Figure 1.4. The capacitor is seen to be the second most crucial component that needs improvement.

In conventional SSTs, an intermediate dc link is necessary to integrate more sources and allows reactive power compensation. The addition of storage also becomes relatively easy. The dc-link is buffered using a capacitor that serves the function of storage and also as a current filter. However, due to the increased reliability issues of capacitors, dc links may not be viable for integration in future SSTs that replace transformers at the distribution level. Therefore, other alternative topologies for SSTs must be pursued.

1.2. THE AC-AC DUAL ACTIVE BRIDGE TOPOLOGY

To address some of the issues mentioned before, an ac-ac Dual Active Bridge (DAB) converter is researched in this work. The DAB converter is already very popular in the dc application space and has been found to be useful wherever high power transfer is desired while also having galvanic isolability and bidirectional power flow capability. The converter was in fact also pursued in an ac-ac format [15, 16]. However, such a DAB was only implemented for unidirectional power flow capacity in the past. Additionally, the reactive power flow is also implemented in one direction. However, a conventional transformer can have bidirectional power flow and bidirectional active and reactive power flow. These research gaps are pursued in this work. Also, soft switching mechanisms for power flow control for the resulting power flow mechanisms are pursued, and a real-time implementable algorithm is developed for use in Digital Signal Processors (DSPs). The high-frequency switchmode transformer used in this converter also needs good justifications for high frequencies, which must be diligently pursued. Therefore, an integrated leakage inductance-based design methodology with proper flux-spectrum analysis is done in this work. All these aforementioned objectives form the first leg of this work.

The second leg of this work focuses on developing a mathematical framework capable of effectively capturing the dynamics of such converters. This modeling framework is called the Extended Generalized Average Modeling (EGAM) technique and will be explained in the next section.

1.3. EXTENDED GENERALIZED AVERAGE MODELING

The generalized Average Modeling (GAM) technique is an advanced extension of the state space averaging technique. It is useful in scenarios where the small ripple approximation does not hold for state variables. The conventional Generalized Average Model [17, 18] framework models the time evolution of Fourier coefficients of state variables instead of the state variable itself.

However, conventional GAM is insufficient in describing the operation of systems excited by two distinct fundamental frequencies. Therefore a newly proposed construct for GAM [19] for two frequencies is first considered and is built upon to emulate the large signal operation of an inverter system successfully and is described. This extended GAM technique [20] is useful in further describing the dynamics of two frequency excited systems such as the ac-ac DAB, which is excited by both grid level and switching level harmonics.

Therefore equipped with the newly proposed EGAM technique, an inverter with two LC filters on the input and output side is used and validated in the second work. The EGAM technique is also used to model the dynamics of the ac-ac DAB converter in the third work.

1.4. ORGANIZATION OF THE DISSERTATION

This dissertation is organized as follows: The ac-ac DAB converter is first investigated for both active and reactive power flow mechanisms along with soft switching and transformer design aspects. Following this, the EGAM formulation is proposed in Section 3, where an inverter is tested. Finally, the EGAM framework is used to model the dynamics of an ac-ac DAB in the last Section.

PAPER

I. A SINGLE-STAGE BIDIRECTIONAL SOFT-SWITCHING AC-AC CONVERTER BASED ON DUAL ACTIVE BRIDGE TOPOLOGY WITH INTEGRATED MAGNETICS

Kartikeya Jayadurga Prasad Veeramraju, Angshuman Sharma, Alvaro Cardoza and Jonathan W. Kimball
Department of Electrical and Computer Engineering
Missouri University of Science and Technology
Rolla, MO 65401 USA
Email: kvkhh@mst.edu, asc4v@mst.edu, kimballjw@mst.edu

ABSTRACT

An ac-ac Dual Active Bridge (DAB) as a Solid State Transformer (SST) is investigated for active and reactive power flow. Analytical expressions for the required phase shifts in open-loop operation are derived. The inductance of the DAB and switching frequency are critical parameters in the design of DAB as an SST, and a design rule is formulated based on the derived results. A real-time soft-switching algorithm is proposed in order to enable ZVS and ZCS of the bidirectional switches for positive and negative voltage regions. It is shown that the transformer flux's grid frequency component is negligible compared to switching frequency components, enabling high-frequency design. The transformer is designed such that the required DAB inductance is integrated as leakage inductance in the transformer leading to a higher energy density design. It is also shown that the transformer core losses in the ac-ac DAB topology are significantly lesser than the ac-dc-dc-ac counterpart. Finally, a SOGI-PLL-based power flow control strategy is proposed for meeting the real and reactive power demands between two grids with the integrated soft-switching algorithm. The design is validated using simulations and experimental hardware.

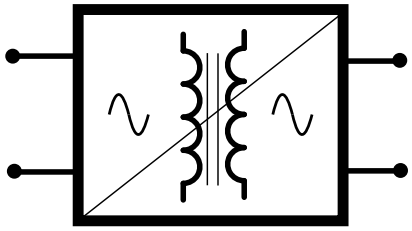

Figure 1. Type A SST [1]

Keywords: Dual Active Bridge Converter, Solid-State Trans- former (SST), Renewable Energy Integration, Microgrids, Power Electronic Transformer, AC distribution systems, soft-switching, Bidirectional switches.

1. INTRODUCTION

Solid State Transformers (SST) are becoming prevalent as the stability and power requirements for power distribution systems increase [1]. For distribution level, reliable and straightforward circuit topologies are desired. A comprehensive review of the design challenges of SST can be found in [1, 2, 3, 4]. SST's can be classified into four broad categories, viz Type A (Figure 1), Type B (Figure 2), Type C (Figure 2), and Type D (Figure 3). Types B and C differ depending on whether the isolation is on the low-voltage or high-voltage side. Type D SSTs are generally used when both low-voltage and high-voltage dc are required.

Type A category of SSTs [5, 6, 7, 3, 8, 9, 10] are generally simpler in construction and interface two ac grids without an intermediate dc link. A matrix converter-type topology is proposed in [7], where 54 switches are needed to realize a three-phase power flow. However, reaching a 95 – 98 % efficiency in this SST can be very challenging due to the high switch count [1]. Some other three-phase topologies employing DABs are also proposed in [8, 11, 5, 9] to reduce the switch count.

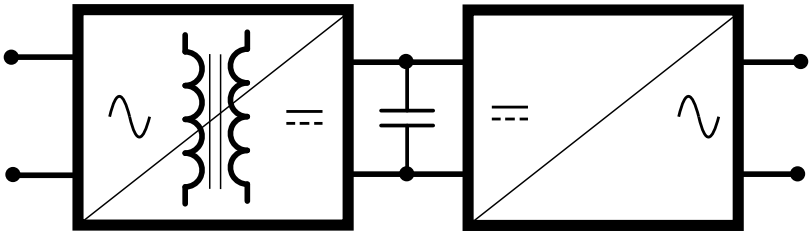

Figure 2. Type B and C SST[1]

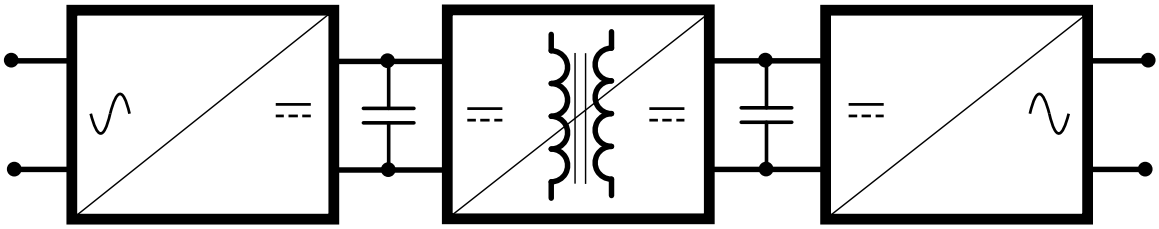

Figure 3. Type D SST[1]

Type B, C [12, 13] and D [14, 15, 16] SSTs are classified as cascaded-type architectures and often employ an ac-dc-ac or ac-dc-dc-ac stages. Type B and C SSTs differ in two ways. In Type B SST, the isolated side sees a high-voltage ac while the dc-link sees a low-voltage dc, which is further inverted. On the other hand, in Type C SST, the isolated side sees a low voltage ac while the dc link sees a high voltage dc, which is further inverted [1]. The availability of dc-link makes these classes of SSTs versatile and facilitates the integration of renewable resources operating at different voltage levels but it also poses challenges due to the higher number of power stages and corresponding circuit complexity [17]. Type A SSTs do not have a dc-link and, therefore, cannot meet reactive power demands [1]. However, this article presents a phase modulation scheme for Type A SSTs that can meet the reactive power demand on an instantaneous power reproduction basis.

A Type A SST in a DAB configuration referred to as the ac-ac DAB in this article is shown in Figure 4 [18, 17, 19, 6]. This particular topology is an attractive alternative to the cascaded converter architecture [17, 18, 1] because of the following:

- fewer passive components

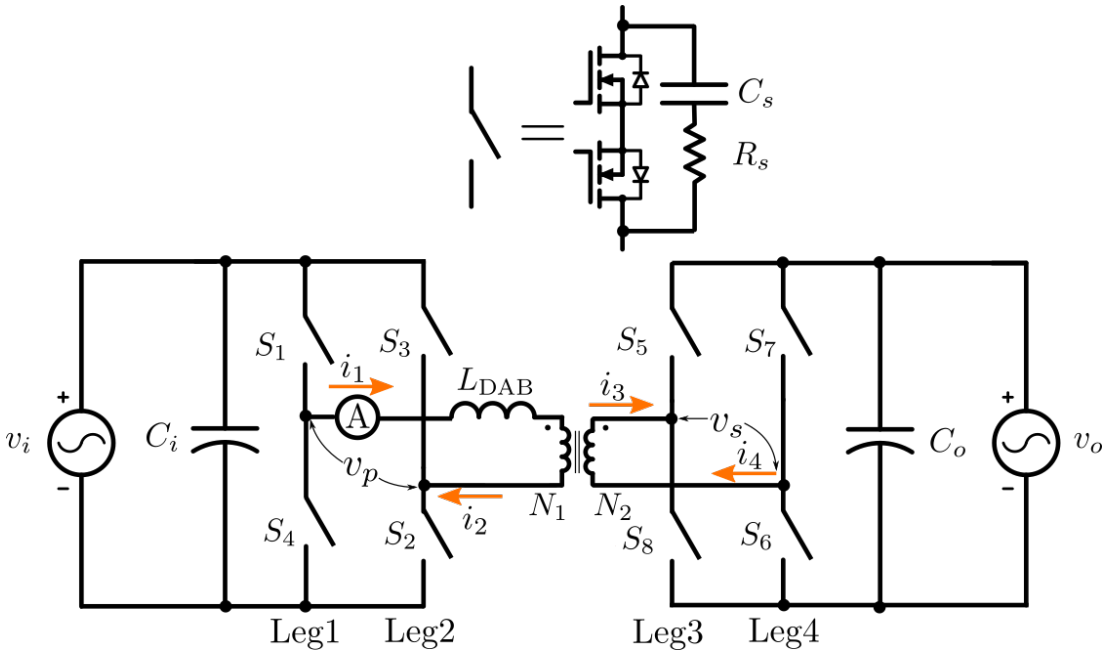

Figure 4. ACAC Dual Active Bridge Converter Schematic

- better reliability
- smaller footprint and lower cost
- soft-switching capability
- higher efficiency
- bidirectional active and reactive power flow capability
- higher safety from galvanic isolation between grids.

Although ac-ac DABs have been used before [17, 18, 2], the bidirectional reactive power flow mechanism in these converters has seldom been studied. Consequently, the challenges of realizing soft-switching in these converters are yet to be explored to allow an efficient implementation on hardware processors [17, 20]. In this article, a novel single current sample-based switching algorithm is proposed to target soft-switching in an ac-ac DAB. A full analysis and description of the switching sequences to handle both soft-switching

and hard-switching cases are necessary. Finally, the nature of flux in the transformer employed in an ac-ac DAB has not been investigated. This article analyzes the flux spectrum and shows that the transformer can be designed using the already-known high-frequency design methods for transformers. Additionally, it is shown that the transformer in the ac-ac DAB incurs significantly lower core losses than the Type B, C, and D counterparts.

Switches S_1-S_4 comprise the primary bridge and S_5-S_8 comprise secondary side bridge. Each of the switches is a four-quadrant switch [21] with anti-series connected solid-state switches. Two power quality conditioning capacitor filters denoted by C_{in} on the input side and C_{out} on the output side before the switching bridges ensure voltage waveforms are sinusoidal.

The High-Frequency Transformer (HFT) provides the isolation and voltage boost/buck actions to interface two different voltage grids. N_1 and N_2 are the HFT primary and secondary turns, respectively. The DAB inductance L_{DAB} serves as a critical parameter in enabling the power transfer between both bridges. The importance of L_{DAB} is presented in more detail in the subsequent sections. The ac-ac DAB topology can utilize additional snubber capacitors across each of the switches to enable Zero Voltage Switching (ZVS)/ Zero Current Switching (ZCS) schemes at the switching edges.

In Section 2, the analytical expressions for real and reactive power in instantaneous power formulation are given, followed by the power relationships of the ac-ac DAB. With the use of the fundamental power relationships, the DAB phase solutions are derived for realizing a demanded apparent power. Following this, a soft-switching analysis and a real-time switching algorithm are proposed in Section 3. The DAB's inductance is integrated into the transformer, whose design is outlined in Section 4. Finally, the results of a hardware implementation for the ac-ac DAB are presented in Section 5.

2. NATURE OF PHASE FOR DEMANDED POWER

In this section, the power expression for an ac system is first given, and the solutions of the phase angle of the ac-ac DAB are derived from realizing the instantaneous power waveform.

2.1. MATHEMATICAL EXPRESSION OF INSTANTANEOUS POWER

Assuming the current and voltage to be simusoidal at the grid frequencies with RMS values equal to V_{RMS} and I_{RMS}, respectively, the voltage and current for a power factor angle of θ are written as

$$v_i(t) = V_{\text{RMS}}\sqrt{2}\cos(\omega_o t) \tag{1}$$

$$v_o(t) = V_{\text{RMS}}\sqrt{2}\cos(\omega_o t) \tag{2}$$

$$i(t) = I_{\text{RMS}}\sqrt{2}\cos(\omega_o t - \theta) \tag{3}$$

The instantaneous power for a given value of active power P and reactive power Q for a grid angular frequency ω_o is given by

$$p(t) = P\{1 + \cos(2\omega_o t)\} + Q\sin(2\omega_o t) \tag{4}$$

2.2. PHASE SOLUTIONS

A schematic of an ac-ac DAB is shown in Figure 4, and the composite switch configuration is also represented. The instantaneous power flow equation [17] for an ac-ac DAB is given by

$$p(t) = \frac{v_i(t)v_o(t)}{\omega_{sw}NL_{\text{lk}}}\left(|\phi| - \frac{\phi(t)^2}{\pi}\right)\text{sgn}(\phi(t)) \tag{5}$$

ϕ is the phase shift between primary and secondary side square waves, N is the transformer turns ratio, $v_i(t)$ is the input voltage, $v_o(t)$ is the output voltage. The $|\phi|$ and sign operators are used to account for the bidirectional nature of the DAB converter. The power equation (5) can be rearranged to get a quadratic equation in ϕ for an instant of required power $p(t)$ and $X_{\text{DAB}} = \omega_{sw} L_{\text{DAB}}$ for a switching angular frequency of $\omega_{sw} = 2\pi f_{sw}$ for the switching frequency of f_{sw} to give

$$\frac{\phi(t)^2}{\pi} - \mid \phi(t) \mid + \left| \frac{p(t) X_{\text{DAB}}}{v_i(t) \cdot v_o(t)} \right| = 0 \tag{6}$$

The discriminant for the solutions of (6) for positive power is given by

$$\Delta = 1 - \frac{4p\,(t)\, X_{\text{DAB}}}{\pi v_i(t) v_o(t)} \tag{7}$$

By inspecting the quadratic equation, three categories of non-solutions can be identified, namely,

1. Non-existence of Δ at either v_i or v_o becoming zero
2. Imaginary solutions of ϕ for negative values of Δ
3. Out of bound values of ϕ

The first type of non-solutions cannot be addressed as it is mathematically impossible to solve the quadratic equation (6). Nevertheless, practically, the demanded power can be made zero by shutting down the converter at the zero crossing zones to make the power transfer zero. On the other hand, the second and third types of non-solutions can be controlled by changing the converter's parameters, which will be explained in the subsequent sections.

The power equation (6) is rewritten after substituting for $v_i(t)$ and $v_o(t)$, the equation simplifies to

$$\frac{\phi(t)^2}{\pi} - \mid \phi(t) \mid + \frac{|p(t)| X_{\text{DAB}}}{2V_{\text{RMS}}^2 \cos^2(\omega_0 t)} = 0 \tag{8}$$

As, $p(t) < 0 \Rightarrow \phi(t) < 0$ and $p(t) > 0 \Rightarrow \phi(t) > 0$, two equations are obtained

$$\frac{\phi(t)^2}{\pi} + \phi(t) - \frac{p(t)X_{\text{DAB}}}{2V_{\text{RMS}}^2 \cos^2(\omega_0 t)} = 0, \text{ for } p(t) < 0 \tag{9}$$

$$\frac{\phi(t)^2}{\pi} - \phi(t) + \frac{p(t)X_{\text{DAB}}}{2V_{\text{RMS}}^2 \cos^2(\omega_0 t)} = 0, \text{ for } p(t) > 0 \tag{10}$$

Now defining a function $\alpha(t)$

$$\alpha(t) = \frac{PX_{\text{DAB}}}{V_{\text{RMS}}^2} + \frac{QX_{\text{DAB}}}{V_{\text{RMS}}^2} \tan(\omega_0 t) \tag{11}$$

the quadratic equations finally reduce to

$$\phi(t)^2 + \pi\phi(t) - \pi\alpha(t) = 0, \text{ for } p(t) < 0 \tag{12}$$

$$\phi(t)^2 - \pi\phi(t) + \pi\alpha(t) = 0, \text{ for } p(t) > 0 \tag{13}$$

As the phase solutions $\phi(t)$ are constrained between $\pm\pi/2$, the final solutions are then written as

$$\phi(t) = -\frac{\pi}{2} + \frac{\sqrt{\pi^2 + 4\pi\alpha(t)}}{2}, \text{ for } p(t) < 0 \tag{14}$$

$$\phi(t) = \frac{\pi}{2} - \frac{\sqrt{\pi^2 - 4\pi\alpha(t)}}{2}, \quad \text{for } p(t) > 0 \tag{15}$$

The values of phase angle tend to $\pm\infty$ at $\omega_0 t = (2n + 1)\pi/2$ for $n \in \mathbb{Z}$. Therefore, the phase angle is to be saturated at these critical instances until the solutions become finite again. The designer must know where the phase angle is supposed to be saturated. Therefore, if the phase is limited at an arbitrary phase angle $\phi_{lt} \leq \pi/2$. The time instance (in radians) at which the phase limit is reached is to be known and must be individually found for the two values of the power expression (12), (13).

Considering the positive power quadratic (13) first and substituting the phase limit value of $+\phi_{lt}$ (as only positive phases can be found out for (13))

$$\phi_{lt}^2 - \pi\phi_{lt} + \pi\alpha(t) = 0 \tag{16}$$

$$-\phi_{lt}^2 + \pi\phi_{lt} = \pi\alpha(t) \tag{17}$$

$$\therefore \alpha(t) = \frac{\pi\phi_{lt} - \phi_{lt}^2}{\pi} \tag{18}$$

substituting $\alpha(t)$ from (11), one obtains, the time at the required angle to be

$$\omega_0 t_{+limit} = \tan^{-1}\left[-\frac{P}{Q} + \frac{V_{\text{RMS}}^2}{QX_{\text{DAB}}}\left\{\frac{-\phi_{lt}^2 + \pi\phi_{lt}}{\pi}\right\}\right] \tag{19}$$

a similar approach can be used for (12), to get the time instance at which a negative angle of $-\phi_{lt}$ is reached and is given by

$$\omega_0 t_{-limit} = n\pi + \tan^{-1}\left[-\frac{P}{Q} + \frac{V_{\text{RMS}}^2}{QX_{\text{DAB}}}\left\{\frac{\phi_{lt}^2 - \pi\phi_{lt}}{\pi}\right\}\right], n \in \mathbb{Z} \tag{20}$$

Also, from (13) and (12), the angle for reaching zero power is given by

$$\omega_0 t_{zero} = n\pi + \tan^{-1}\left(-\frac{P}{Q}\right), \text{ where } n \in \mathbb{Z} \tag{21}$$

Based on the observations from the nature of the power plots and the phase $\phi(t)$ behavior, the following conclusions can be drawn:

1. The points where the output current waveform reaches zero, the instantaneous power reaches zero, and the phase also reaches zero

2. When the voltage waveform reaches zero, the phase plot's solution ceases to exist due to the asymptotic behavior of the tangent function in (11)

3. When Q is positive, the phase plot needs to be saturated at $-\pi/2$ starting at the angle corresponding to $v(t) = 0^+$ and $+\pi/2$ for the angle corresponding to $v(t) = 0^-$

4. When Q is negative, the phase plot needs to be saturated at $\pi/2$ starting at the angle corresponding to $v(t) = 0^+$ and $-\pi/2$ for the angle corresponding to $v(t) = 0^-$

5. The exact time instance (in radians) at which the saturation is to be applied is governed by (19), (20)

6. The exact time instance (in radians) at which the power reaches zero is governed by (21)

7. For pure active power demands, the reactive power is zero, making (11) a constant value, which ultimately makes $\phi(t)$ also constant.

Based on the properties discussed in this section, two types of closed-form solutions for the phase are written for positive and negative reactive power demands. For $Q > 0$, the value of $\phi(2\omega_0 t)$ is given by,

$$\phi(2\omega_0 t) = \begin{cases} -\frac{\pi}{2} & \text{for } -\pi/2 \leq 2\omega_0 t \leq \omega_0 t_{-limit} \\ -\frac{\pi}{2} + \frac{\sqrt{\pi^2+4\pi\alpha(t)}}{2} & \text{for } \omega_0 t_{-limit} < 2\omega_0 t \leq \omega_0 t_{zero} \\ \frac{\pi}{2} - \frac{\sqrt{\pi^2-4\pi\alpha(t)}}{2} & \text{for } \omega_0 t_{zero} < 2\omega_0 t \leq \omega_0 t_{+limit} \\ \frac{\pi}{2} & \text{for } \omega_0 t_{+limit} < 2\omega_0 t \leq \pi/2 \end{cases} \tag{22}$$

For $Q < 0$

$$\phi(2\omega_0 t) = \begin{cases} \frac{\pi}{2} & \text{for } -\pi/2 \leq 2\omega_0 t \leq \omega_0 t_{+limit} \\ \frac{\pi}{2} - \frac{\sqrt{\pi^2-4\pi\alpha(t)}}{2} & \text{for } \omega_0 t_{+limit} < 2\omega_0 t \leq \omega_0 t_{zero} \\ -\frac{\pi}{2} + \frac{\sqrt{\pi^2+4\pi\alpha(t)}}{2} & \text{for } \omega_0 t_{zero} < 2\omega_0 t \leq \omega_0 t_{-limit} \\ -\frac{\pi}{2} & \text{for } \omega_0 t_{-limit} < 2\omega_0 t \leq \pi/2 \end{cases} \tag{23}$$

The physical interpretation of saturating the phase shift is that the DAB converter's power transfer characteristic (5) takes the maximum value at $\pm\pi/2$, the power transferred from the primary side to the secondary side cannot be increased using a phase beyond the $\pi/2$ limit. The DAB squeezes as much maximum instantaneous power as it can during the $\pi/2$ intervals.

2.3. PHASE SOLUTIONS FOR ACTIVE POWER FLOW

A special case of phase solution can be made for pure active power flows, in which case $Q = 0$. Therefore, the value of $\alpha(t)$ reduces to,

$$\alpha = \frac{PX_{\text{DAB}}}{V_{\text{RMS}}^2} \tag{24}$$

The phase angle is then written as,

$$\phi = -\frac{\pi}{2} + \frac{\sqrt{\pi^2 + \frac{4\pi\ PX_{\text{DAB}}}{V_{\text{RMS}}^2}}}{2}, \text{ for } P < 0 \tag{25}$$

$$\phi = \frac{\pi}{2} - \frac{\sqrt{\pi^2 - \frac{4\pi\ PX_{\text{DAB}}}{V_{\text{RMS}}^2}}}{2}, \quad \text{for } P > 0 \tag{26}$$

as α is a constant value, the value of phase angle $\phi(t)$ is also a constant. Therefore the phase shift angle on the DAB is to be a constant value for the entire line cycle when active power is demanded.

Also, (25), (26) show that as long as the second terms in both relations do not cross $-\pi/2$ or $\pi/2$ respectively or do not make the square root term negative, the phase value will be constant. Also, the non-existence of the solutions due to the voltage becoming zero, as described previously, does not become an issue as the desired instantaneous power also reaches zero at the same instant as the voltage reaches zero (a consequence of unity power factor operation).

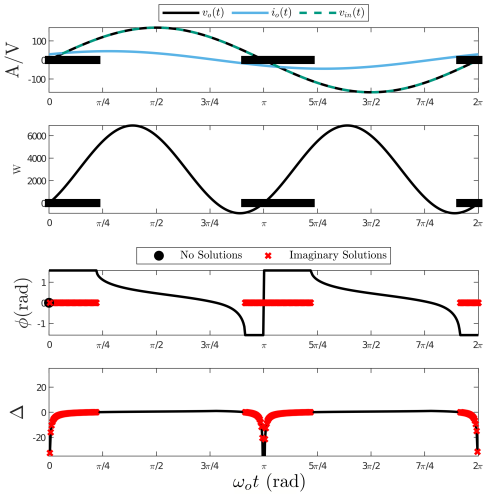

(a) Nature of roots for 10 µH for phase saturation applied for imaginary roots

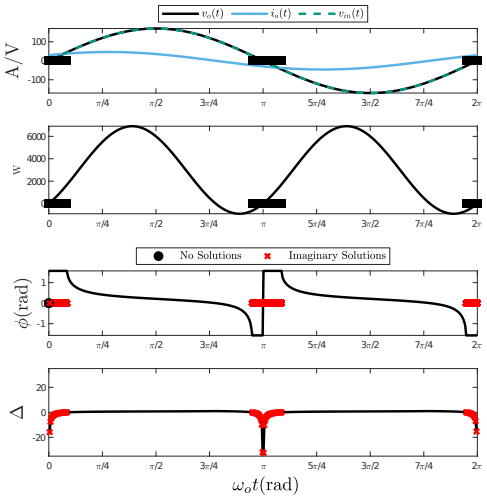

(b) Improved reproducibility of desired power by reducing L_{DAB} to 5 µH

Figure 5. Phase solutions based on leakage inductance choice

2.4. INDUCTANCE AND FREQUENCY CHOICE FOR SST DAB

The boundary for imaginary solutions in the quadratic equations is given by

$$1 - \frac{4p(t)X_{\text{DAB}}}{\pi v_i(t)v_o(t)} < 0 \tag{27}$$

which can be rearranged to inspect the relationship between $v_i(t)$, $v_o(t)$, $p(t)$, L_{DAB}, and f_{sw} as,

$$\frac{\pi v_i(t)v_o(t)}{8p(t)} < L_{\text{DAB}} \times f_{sw} \tag{28}$$

The boundary equation (28) shows that as long as the RHS term is greater than the LHS term, $\phi(t) \in \mathbb{C}$. Therefore, for a given value of LHS variables, a lower value of the RHS term will lead to an easier boundary to cross over for the LHS terms to guarantee $\phi(t) \in \mathbb{R}$.

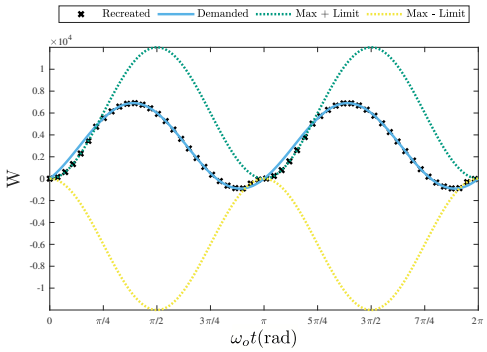

(a) Nature of roots for 10 µH for phase zeroing applied for imaginary roots

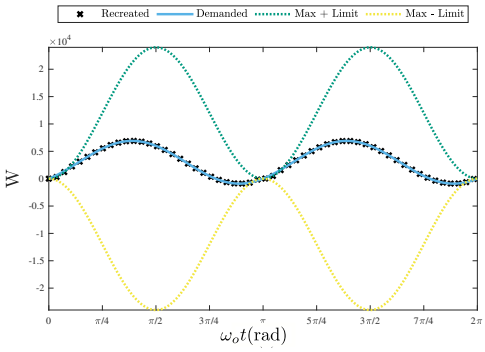

(b) Improved reproducibility of desired power by reducing L_{DAB} to 5 µH

Figure 6. Phase solution space visualization

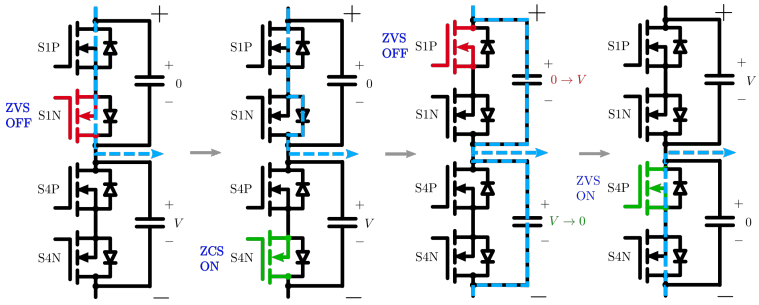

Figure 7. S1-S4 transition with a positive voltage applied to Leg and transformer current flowing outwards demonstrating FSS

Therefore, as the switching frequency increases, a lower inductance will be needed to maintain the same level of instantaneous power transferability. That being said, a lower switching frequency and a higher L_{DAB} are desirable to ease the SST DAB design for a given rated power specification from a practical standpoint.

Figures 5a and 5b show the $\phi(t)$ solution plots obtained for 10 µH and 5 µH of L_{DAB} respectively for the same apparent power demand and f_{sw}. The solutions are obtained by applying the phase solutions (22) or (23) depending on the sign of Q. The 10 µH case shows a higher range of imaginary solutions than that of the 5 µH case as described from the design equation (28). Figures 6a and 6b show an alternative viewpoint for apparent power flow from the DAB's perspective. The two enveloped waveforms (dotted waveforms) show the

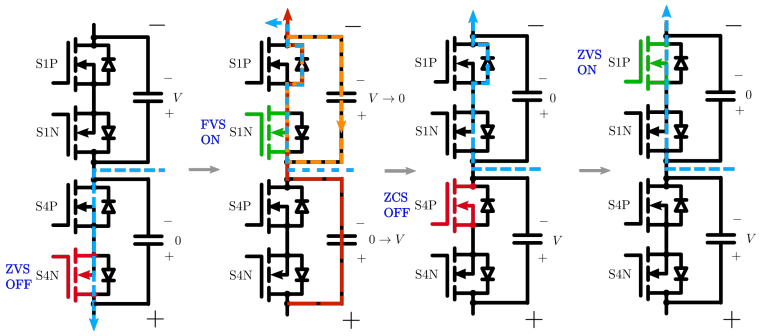

Figure 8. S4-S1 transition with a negative voltage applied to Leg and transformer current flowing inwards demonstrating PSS

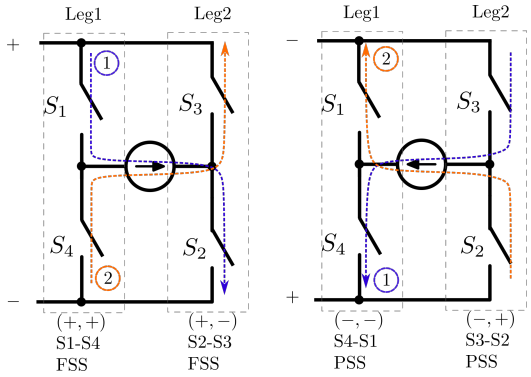

Figure 9. H-bridge switching: PSS case on the left and FSS case on the right

maximum possible power available for transfer between the two ac sources on either side of the ac-ac DAB at any given point in time. The demanded power (thick trace) describes the instantaneous power demand. The recreated power by the DAB is overlayed on top of the demanded power (shown as crosses). It can be inferred from the figures that the area enclosed between the Max + Limit and Max - Limit is the real solution space for the power quadratic equations (12) and (13) where $\phi(t) \in \mathbb{R}$. When the demanded power exceeds the maximum reproducible power limits, the DAB rides through the extreme value possible while overriding the demanded value. In these regions, the DAB squeezes as much power as it can from one side to the other. By reducing L_{DAB}, the peak power levels of the DAB increase, thereby shrinking the demand override regions leading to lower span of imaginary solutions.

3. SOFT-SWITCHING ANALYSIS

Each Half-Bridge (Leg) of the ac-ac DAB has four switches: SxP, SxN, SyP and SyN where $x \in \{1, 3, 5, 7\}$ and $y \in \{2, 4, 6, 8\}$. The switches belonging to odd number indices are referred to as High (Hi) side switches, and the ones belonging to the even indices are referred to as the Low (Lo) side switches. Each switch Sx or Sy again is given a sub-classification suffix—P or N based on the orientation of the MOSFET. In a DAB, the i_{DAB} can be either positive or negative based on the polarity of the grid voltage $V = v_i = v_o$. From a sign convention perspective, the current is positive if it flows out of the leg and vice-versa. The sign of this current is critical in determining whether the switching event is soft-switching or hard-switching. Based on the direction of the current and the voltage applied across a leg with bidirectional switches, two types of switching events are possible:

1. all four switches undergo soft-switching; i.e., Full Soft-Switching (FSS)
2. three out of four switches are soft-switched; Partial Soft-Switching (PSS)

3.1. FSS MECHANISM

An example of the FSS mechanism is shown in Figure 7. Assuming that the current is already flowing through S1P and S1N, four instances are shown for transitioning the current from S1P and S1N to S4P and S4N. The first step begins with S1N turning off under ZVS as the current continues to flow through its body diode. In the next step, S4N turns on under ZCS as no current flows through it. In the third step, S1P turns off under ZVS, and immediately, i_{DAB} starts charging the capacitor across S1 from $0 \rightarrow V$ and discharging the capacitor across S4 from $V \rightarrow 0$. Finally, the current transition from S1P and S1N to S4P and S4N is completed when S4P turns on under ZVS.

3.2. PSS MECHANISM

An example of the PSS mechanism is shown in Figure 8. Assuming that the current is already flowing through S4P and S4N, four instances are shown for transitioning the current from S4P and S4N to S1P and S1N. The first step begins with S4N turning off under ZVS as the current continues to flow through its body diode. In the second step, S1N turns on, and the following three events happen simultaneously:

1. the capacitor across S1 starts discharging the full blocking voltage, thus representing a Full Voltage Switching (FVS), i.e., hard-switching
2. i_{DAB} starts shifting from S4 to S1
3. the capacitor across S4 starts building the full blocking voltage.

In the third stage, the switch S4P turns off under ZCS as no current flows through it. Finally, S1P turns on under ZVS as the top capacitor is discharged to zero volts.

3.3. H-BRIDGE SOFT-SWITCHING CONDITIONS

So far, soft-switching is explained from the perspective of a half-bridge. The soft-switching mechanism of an H-bridge depends on the relative signs of i_{DAB} and V. Assuming the same voltage polarity for both primary and secondary bridges, the sign of the current is opposite in the two half bridges—Leg1 and Leg2. When the current leaves Leg1, as shown in Figure 9 for the FSS case, it gets a positive sign. If a positive voltage is applied across the switches and the current leaves Leg1, it gets a $(+,+)$ notation, thus suggesting that both the voltage and current are positive. For the same voltage polarity, Leg2 gets a $(+,-)$ notation indicating a negative current. Alternatively, if a negative voltage is applied across the Legs and the current flows from Leg2 to Leg1, $(-,-)$ notation for Leg1 is indicated in Figure 9, thus suggesting PSS.

A similar sign convention is followed for the secondary bridge. Here, the dot convention of the transformer must be accounted for to understand the FSS or PSS mechanism of the secondary bridge. The current entering the dot from one side of the transformer leaves the dot from the other side. The primary and secondary side switching events are offset by the phase angle value used to control the converter.

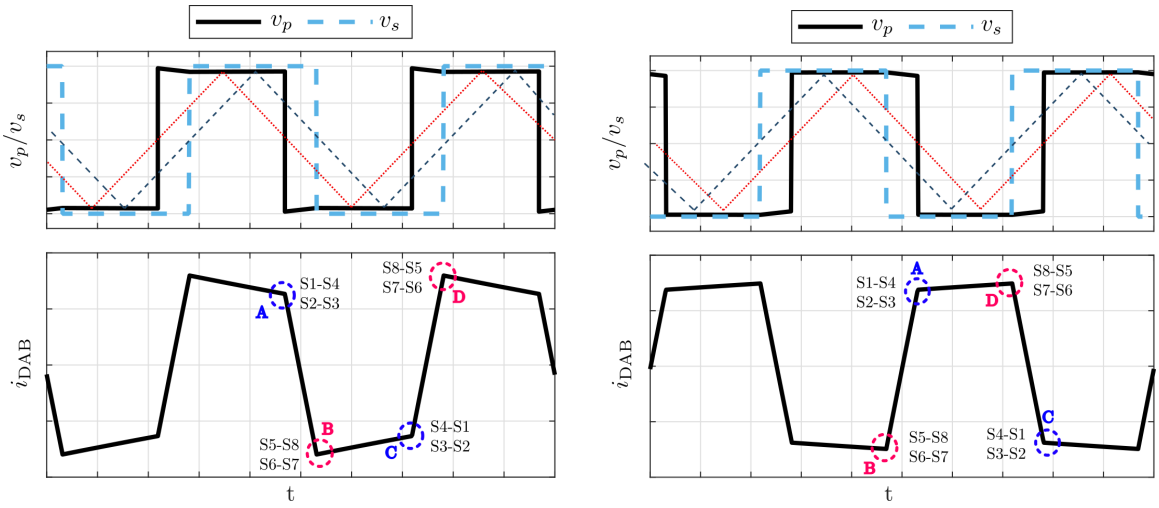

(a) DAB phase state progression for positive phase angle: ABCD sequence

(b) DAB phase state progression for negative phase angle: BADC sequence

Figure 10. Switching order sequences based on the sign of phase

3.4. SWITCHING SEQUENCES

Figure 10a and 10b show primary and secondary voltages and the resulting inductor current in a DAB. Here, four points of interest—A, B, C, and D—are identified. If the sign of the i_{DAB} at A is known, the sign of the rest of the points can be ascertained. Using the sign of A and that of the grid voltage, the mechanism for one switching cycle can be scheduled. Hence, an algorithm can be formulated for implementing the switching mechanism of the ac-ac DAB in an embedded platform. The algorithm can be divided into three cases based on the sign of the phase angle. Figure 10a and 10b show the up-down counters used in an embedded processor for generating switching signals. Here two switching sequences can be

Table 1. Switching transitions

Point	Transition
A	S1→S4 and S2→S3
B	S5→S8 and S6→S7
C	S4→S1 and S3→S2
D	S8→S5 and S7→S6

Table 2. Current Sensor Sign to Switching Transition Lookup

	Current sign	Leg1	Leg2	Leg3	Leg4	Leg1	Leg2	Leg3	Leg4
$\phi > 0$	for Leg1 at C	S4-S1	S3-S2	S8-S5	S7-S6	S1-S4	S2-S3	S5-S8	S6-S7
ABCD Sequence	-	-	+	+	-	+	-	-	+
	+	+	-	-	+	-	+	+	-
	Current sign	Leg1	Leg2	Leg3	Leg4	Leg1	Leg2	Leg3	Leg4
$\phi < 0$	for Leg1 at D	S4-S1	S3-S2	S5-S8	S6-S7	S1-S4	S2-S3	S8-S5	S7-S6
BADC Sequence	-	-	+	+	-	+	-	-	+
	+	+	-	-	+	-	+	+	-

observed—ABCD and BADC. When the phase shift in the DAB is positive, the inductor current takes the shape of the typical trapezoidal waveform as shown in Figure 10a. The switching events occur in the following sequence A→B→C→D. For negative phase shift, the switching sequence is B→A→D→C, as shown in Figure 10b.

3.5. SWITCHING SEQUENCE LOOKUP TABLES

Based on the FSS and PSS examples, every half bridge undergoes either an FSS or a PSS based on the V and i_{DAB} at the instance of switching. Tables 2 and 3 show all the possible voltage and current combinations for all the legs of the DAB. Table 2 describes what the current signs of switching instances will be based on the sign of ϕ and the i_{DAB} sensed at the point of interest. A sign convention is adopted in the first two columns of Table 3. A positive sign in the voltage column denotes a positive voltage applied across each Leg and vice-versa. A positive sign is applied to $i_x, x \in \{1, 2, 3, 4\}$ shown in Figure 4 to denote the current leaving Leg$x$ and a negative sign to denote the current entering Leg$x$. When

undergoing FSS, the first, third, and fourth switching instances are all ZVS, while the second is ZCS. In PSS, the first and fourth switching instances are ZVS, the third is ZCS, and the second is FVS, i.e., hard-switched.

Table 3. Hard and soft-switching conditions for a Leg

v_{in}	i_1	Transition	OFF	ON	OFF	ON	Soft-Switching
+	+	Hi-Lo	HiN	LoN	HiP	LoP	Full
+	-	Hi-Lo	HiP	LoP	HiN	LoN	Partial
-	-	Hi-Lo	HiP	LoP	HiN	LoN	Full
-	+	Hi-Lo	HiN	LoN	HiP	LoP	Partial
+	-	Lo-Hi	LoN	HiN	LoP	HiP	Full
+	+	Lo-Hi	LoP	HiP	LoN	HiN	Partial
-	+	Lo-Hi	LoP	HiP	LoN	HiN	Full
-	-	Lo-Hi	LoN	HiN	LoP	HiP	Partial

3.6. SWITCHING ALGORITHM

In embedded systems, Interrupt Service Routines (ISR) are used for coordinating real-time data acquisition and decision-making processes to enable the generation of switching signals and seamless implementation of algorithms. A flow chart is provided in Figure 11 to implement the switching algorithm. The algorithm is divided into three major substeps, namely,

1. Data acquisition

2. Sequence identification and data lookup

3. Compare enforcement

In the first step, the polarity of V, i_{DAB}, and ϕ are acquired. Two sensors are used for this purpose: a voltage sensor sensing either v_{in} or v_{out} and a current sensor sensing i_1 current as shown in Figure 4. Based on these signs, decisions are made on whether the switching sequence is an ABCD or BADC. Once the sequence is detected, the switching

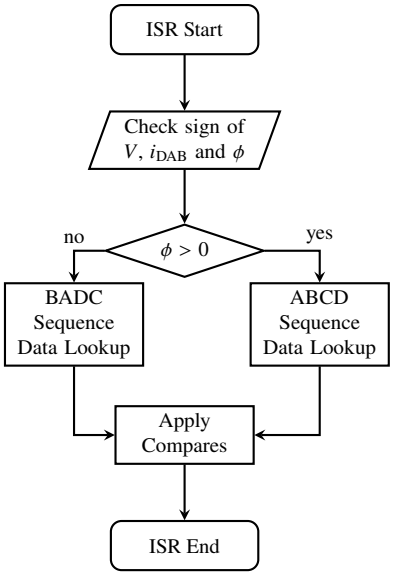

Figure 11. Soft-switching algorithm implemented in `ISR-1`

sequence for S1-S8 is decided based on the polarity of V and i_1. Here, the sequences in Table 2 help in cross-referencing the rows to be selected in Table 3. After the sequence is detected, compare values used to generate the switching signals are enforced.

Figure 12 shows the up-down counter and its coordination with various tasks for an ABCD sequence. The instances are subscripted to denote the cycle of operation. Three tasks T_1, T_2, and T_3 are shown in the figure to aid the understanding of the algorithm. Task T_1 is responsible for computing the phase deployment required to meet the demanded power value using the relations derived in Section 2. Tasks T_2, and T_3, on the other hand, coordinate the soft-switching algorithm. T_2 is always triggered by the leading bridge and initiates V and i_{DAB} ADC acquisitions to run the three steps described earlier. Even though T_2 is shown to set the compares for S1 and S4 switches, it also sets the compare values for all other switches. Only four compare assignments are shown in Figure 12 to avoid redundancy. Once T_2 sets the compare sequences for the switches, the compares remain the same throughout the rising slope period. The last task T_3 reverses the compares to preserve the switching order. The flow chart in Figure 11 is implemented in T_2 ; T_3 only inverts the compares that T_2 decides.

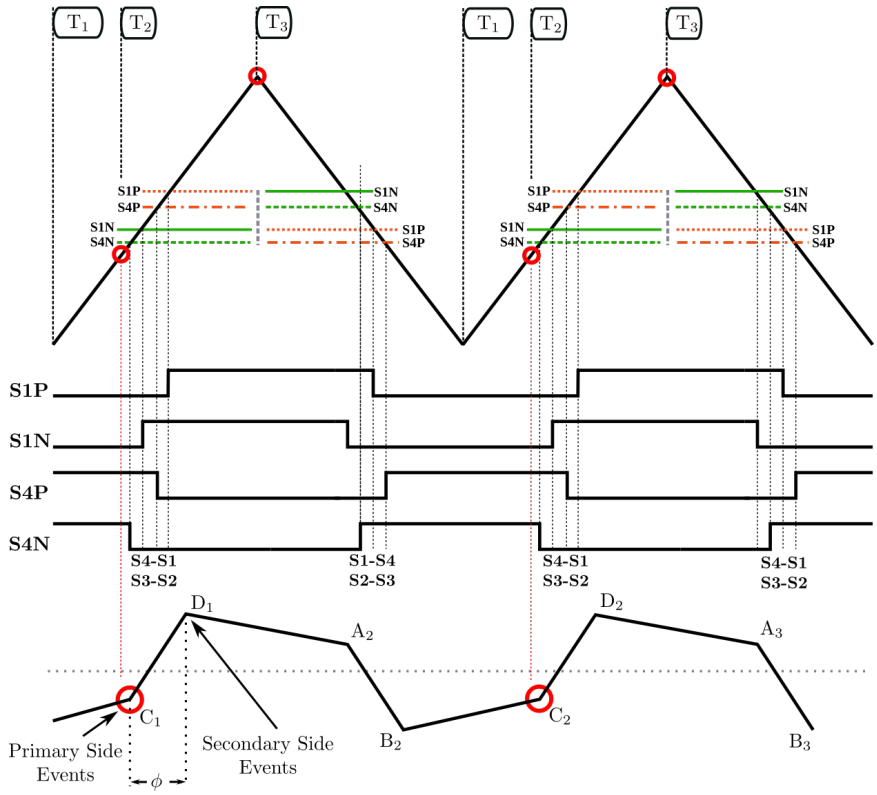

Figure 12. DSP implementation of soft-switching algorithm for ABCD sequence

The compare values are shadowed to be effective in the next cycle, which always starts at T_3. The primary side's up-down counter always triggers the T_2 at the point shown in Figure 12. The trigger point is configured to accurately capture the sign of i_{DAB}.

4. TRANSFORMER MODELING AND DESIGN

In this section, the design requirements for an ac-ac DAB transformer will be discussed. The transformer is designed for 120 V of input and output RMS grid voltage and 1 kVA of apparent power. But before starting with the actual design parameters, the flux characteristic in the transformer must be understood as there are two frequencies at play, namely the switching frequency and the grid frequency components.

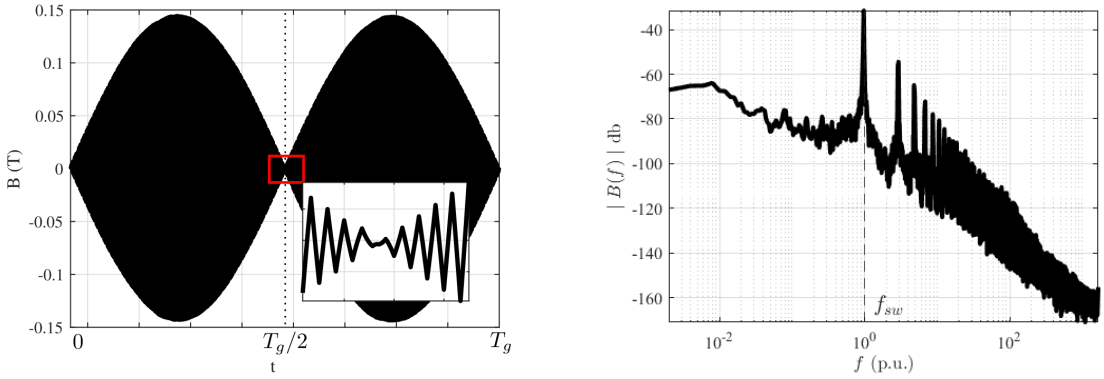

(a) Time vs. transformer flux plot for ac-ac DAB (b) ACAC DAB transformer flux spectrum

Figure 13. Transformer flux waveforms

Figure 13a shows the time vs. magnetic flux plot for a transformer for one cycle of grid waveform. The plot shows a switching waveform enveloped inside a grid waveform. Therefore the transformer is subjected to both the grid and the switching frequencies. The Fourier decomposition on the flux waveform is shown in Figure 13b. The transformer is predominantly subjected to the switching frequency. Therefore, the transformer must be designed for the switching frequency.

4.1. TRANSFORMER DESIGN

The area product for transformer design is given by

$$\text{AP} = \left(\frac{S_{tot}(10^4)}{K_u K_f K_j B_{max} f_{sw}} \right)^{(8/7)} \tag{29}$$

where K_u, K_f, and K_j are the fill factor, form factor, and temperature rise factors, respectively. The switching frequency f_{sw} is 30 kHz. The calculated AP value is 26 cm^4 for K_u of 30% and $K_f = 4$. Accounting for a 50 °C, a K_j value of 534 is selected. A B_{max} value of 120mT is chosen. Based on the calculated AP value, an EE 80/38/20 core is selected. Based on the design, a transformer with 32 turns, each on the primary and secondary sides is required.

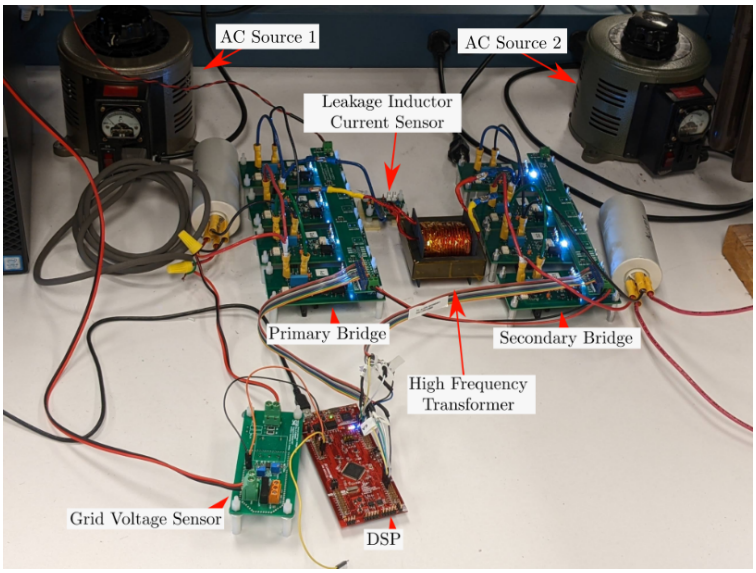

Figure 14. ac-ac DAB hardware setup

At a switching frequency of 30 kHz, the skin depth for copper conductors is 376 µm. To eliminate the skin and proximity effects, the radius of the selected wire should be smaller than the skin depth. Hence, AWG 25 magnet wire that has a radius of 227.5 µm is selected. To meet the desired current level, 19 strands of this wire are used to make a litz wire bundle. The constructed transformer is shown in Figure 14.

4.2. CORE LOSSES

The expression for core losses in a transformer is given by

$$P_{\text{core}} = k f_{sw}^{x} \Delta B^{y} \tag{30}$$

where k, x, y are material constants, and ΔB is half of the flux excursion in the BH excitation loop. The core losses in ac-ac flux waveform shown in Figure 13a are compared with a triangle wave signal of same peak magnitude as seen in a classic dc-dc phase shifted DAB converter. To compare both signals, Root Mean Index (RMy) for $y \in \mathbb{R}^{+}$ is used. The RMy

for an arbitrary periodic waveform $r(t)$ is given by

$$R_{\mathrm{RM}y} = \sqrt[y]{\frac{1}{T}\int_0^T |\, r(t)\,|^y \, dt} \tag{31}$$

The $\Delta B^y_{\mathrm{RM}y}$ for a P-type material from [22] core with $y = 2.62$ is calculated for the ac-ac flux waveform and a dc-dc flux waveform, and the former was about 2.22 times lower than the latter. Therefore the core losses in the ac-ac DAB converter will be much lower than an ac-dc-dc-ac counterpart.

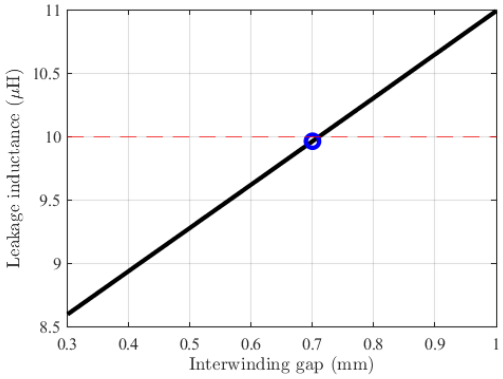

(a) L_{lk} at different interwinding gaps.

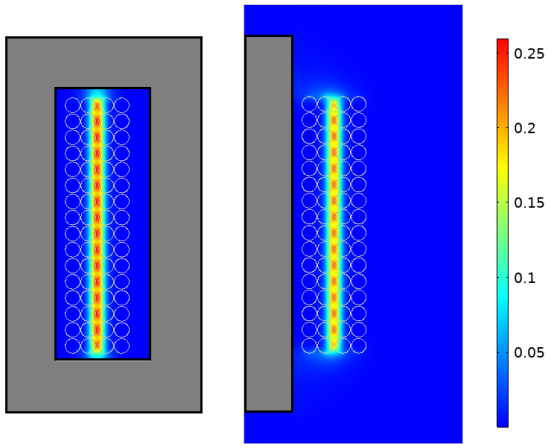

(b) Magnetic energy density ($\mathrm{J/m^3}$) plots for the inside window (left) and outside window (right) planes of the transformer.

Figure 15. Integrated leakage inductance design using FEM based Double 2D Model in COMSOL multiphysics software

4.3. INTEGRATED LEAKAGE INDUCTANCE DESIGN

A 10 µH of L_{DAB} is desired in this work. This inductance is integrated as the leakage inductance (L_{lk}) of the transformer. The transformer designed earlier has 32 turns on both the primary and secondary sides. The turns on either side are split into two layers of 16 turns each, which occupy the entire winding height.

In order to achieve the desired L_{lk} value, the transformer windings are designed in COMSOL Multiphysics using the Double-2-D model [23]. Two degrees of freedom can be availed for controlling the L_{lk}: the interlayer gap and the interwinding gap. The interwinding gap offers the scope for larger adjustments in L_{lk} than the interlayer gap [23]. As such, the interlayer gap is fixed at 0.2 mm while the interwinding gap is swept between 0.3 mm-1 mm. Figure 15a plots the leakage inductance L_{lk} for different interwinding gaps, which shows that a gap of 0.7 mm is required to meet the 10 µH of L_{lk}. Figure 15b shows the surface plots of the magnetic energy density across the inside window and outside window planes of the transformer for the selected gap of 0.7 mm.

5. HARDWARE IMPLEMENTATION

The hardware setup of the ac-ac DAB converter is shown in Figure 14. The primary and secondary bridges are comprised of 650 V 46 A N-channel MOSFETs driven by isolated optocoupler gate drivers. Two variable ac autotransformers (variacs) are used to energize the two sides of the ac-ac DAB converter. Both ac voltages are set to be in the same voltage and phase $V_{\alpha/\underline{\gamma}}$. A TMS320F28377S Digital Signal Processor (DSP) controls the switches and the phase between the bridges. The DSP is also responsible for computing the phase angles required in different instances and enforcing the soft-switching behaviors. A hall-effect voltage sensor based on an LV 25-P sensor is connected to one ac voltage to extract the phase, frequency, and RMS information for use in the various algorithms running on the DSP. A hall-effect current sensor based on an LTS 25-NP is connected to Leg1 as shown in Figure 4 to capture the sign of the current for soft-switching decisions. Two 1.5 µF film capacitors C_1 and C_2 are connected on either side of the ac-ac DAB to act as filters.

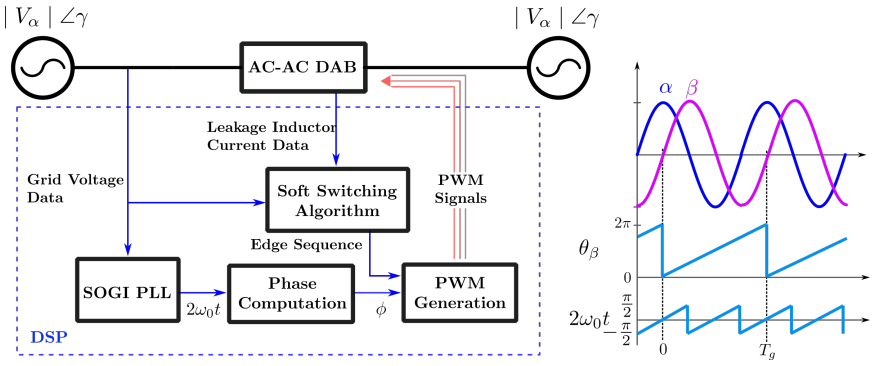

Figure 16. Hardware diagram for open loop control of ac-ac DAB.

Table 4. Simulation Parameters

Parameter	**Value**
Input Voltage	30 V
Output Voltage	30 V
Leakage Inductance	10 µH
Switching Frequency	30 kHz

5.1. POWER WAVEFORMS

A block diagram for power control is shown in Figure 16. The diagram shows the two ac sources on either side of the ac-ac DAB and various algorithms running inside the DSP. A Second Order Generalized Integrator (SOGI) Phase Locked Loop (PLL) [24] is used to extract the phase, frequency, and RMS information from the input grid. The grid voltage and leakage inductor current data are handed over to the soft-switching algorithm to enable the edge sequence decisions. The RMS value and phase information computed by the SOGI algorithm are handed off to the phase computation block. The $2\omega_0 t$ data is extracted from the SOGI PLL data by wrapping the phase value between $-\pi/2$ and $\pi/2$ as shown in Figure 16. Additionally, the PLL is synchronized to the quadrature component of the input grid waveform to fix the $2\omega_0 t$ value.

The power flow performance for positive and negative active power flow demands are shown in Figures 17a and 17b, respectively. The active power flow expressions (25) and (26) are used to compute the phase angle required to transfer the required power flow.

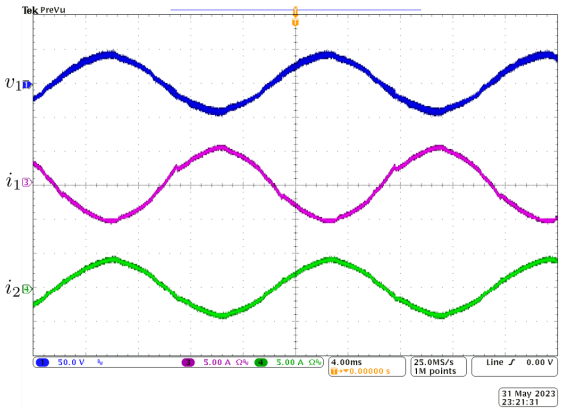

(a) Active power flow from ac voltage-1 to ac voltage-2.

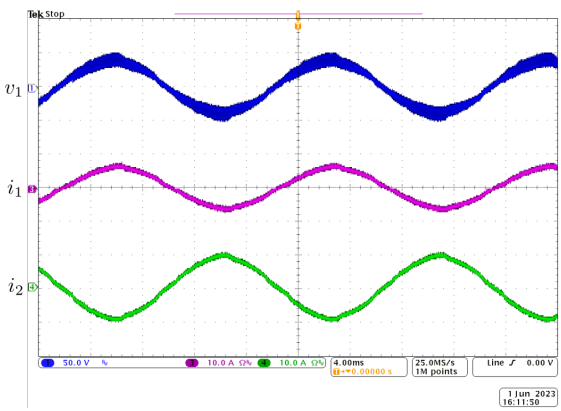

(b) Active power flow from ac voltage-2 to ac voltage-1.

Figure 17. Active power flow mechanism in ac-ac DAB converter

For a reactive power flow scenario, the $2\omega_0 t$ signal computed by the SOGI PLL is used to compute the phase angle (22)-(23). Figures 18a, 18b demonstrate ac voltage-1 consuming reactive power and producing reactive power respectively while consuming active power from ac voltage-2.

5.2. SOFT-SWITCHING PERFORMANCE

In order to demonstrate the efficacy of the soft-switching behaviors of the proposed soft-switching algorithm in Section 3, the ZVS characteristics of the last MOSFET are demonstrated. For ABCD and BADC sequences pertaining to $\phi > 0$ and $\phi < 0$ cases, respectively, the last MOSFET undergoes ZVS turn ON. In order to control the rise and settling times of the snubber circuit, a 90 nF capacitor C_s and 25 Ω resistor R_s are used across each bidirectional switch.

Figure 19a shows the ZVS turn-on characteristic of S4N MOSFET for an S1-S4 transition for positive phase shift (ABCD sequence). The voltage of the grid is negative, and i_{DAB} is negative at the instant of switching. Table 2 shows that for positive current sensed at point C leads to a negative current at the S1-S4 transition. Looking up the switching

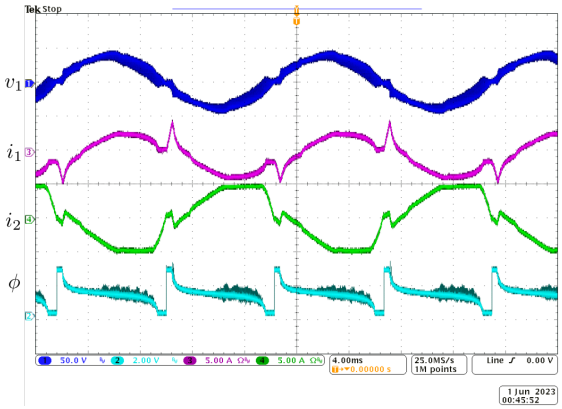

(a) ac voltage-1 consuming active power and reactive power from ac voltage-2.

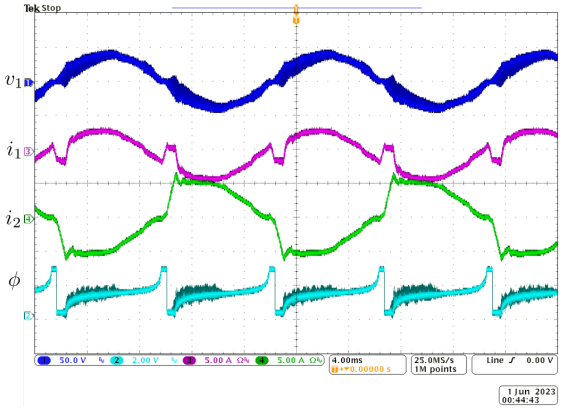

(b) ac voltage-1 consuming active power from ac voltage-2 and delivering reactive power to ac voltage-2.

Figure 18. Combined reactive and active power flow waveforms in ac-ac DAB converter

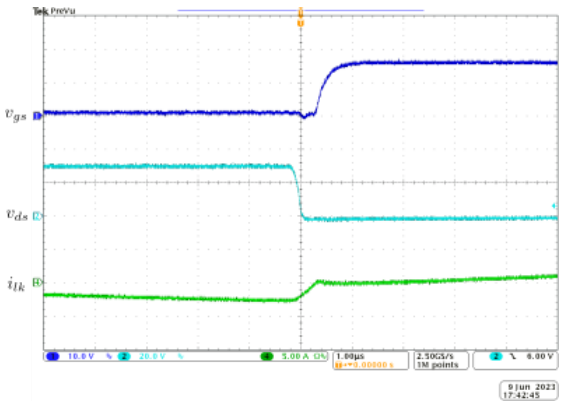

(a) ZVS turn ON characteristic of S4N MOSFET for S1-S4 transition for $\phi > 0$ when $V < 0$, $I_{\text{DAB}} < 0$ at the switching instance

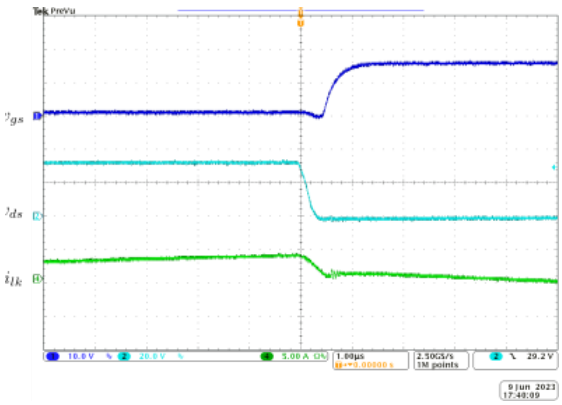

(b) ZVS turn ON characteristic of S4P MOSFET for S1-S4 transition for $\phi > 0$ when $V > 0$, $I_{\text{DAB}} > 0$ at the switching instance

Figure 19. Soft switching demonstration for various conditions in ac-ac DAB converter

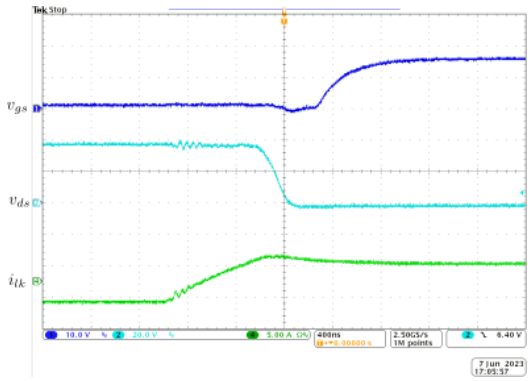

Figure 20. ZVS turn ON characteristic of S4P MOSFET for S1-S4 transition for $\phi < 0$ when $V > 0$, $I_{\text{DAB}} > 0$ at the switching instance

sequence from Table 3 shows that the transition is an FSS sequence. The MOSFET's drain-source voltage v_{ds} reaches zero well before the gate-source voltage v_{gs} command of the MOSFET goes high.

A similar situation is observed for the S4P MOSFET as shown in Figure 19b where the grid voltage is positive. The current is negative at the decision instance at C for the ABCD sequence, leading to a positive current at the instant of switching, leading again to an FSS sequence. Lastly, a BADC sequence is demonstrated where the S4P MOSFET's ZVS turn-on characteristic is shown in Figure 20 for positive voltage and positive current at decision instance at D, leading to a positive current at the switching instance. Again, the DSP is found to correctly make the switching decision to switch the MOSFETs in the correct sequence, demonstrating the correctness of the soft-switching algorithm

6. CONCLUSIONS

This work provides a comprehensive analysis for calculating the phase angles of an ac-ac DAB when it is operated for both active and reactive power flows. The choice of DAB inductance and the switching frequency is a critical design parameter in sizing the power transferability of the DAB. A mathematical design relationship is formulated to maximize the instantaneous power transfer capability of the DAB for the requested design

specifications. When compared to an ac-dc-dc-ac SST topology, this particular topology shows the pure advantage of soft-switching in almost all the switches, thereby leading to very high efficiency. It is found that the critical parameters to identify the switching mechanism are the signs of the leakage inductor current, applied grid voltage, and the phase shift at the instant of switching. Look-up tables derived herein are used by the processor to decide the switching order in each Leg of the DAB to achieve full or partial soft-switching. Finally, a flow chart is provided to systematically look up the data in the given switching tables and realize the switching algorithm in embedded hardware. To account for time criticality, ISR-based implementation is built around the algorithm to ensure adherence to real-time constraints in acquiring the data and enforcing the switching compare actions. A high-frequency transformer with integrated leakage inductance is designed to account for the DAB inductance. It is also shown that the core losses in the ac-ac transformer are much lower than in the ac-dc-dc-ac case. Finally, a hardware prototype is constructed for the ac-ac DAB topology, and the phase calculation and soft-switching algorithms are implemented to demonstrate the power flow capability and the validity of the proposed soft-switching algorithm.

REFERENCES

[1] X. She, A. Q. Huang, and R. Burgos, "Review of solid-state transformer technologies and their application in power distribution systems," *IEEE Journal of Emerging and Selected Topics in Power Electronics*, vol. 1, no. 3, pp. 186–198, 2013.

[2] F. Bignucolo, M. Bertoluzzo, and C. Fontana, "Applications of the solid state transformer concept in the electrical power system," in *2015 AEIT International Annual Conference (AEIT)*, 2015, pp. 1–6.

[3] Q. Zhu, L. Wang, D. Chen, L. Zhang, and A. Q. Huang, "Design and implementation of a 7.2kv single stage ac-ac solid state transformer based on current source series resonant converter and 15 kv sic mosfet," in *2017 IEEE Energy Conversion Congress and Exposition (ECCE)*, 2017, pp. 1288–1295.

[4] F. Ruiz, M. A. Perez, J. R. Espinosa, T. Gajowik, S. Stynski, and M. Malinowski, "Surveying solid-state transformer structures and controls: Providing highly efficient and controllable power flow in distribution grids," *IEEE Industrial Electronics Magazine*, vol. 14, no. 1, pp. 56–70, 2020.

[5] H. Chen and D. Divan, "Soft-switching solid-state transformer (s4t)," *IEEE Transactions on Power Electronics*, vol. 33, no. 4, pp. 2933–2947, 2018.

[6] R. Rahmoun and M. Patt, "High efficiency single-phase dual-active-bridge ac/ac converter," in *2019 21st European Conference on Power Electronics and Applications (EPE '19 ECCE Europe)*, 2019, pp. P.1–P.10.

[7] K. Mohapatra and N. Mohan, "Matrix converter fed open-ended power electronic transformer for power system application," in *2008 IEEE Power and Energy Society General Meeting - Conversion and Delivery of Electrical Energy in the 21st Century*, 2008, pp. 1–6.

[8] H. Keyhani, H. A. Toliyat, M. Harfman-Todorovic, R. Lai, and R. Datta, "An isolated resonant ac-link three-phase ac–ac converter using a single hf transformer," *IEEE Transactions on Industrial Electronics*, vol. 61, no. 10, pp. 5174–5183, 2014.

[9] K. Basu, A. Shahani, A. K. Sahoo, and N. Mohan, "A single-stage solid-state transformer for pwm ac drive with source-based commutation of leakage energy," *IEEE Transactions on Power Electronics*, vol. 30, no. 3, pp. 1734–1746, 2015.

[10] A. Sharma, K. J. P. Veeramraju, and J. W. Kimball, "Power flow control of a single-stage ac-ac solid-state transformer for ac distribution system," in *2022 IEEE Power and Energy Conference at Illinois (PECI)* [Accepted], 2022.

[11] A. Prasai, H. Chen, R. Moghe, Z. Wolanski, K. Chintakrinda, A. Zhou, J. C. Llambes, and D. Divan, "Dyna-c: Experimental results for a 50 kva 3-phase to 3-phase solid state transformer," in *2014 IEEE Applied Power Electronics Conference and Exposition - APEC 2014*, 2014, pp. 2271–2277.

[12] J. Ai-juan, L. Hang-tian, and L. Shao-long, "A new matrix type three-phase four-wire power electronic transformer," in *2006 37th IEEE Power Electronics Specialists Conference*, 2006, pp. 1–6.

[13] M. Sabahi, A. Y. Goharrizi, S. H. Hosseini, M. B. B. Sharifian, and G. B. Gharehpetian, "Flexible power electronic transformer," *IEEE Transactions on Power Electronics*, vol. 25, no. 8, pp. 2159–2169, 2010.

[14] E. Ronan, S. Sudhoff, S. Glover, and D. Galloway, "A power electronic-based distribution transformer," *IEEE Transactions on Power Delivery*, vol. 17, no. 2, pp. 537–543, 2002.

[15] S. Bhattacharya, T. Zhao, G. Wang, S. Dutta, S. Baek, Y. Du, B. Parkhideh, X. Zhou, and A. Q. Huang, "Design and development of generation-i silicon based solid state transformer," in *2010 Twenty-Fifth Annual IEEE Applied Power Electronics Conference and Exposition (APEC)*, 2010, pp. 1666–1673.

[16] D. Gonzalez-Agudelo, A. Escobar-Mejía, and H. Ramirez-Murrillo, "Dynamic model of a dual active bridge suitable for solid state transformers," in *2016 13th International Conference on Power Electronics (CIEP)*, 2016, pp. 350–355.

[17] H. Qin and J. W. Kimball, "Solid-state transformer architecture using ac–ac dual-active-bridge converter," *IEEE Transactions on Industrial Electronics*, vol. 60, no. 9, pp. 3720–3730, 2013.

[18] ——, "Ac-ac dual active bridge converter for solid state transformer," in *2009 IEEE Energy Conversion Congress and Exposition*, 2009, pp. 3039–3044.

[19] G. G. Facchinello, L. L. Brighenti, S. L. Brockveld, D. C. Martins, and W. M. Dos Santos, "Closed-loop operation and control strategy for the dual active half bridge ac-ac converter," in *2017 IEEE 8th International Symposium on Power Electronics for Distributed Generation Systems (PEDG)*, 2017, pp. 1–7.

[20] K. J. Veeramraju, A. Sharma, and J. W. Kimball, "A comprehensive analysis on complex power flow mechanism in an ac-ac dual active bridge," in *2022 IEEE Power and Energy Conference at Illinois (PECI)*, 2022, pp. 1–6.

[21] G. Venkataramanan and N. Kogalur, "A hybrid 4-quadrant switch for ac power conversion," in *2019 IEEE Energy Conversion Congress and Exposition (ECCE)*, 2019, pp. 5487–5493.

[22] Magnetics inc. p-type material. [Online]. Available: https://www.mag-inc.com/Products/Ferrite-Cores/P-Materialhttp://link.com

[23] A. Sharma and J. W. Kimball, "Transformer leakage inductance design methodology," in *2023 IEEE Applied Power Electronics Conference and Exposition (APEC)*, 2023, pp. 1572–1578.

[24] J. Xu, H. Qian, Y. Hu, S. Bian, and S. Xie, "Overview of sogi-based single-phase phase-locked loops for grid synchronization under complex grid conditions," *IEEE Access*, vol. 9, pp. 39 275–39 291, 2021.

II. AN EXTENDED GENERALIZED AVERAGE MODELING FRAMEWORK FOR POWER CONVERTERS

Kartikeya Jayadurga Prasad Veeramraju, Jacob A. Mueller and Jonathan W. Kimball
Department of Electrical and Computer Engineering
Missouri University of Science and Technology
Rolla, MO 65401 USA
Email: asc4v@mst.edu, kimballjw@mst.edu

ABSTRACT

The Generalized Averaged Modeling (GAM) technique is traditionally employed to capture the dynamic performance of power electronic converters. This paper proposes an improved version of it, named the Extended-GAM (EGAM) technique, which supports the multiplication of two Double Fourier Series (DFS) signals in the time domain. Multiplication of DFS signals in the time domain translates to the 2D-convolution of coefficients of the DFS terms of their equivalent Discrete Fourier Image (DFI) representations. Thus, the proposed EGAM technique, capable of capturing many harmonics present in the output of a power converter, effectively captures the dynamic behavior of power converters excited by two distinct frequencies. The proposed technique is then converted into an algorithm suitable for numerical platforms, which typically use Ordinary Differential Equation (ODE) solvers. The proposed algorithm is validated based on the observations of the effects of harmonic truncation. The efficacy of the proposed technique is assessed through a case study, wherein a single-phase inverter employs LC filters on both the dc-link and the ac-side. Finally, it is shown that the results obtained with the proposed method show an excellent congruence between simulation and hardware experimental models. Additionally, the proposed algorithm is packaged into a MATLAB toolbox and shared for future implementations.

1. INTRODUCTION

The Generalized Averaged Modeling (GAM) technique is instrumental in systems where Small Ripple Approximation (SRA) may not be applied, such as series-resonant converters, three-phase inverters, Dual Active Bridge (DAB) converters. Modeling poses difficulties, as the SRA about an operating point cannot be applied to such systems. The idea of GAM is first presented in [1], where selective frequencies for modeling various power electronic converters and operators over a state variable expressed as Fourier coefficients were presented. GAM is applied to a dc-dc converter, and its frequency-dependent structure is described [1, 2, 3]. The product of two Fourier coefficients for the dc and fundamental terms is shown [1, 2]. These product terms are directly used in subsequent works using GAM treatment on DABs [4, 5, 6, 7], series resonant converters [8], Modular Multilevel Converter (MMC) [9, 10], and microgrids [11]. Of late, GAM is also being referred to as the *Dynamic Phasor Modeling* (DPM) technique as described in the works on inverter modeling studies [12, 13, 14], and diode bridge rectifiers [15]. GAM was also shown to model and describe the stability behavior of inverter-based microgrids by eigenvalue analysis [16] for imbalance conditions and advanced droop control techniques [17]. It is shown in [18] that, unlike other models, the GAM technique can capture multi-frequency dynamics in conventional dc-dc converters. A *dimension* in the context of this work refers to an excitation frequency. Therefore, a GAM technique using a single frequency is called uni-dimensional GAM.

The necessity for including two excitation frequencies must be concretely set to realize the motivation for this work. Figure 1 shows models of increasing complexity, introduced alongside exemplary topologies, connecting each increase in model complexity to a different specific modeling requirement. A buck converter is shown in Figure 1(a). This converter is assumed to have the ripple value Δx in its state variables that is much smaller than the dc component x_{dc} (i.e., $\Delta x \ll x_{\mathrm{dc}}$). Therefore, State Space Averaging (SSA) technique has traditionally been applied to capture the dynamics of the inductor current and

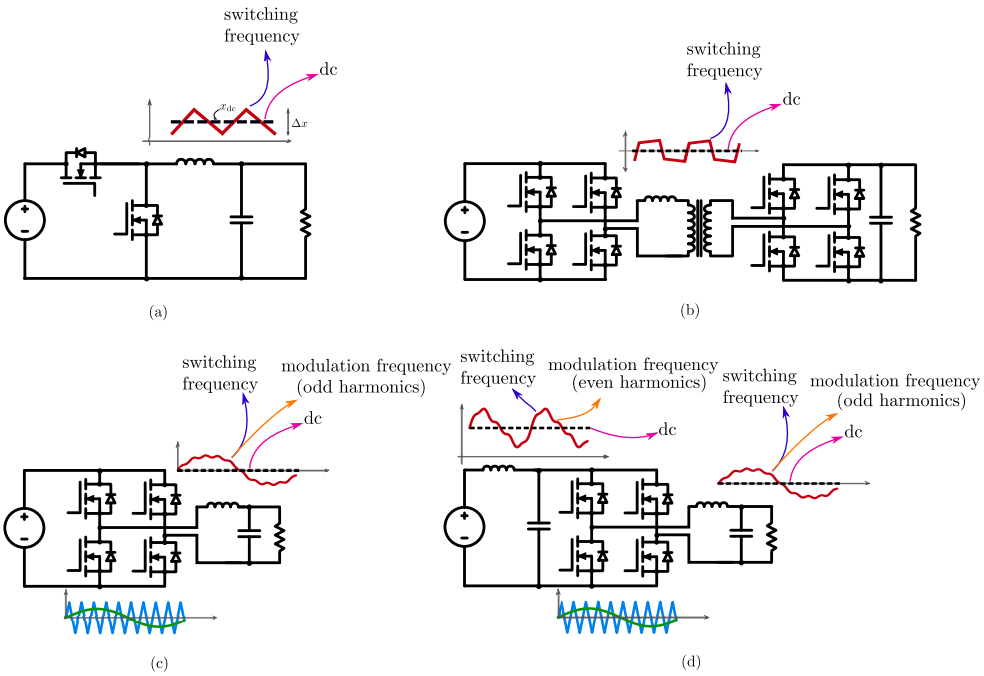

Figure 1. Various power converters: (a) a buck converter with single switching frequency; SSA applicable, (b) a DAB converter with single switching frequency; SSA not applicable, (c) an inverter with SPWM with two distinct frequencies of excitation, (d) an inverter with input LC filter, with two distinct frequencies of excitation

the capacitor voltage. The SSA technique cannot be used where switching level dynamics cannot be ignored. The GAM technique is effective in such an application space, which captures the switching level dynamics [2].

As a next example, a Dual Active Bridge (DAB) converter is shown in Figure 1(b). In this situation, the SSA fails to capture the inductor dynamics as the inductor current waveform (shown in the figure) has a zero dc value and a highly dominant switching frequency component (thus SRA fails too). Therefore, the GAM technique is needed to model the behavior of the leakage inductance dynamics of DAB [4, 19].

A single frequency of excitation is considered in the works described thus far. These frameworks are extended to the second dimension in the works described in the following paragraphs. Inverters and ac-ac converters [20, 21, 22] have two excitation frequencies, namely, the switching frequency and the modulation frequency. In such a scenario, a

uni-dimensional GAM framework cannot support capturing the two frequency components in the system. For example, a single-phase inverter schematic is shown in Figure 1(c). The modulation and switching frequencies are injected into the inverter via the switching signals, and the inverter fabricates the modulation frequency and the subsequent odd harmonics. The switching ripple rides on top of this signal as well. Therefore, the inverter's dynamic model has four frequency categories: the dc, switching frequency, modulation frequency, and sideband components. To facilitate the capturing of these components, two frequencies are to be considered in the two-dimensional GAM (2D-GAM) framework [23, 24, 25, 26].

Although the extension to the second dimension was made in the 2D-GAM framework[23, 16], it can be difficult to model all converter classes with two excitation frequencies with the existing literature. An inverter with an LC filter on the dc side is shown in Figure 1(d) as an example topology. The state variables on the ac side have dc, modulation, and switching components that can be modeled in 2D-GAM. However, the dc side of the inverter possesses the dc, even order modulation harmonics, and the switching components. The Sine Pulse Width Modulation (SPWM) results in the spectral components shown in Figure 2. The spectrum has three types of components: modulation frequency harmonics ($p\bar{f}$), switching frequency harmonics ($r\hat{f}$), and sideband components ($r\hat{f} + p\bar{f}$) where $p \in \mathbb{Z}$, and $r \in \mathbb{W}$. The magnitude of the switching signal is zero at modulation frequency harmonics above the fundamental, which makes them difficult to be considered in 2D-GAM. This paper proposes a novel 2D convolution-based Extended GAM (EGAM) framework, as harmonic components do not naturally manifest in the 2D-GAM framework, and it is difficult to keep track of the manifestations. The proposed framework accounts for the dynamics at the initially considered frequencies and newly manifesting frequencies of the system. Therefore, the main contributions of this work are to develop:

1. A consistent framework for handling the Single Fourier Series (SFS) or Double Fourier Series (DFS) products

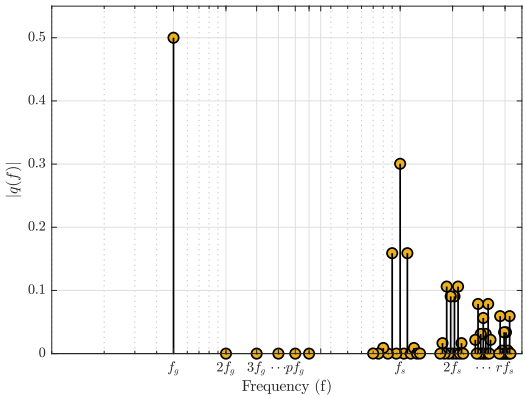

Figure 2. Spectral components in SPWM switching waveform

2. An algorithm for handling 2D convolutions in frequency plane to enable EGAM in numerical ODE solvers

This article is organized as follows: a review of the conventional GAM technique is first presented in Section 2. The idea of Discrete Fourier Images (DFI) is presented in Section 3, succeeded by the Extended GAM modeling technique. The properties of harmonic truncation (a consequence of EGAM) are explored in Section 4. Hardware results for an example single phase inverter in Section 5 are presented to test the model's efficacy, and the results are analyzed.

2. REVIEW OF GAM

In conventional GAM, the time-dependent state variables are transformed to the Fourier coefficients written as Single Fourier Series (SFS) expansions; that is, a periodic signal $x(t)$ in the time domain can be written as

$$x(t) = \sum_{k=-\infty}^{+\infty} x_k e^{jk\omega_0 t} \tag{1}$$

$$\mathbf{C}(t) = \begin{bmatrix} 1 & \cos(\bar{\omega}t) & \sin(\bar{\omega}t) & \cdots & \cos(n\bar{\omega}t) & \sin(n\bar{\omega}t) \end{bmatrix} \tag{2}$$

$$x(t) = \mathbf{C}(t) \cdot \mathbf{x}_k^{\mathsf{T}} \tag{3}$$

where $\mathbf{x}_k$ is the vector of Fourier coefficients

$$\mathbf{x}_k = \begin{bmatrix} x_0 & x_{1c} & x_{1s} & \cdots & x_{nc} & x_{ns} \end{bmatrix} \tag{4}$$

With these base relationships, the framework can be extended for other operators [1, 2, 24] given by

$$\frac{d}{dt}\langle x \rangle_k(t) = \left\langle \frac{d}{dt} x \right\rangle_k (t) - jk\omega_0 \langle x \rangle_k(t) \tag{5}$$

$$\langle xy \rangle_k = \sum_{i=-\infty}^{\infty} \langle x \rangle_{k-i} \langle y \rangle_i \tag{6}$$

the operator $\langle \bullet \rangle_k$ represents the k^{th} harmonic Fourier coefficient of a time domain signal and (6) is a discrete 1D convolution [27].

If the system of interest has two distinct excitation frequencies, namely ω_1, ω_2, the state variable $x(t)$ in the time domain is represented using DFS given by

$$x(t) = \sum_{p \in \mathbb{Z}, r \in \mathbb{W}} \mathrm{x}_{p,r} e^{i(p\omega_1 t + r\omega_2 t)} \tag{7}$$

then it can be converted to the vector containing the Fourier coefficients for a finite number of harmonics as

$$\mathbf{x} = \begin{bmatrix} \mathrm{x}_{0,0} & \mathrm{x}_{1,0c} & \mathrm{x}_{1,0s} & \cdots & \mathrm{x}_{0,1c} & \mathrm{x}_{0,1s} & \cdots & \mathrm{x}_{p,rc} & \mathrm{x}_{p,rs} \end{bmatrix} \tag{8}$$

where, $\mathrm{x}_{p,0c}$, $\mathrm{x}_{p,0s}$ belong to the Fourier coefficients of the harmonics of ω_1; $\mathrm{x}_{0,rc}$, $\mathrm{x}_{0,rs}$ belong to coefficients of the harmonics of ω_2, and $\mathrm{x}_{p,rc}$, $\mathrm{x}_{p,rs}$ belong to coefficients of the harmonics of $p\omega_1 + r\omega_2$ components. The subscripts c and s correspond to the cos and sin terms of the DFS expansion in rectangular form.

In order to extend the GAM framework to 2D-GAM, (5) is rewritten as

$$\frac{dx(t)}{dt} = \mathbf{C}(t)\left(\frac{d\mathbf{x}}{dt} + \mathbf{T}\mathbf{x}\right) \tag{9}$$

where the DFS coefficients of the expansion are stored in the state variable $\mathbf{x}$ (8) and the matrix $\mathbf{T}$ stores the frequency information at the state variable $\mathrm{x}_{p,r}$. Therefore, $\mathbf{T}$ is the matrix version of the second term of GAM (5) given by

$$\mathbf{T}_{(2k,2k+1)} = (\mathbf{m}_{k+1}\omega_1 + \mathbf{n}_{k+1}\omega_2) \tag{10}$$

$$\mathbf{T}_{(2k+1,2k)} = -(\mathbf{m}_{k+1}\omega_1 + \mathbf{n}_{k+1}\omega_2) \tag{11}$$

where $k \in \mathbb{N}^O$, indexes the vectors $\mathbf{m} \in \mathbb{Z}^{O+1}$,and $\mathbf{n} \in \mathbb{W}^{O+1}$. Dimensionally, $\mathbf{T}$ is a $(2O+1) \times (2O+1)$ sparse matrix [23]. O is the total number of distinct frequencies and harmonic combinations considered, excluding the dc term and $k \in \{1, 2, \cdots O\}$. Vectors $\mathbf{m}$ and $\mathbf{n}$ have an order of one more than the distinct frequencies (O) to account for the dc term, which is always the first entry from an indexing viewpoint. With these base equations, a first-order differential equation of the form

$$\frac{dx(t)}{dt} = ax(t) + by(t) \tag{12}$$

can be rewritten in the Fourier coefficients and using (3)

$$\left\langle \frac{dx(t)}{dt} \right\rangle = a\langle x(t)\rangle + b\langle y(t)\rangle \tag{13}$$

$$\frac{d\mathbf{x}}{dt} = (a\mathbf{I} - \mathbf{T})\mathbf{x} + b\mathbf{y} \tag{14}$$

where $\mathbf{x}$, $\mathbf{y}$ are Fourier coefficient vectors at the same frequencies. Applying the same procedure on a more complicated base first-order ordinary differential equation

$$\frac{dx(t)}{dt} = ax(t) + bx(t)y(t) \tag{15}$$

$$\frac{d\mathbf{x}}{dt} = (a\mathbf{I} - \mathbf{T})\mathbf{x} + b(\mathbf{x} * \mathbf{y}[\ell]) \tag{16}$$

Eq. (16) can then be expanded for the desired number of harmonics (by writing for each harmonic order, $\ell \in (1, 2, \cdots, O)$) to finally give

$$\frac{d}{dt}\begin{bmatrix} x_0 \\ x_{1c} \\ x_{1s} \\ \vdots \\ x_{lc} \\ x_{ls} \end{bmatrix} = \begin{bmatrix} a & 0 & 0 & 0 & \cdots & 0 \\ 0 & a & -\omega_1 & 0 & \cdots & 0 \\ 0 & \omega_1 & a & 0 & \cdots & 0 \\ \vdots & \vdots & \vdots & \ddots & \vdots & \vdots \\ 0 & 0 & 0 & 0 & a & -\omega_l \\ 0 & 0 & 0 & 0 & \omega_l & a \end{bmatrix} \begin{bmatrix} x_0 \\ x_{1c} \\ x_{1s} \\ \vdots \\ x_{lc} \\ x_{ls} \end{bmatrix} + b \begin{bmatrix} \sum_{u=-\infty}^{\infty} x[u]y[-u] \\ \Re\left\{\sum_{u=-\infty}^{\infty} x[u]y[1-u]\right\} \\ \Im\left\{\sum_{u=-\infty}^{\infty} x[u]y[1-u]\right\} \\ \vdots \\ \Re\left\{\sum_{u=-\infty}^{\infty} x[u]y[l-u]\right\} \\ \Im\left\{\sum_{u=-\infty}^{\infty} x[u]y[l-u]\right\} \end{bmatrix} \tag{17}$$

In (15), the product of two SFS terms, $x(t)y(t)$, translated to 1D discrete convolution on the frequency plane for the Fourier coefficient vectors $\mathbf{x}$, $\mathbf{y}$ [1, 28, 2, 26, 25]. The translation from the time domain to the frequency domain for the multiplication of two terms expressed as DFS is not reported in the literature. Although [26] considered a three-phase inverter with an input LC filter, the article only considers the existing spectral components in the SPWM waveform and does not accommodate newly manifesting harmonics. Also, [29] notes that the multiplication of two DFS terms must be considered in the future and points out that the authors did not view the product terms in their work. This crucial result is needed to accurately capture the dynamic performance of many power electronic converters, where a switching term multiplies over a state variable, as in the case of an inverter with an LC filter on the dc side. Although more recent work in microgrids [16] considers dc filter

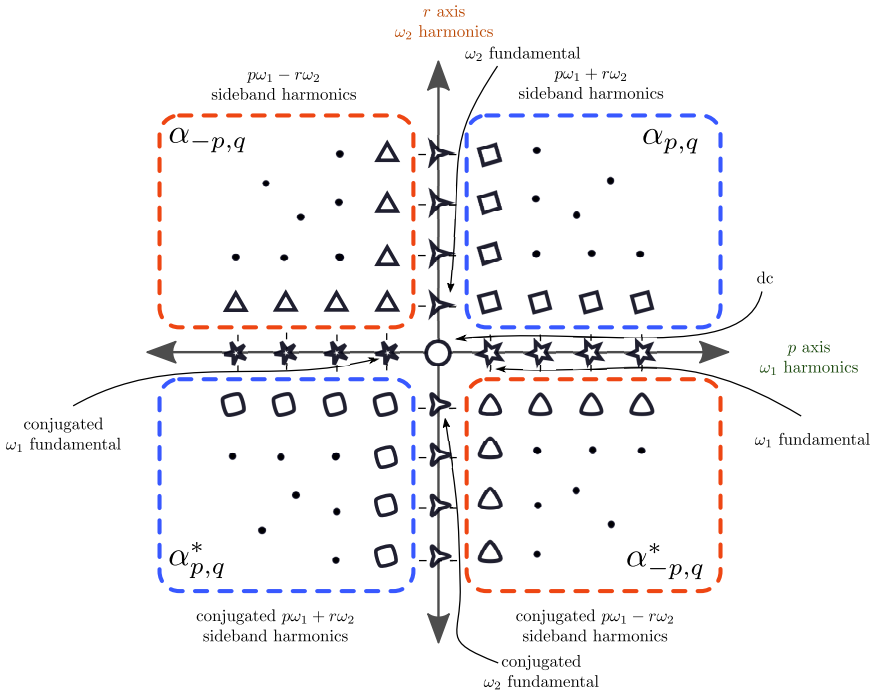

Figure 3. Two dimensional DFI signal representation

dynamics, it does not explain how similar relationships are derived for other harmonics in an organized way. The following section discusses the process of handling the product of two DFS terms and lays the foundation for EGAM.

3. EXTENDED GAM WITH DISCRETE FOURIER IMAGES

In a one-dimensional case, the product of two state vectors consisting of coefficients in the time domain will imply convolution in the frequency domain [27], a direct consequence of the convolution theorem. A corollary can be stated in this regard,

Corollary *The product of two sinusoidal signals of the same period produces a waveform with Fourier coefficients matching the discrete convolution of the original signals in the frequency domain.*

Most works listed so far only consider a select number of terms to compute the product terms while neglecting the others. When multiple fundamental frequencies of operation are considered, as in an inverter, the convolution operator becomes very complicated, and a concrete methodical way of resolving the products must be devised.

To handle the product terms, a two-dimensional extension can be made to the already existing Corollary 3.1 and can be restated as,

Corollary *The product of two sinusoidal signals, with two distinct periods, produces a waveform with Fourier coefficients matching the two-dimensional discrete convolution of the original signals in the frequency domain.*

Based on corollary 3.2, the frequency component vectors must be convolved over two dimensions to obtain the resulting component vector. However, the Fourier vector must be transformed to a discrete frequency plane, where the Fourier components must be placed before the 2D convolution is applied. Proof for Corollary 3.2 is provided in Appendix 3. The following subsections describe a methodical way to place and keep track of new harmonics when there are two distinct excitation frequencies.

3.1. DISCRETE FOURIER IMAGE SIGNAL

The vector **x** (8) can be separated into two new vectors consisting of the coefficients of c and s subscripts to give

$$\begin{aligned} \mathbf{a} &= \begin{bmatrix} x_{0,0} & x_{1,0c} & \cdots & x_{0,1c} & \cdots & x_{p,rc} \end{bmatrix} \\ \mathbf{b} &= \begin{bmatrix} 0 & x_{1,0s} & \cdots & x_{0,1s} & \cdots & x_{p,rs} \end{bmatrix} \end{aligned} \tag{18}$$

where the dc term is accounted into the c vector term and the corresponding value in **b** is left to zero. The vectors (18) can then be converted to complex notation for each harmonic index given using the transformation

$$\alpha_{p,r} = \begin{cases} a_0, \text{for } p = 0, r = 0 \\ \frac{1}{2}(a_g - \mathrm{i}b_g), \text{ otherwise} \end{cases} \tag{19}$$
$$\alpha^*_{(p,r)} = \frac{1}{2}(a_g + \mathrm{i}b_g)$$

The subscripts of each element of $\mathbf{a}$, $\mathbf{b}$ ($x_{\bullet,\bullet}$) indexed by $g \in \mathbb{N}$ get carried over to the subscripts of $\alpha_{\bullet,\bullet}$, and $\alpha^*_{\bullet,\bullet}$. The calculated components can then be placed on an image space to represent a 2D signal corresponding to the Fourier coefficients at the discrete instances of the harmonic numbers as shown in Figure 3. As the two frequencies of the signal are distinct, each Fourier coefficient can be placed in a distinct location on the 2D image plane formed by ω_1 and ω_2 axes. This forms the basis for the rest of the discussion in this article.

A matrix can then be generated based on Figure 3 and is given by

$$\mathbf{F} = \begin{bmatrix} \alpha_{-p,r} & \cdots & \alpha_{-1,r} & \alpha_{0,r} & \alpha_{1,r} & \cdots & \alpha_{p,r} \\ \vdots & \ddots & \ddots & \vdots & \iddots & \iddots & \vdots \\ \alpha_{-p,1} & \ddots & \alpha_{-1,1} & \alpha_{0,1} & \alpha_{1,1} & \iddots & \alpha_{p,1} \\ \alpha^*_{p,0} & \cdots & \alpha^*_{1,0} & \alpha_{0,0} & \alpha_{1,0} & \cdots & \alpha_{p,0} \\ \alpha^*_{p,1} & \iddots & \alpha^*_{1,1} & \alpha^*_{0,1} & \alpha^*_{-1,1} & \ddots & \alpha^*_{-p,1} \\ \vdots & \iddots & \iddots & \vdots & \ddots & \ddots & \vdots \\ \alpha^*_{p,r} & \cdots & \alpha^*_{1,r} & \alpha^*_{0,r} & \alpha^*_{-1,r} & \cdots & \alpha^*_{-p,r} \end{bmatrix} \tag{20}$$

where $\mathbf{F}$ is referred to as the *Discrete Fourier Image* (DFI) [30] of Fourier coefficient vector $\mathbf{x}$. The DFI has nine regions, differentiated by different symbols, as seen in the DFI image shown in Figure 3. A legend for each symbol corresponding to each harmonic component with their p and r axis values is given in Table 1

Now, using Corollary 3.2, two Fourier coefficient vectors $\mathbf{x}$, and $\mathbf{y}$ can be 2D convolved to get a larger matrix. These relations are mathematically given by

$$x(t) \overset{\mathcal{F}}{\longleftrightarrow} \mathbf{x} \overset{\text{DFI}}{\longleftrightarrow} \mathbf{F_x} \tag{21}$$

$$y(t) \overset{\mathcal{F}}{\longleftrightarrow} \mathbf{y} \overset{\text{DFI}}{\longleftrightarrow} \mathbf{F_y} \tag{22}$$

$$z(t) \overset{\mathcal{F}}{\longleftrightarrow} \mathbf{z} \overset{\text{DFI}}{\longleftrightarrow} \mathbf{F_z} \tag{23}$$

$$z(t) = x(t)y(t) \overset{\text{DFI}}{\longleftrightarrow} \mathbf{F_z} = \mathbf{F_x} * * \mathbf{F_y} \tag{24}$$

where $\mathcal{F}$ is the Fourier series coefficient extraction operation from the time domain signal $\bullet(t)$. The resulting matrix $\mathbf{F}_z$ is converted back to the vector $\mathbf{z}$ by using the transformation

$$\begin{aligned} h_g &= \begin{cases} \alpha_{0,0}, \text{for } p = 0, r = 0 \\ \alpha_{p,r} + \alpha^*_{p,r} \text{ otherwise} \end{cases} \\ s_g &= \mathrm{i}(\alpha_{p,r} - \alpha^*_{p,r}) \end{aligned} \tag{25}$$

The resulting values are populated in $\mathbf{h}$, $\mathbf{s}$ and redistributed in the proper harmonic order as that of (8) to form the vector $\mathbf{z}$, which is the resulting vector of the 2D convolution.

Before proceeding with the subsequent sections, an essential distinction between convolution operators should be made. The 2D convolution and Corollary 3.2 are applied when the vector is converted to DFI as shown in Figure 3. Therefore, to simplify the notation, for vectors $\mathbf{x}$, and $\mathbf{y}$, a new notation $\mathbf{x} \circledast \circledast \mathbf{y}$ is defined to mean $\mathbf{z}$, which is converted using (25) on $\mathbf{F_x} * * \mathbf{F_y}$. That is, $\circledast \circledast$ represents the complete process of rectangular to complex DFI to double convolution and back to rectangular form.

For systems excited by two different base fundamental frequencies, such as in the case of an inverter, the vector $\mathbf{x}$ is extended to capture multiple baseband harmonics and the sidebands harmonics by their respective DFS expansions. However, in [23, 24], the expansion

Table 1. Legend for DFI components in Figure 3

Component	Axis	Symbol
dc component	$p = 0; r = 0$	○
ω_1 harmonics	$p \in \mathbb{Z}^+; r = 0$	☆
ω_2 harmonics	$p = 0; r \in \mathbb{Z}^+$	➤
ω_1, ω_2 sidebands	$p \in \mathbb{Z}^+; r \in \mathbb{Z}^+$	□
$-\omega_1, \omega_2$ sidebands	$p \in \mathbb{Z}^-; r \in \mathbb{Z}^+$	△
ω_1 harmonics' conjugates	$p \in \mathbb{Z}^+; r = 0$	✱
ω_2 harmonics' conjugates	$p = 0; r \in \mathbb{Z}^+$	➢
ω_1, ω_2 sidebands' conjugates	$p \in \mathbb{Z}^+; r \in \mathbb{Z}^+$	▢
$-\omega_1, \omega_2$ sidebands' conjugates	$p \in \mathbb{Z}^-; r \in \mathbb{Z}^+$	△

for the product of two state vectors written as DFS is not provided as indicated earlier in Section 2. Also, the authors make simplifying assumptions to avoid the multiplication terms by neglecting state variables that multiply with a switching term by choosing simpler topologies. In [26, 25], however, the dc side filters in the inverter are modeled. The authors consider only a few harmonics in their 2D-GAM model and do not consider even harmonics of the modulation signal.

Referring back to (15), and assuming $x(t)$ and $y(t)$ to be DFS expansions instead of SFS, (16) can be expanded into the second dimension by

$$\frac{d\mathbf{x}}{dt} = (a\mathbf{I} - \mathbf{T})\mathbf{x} + b(\mathbf{x} \circledast \circledast \mathbf{y}) \tag{26}$$

Table 2. EGAM operations set

Operation	Time Domain	Frequency Domain
Scalar Product	$ax(t)$	$a\mathbf{x}$
Summation	$x(t) + y(t)$	$\mathbf{x} + \mathbf{y}$
Differentiation	$\frac{dx(t)}{dt}$	$\left(\frac{d\mathbf{x}}{dt} + \mathbf{T}\mathbf{x}\right)$
Multiplication	$x(t)y(t)$	$\mathbf{x}\circledast \circledast\mathbf{y}$

This completes the EGAM formulation that is capable of handling DFS products. A complete set of the time domain to EGAM translations is shown in Table 2 for clarity. The following subsection shows an algorithm for handling DFS products in Ordinary Differential Equation (ODE) solvers for making EGAM implementable with the MATLAB simulation software package.

3.2. CONVOLUTION ALGORITHM FOR ODE SOLVERS

An algorithm is proposed for computing the 2D convolution of the Fourier image signals in each processing cycle of a numerical ODE solver.

A step-by-step process for the DFI convolution algorithm is shown in Figure 4. In the first step, the vectors **x** and **y** are first imported from the ODE process call. The imported vectors are then split into real and imaginary component vectors shown by the subscripts $\mathbb{R}$, $\mathbb{I}$ in the second step. The split vectors are transformed into the corresponding DFI in the third step. In the fourth step, the 2D convolution operator is applied to the two DFIs, and the resultant DFI is shown. The size of the resulting matrix is larger than both of the individual input matrices. Therefore, to restrict the length of the resultant vector, the new harmonics cropping up are neglected in the fifth step to prevent the growth of vectors as the ODE solver progresses. This method of ignoring harmonic components beyond the allowed size of the input vectors is referred to as *harmonic truncation*. The effects of making the harmonic truncation approximation will be studied in further detail in the next section. The truncated DFI is transformed into the real and imaginary component vectors, merged into

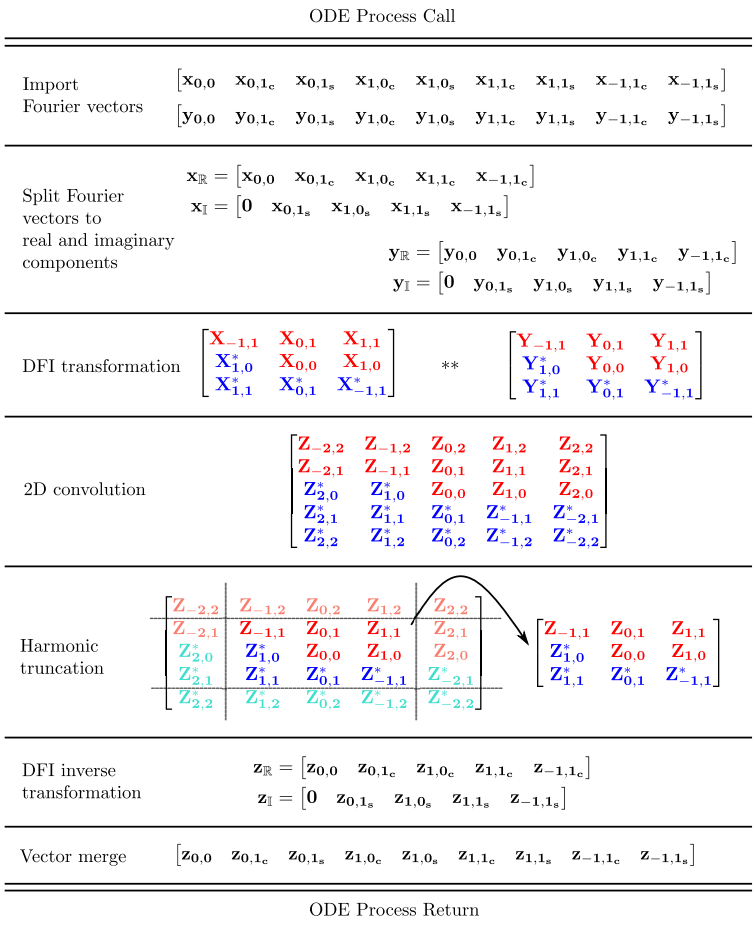

Figure 4. Proposed convolution algorithm for resolving $z = \mathbf{x} \circledast \circledast \mathbf{y}$ in an ODE solver

one contiguous vector in the last step, and handed over to the ODE process. A MATLAB toolbox is developed for systematically performing the 2D convolution computations and is shared publicly as a GitHub project in Appendix 1.6 to aid future implementations.

4. HARMONIC TRUNCATION

When two DFI signals are convolved, the size of the resulting DFI ($\mathbf{F_z}$) increases indicating the evolution of new harmonic components. However, if the size of the DFI increases, it will also increase the resulting Fourier coefficient vector length and will impose further requirements on the memory allocation aspects in the ODE solver front. To alleviate this issue, harmonic truncation is necessary to restrict the growth of the size of the $\mathbf{F_z}$ matrix.

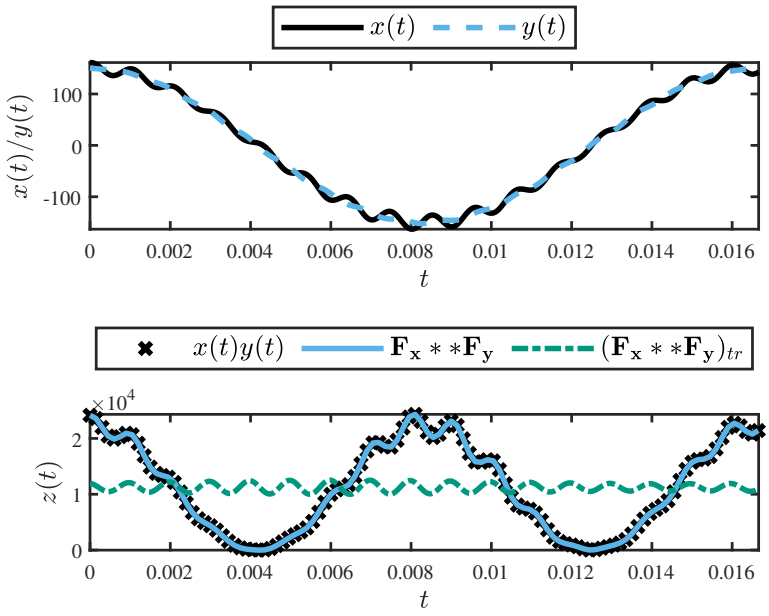

Figure 5. Detrimental effects of harmonic truncation; p axis restricted to fundamental harmonic

However, the harmonic truncation approximation may not be a viable technique always as it depends on the relative scales of amplitudes of the DFI signals. Two examples are provided in this section: one where the process of harmonic truncation shows a detrimental behavior and the other where it is a reasonable approximation.

4.1. DETRIMENTAL EFFECTS OF HARMONIC TRUNCATION

Consider $x(t)$ and $y(t)$ to be two input signals as functions of ω_1 and ω_2, given by

$$x(t) = 150\cos(\omega_1 t) - 1.5\cos(\omega_2 t) + 2.5\cos(\omega_1 t + \omega_2 t) + 10\cos(-\omega_1 t + \omega_2 t) - 1.75\sin(-\omega_1 t + \omega_2 t) \quad (27)$$

$$y(t) = 150\cos(\omega_1 t) + 1.5\sin(\omega_2 t) - 1.5\sin(\omega_1 t + \omega_2 t) + 0.75\sin(-\omega_1 t + \omega_2 t) \quad (28)$$

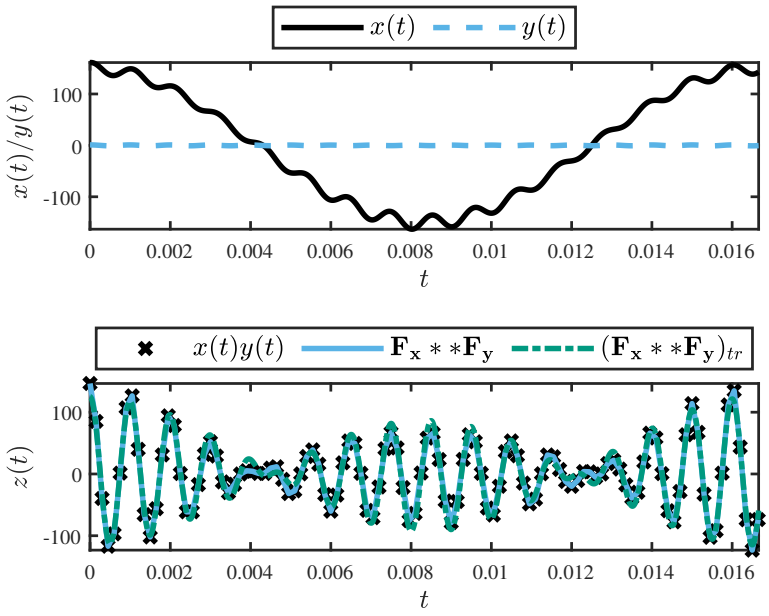

Figure 6. Good approximation by harmonic truncation; p axis restricted to fundamental harmonic

Figure 5 shows the two input signals described in (27) and (28) and the actual product $z(t) = x(t)y(t)$. Also shown are the truncated and un-truncated time domain reconstructions of the two DFI signals represented by $\mathbf{F}_{\mathbf{z}tr} = (\mathbf{F_x} * * \mathbf{F_y})_{tr}$ and $\mathbf{F_z} = \mathbf{F_x} * * \mathbf{F_y}$ respectively. The two signals (27), (28) have a dominant ω_1 component, and their product will have a dominant $2\omega_1$ component. To capture the second-order components, the DFI needs to be extended by an extra harmonic order on the p (ω_1) axis, which is one order higher than the original sizes of the input DFIs $\mathbf{F_x}$, and $\mathbf{F_y}$. If this harmonic order extension is not done, the crucial $2\omega_1$ feature of the resulting product signal $z(t)_{tr}$ will be lost and the truncated 2D convolution of the DFI leads to a drastically different result when compared to the case where the $2\omega_1$ components are considered (as indicated by the untruncated DFI reconstruction in Figure 5).

4.2. GOOD HARMONIC TRUNCATION

In this example, two signals are again selected, where the first operator $x(t)$ is the same as in (27). But $y(t)$ is replaced with

$$y(t) = 0.01\cos(\omega_1 t) + 0.7\cos(\omega_2 t) + 0.1\cos(\omega_1 t + \omega_2 t) + 0.1\cos(-\omega_1 t + \omega_2 t) \quad (29)$$

Figure 6 shows the two input signals described in (27) and (29) and the actual product $z(t) = x(t)y(t)$. This case however shows a close match between $z(t)$ and the reconstructions of $\mathbf{F_z}$, and $\mathbf{F}_{\mathbf{z}tr}$ DFIs. The close match is attributed to non-dominant $2\omega_1$ components due to the high order difference between the Fourier coefficients of the ω_1 components of $x(t)$ and $y(t)$.

This shows that essential features of the product signals can be lost if dominant harmonics lie outside the region of harmonic order approximation. Therefore, the system designer must know the entire range of dominant harmonics before deciding on the truncation region in EGAM. If dominant harmonics are neglected, the dynamic behavior of the model will be significantly different from the actual detailed/hardware model.

5. EXPERIMENTAL VALIDATION

A single-phase inverter is used to test the validity of the DFI convolution algorithm. A schematic of the inverter is shown in Figure 7. The inverter has an input LC filter to filter the input current ripple and an LC-filtered output for the load resistance R. The input filter has an inductor L_1, capacitor C_1, and the output filter has an inductor L_2, capacitor C_2. The series resistance of both the filter inductors, R_L, is assumed to be the same.

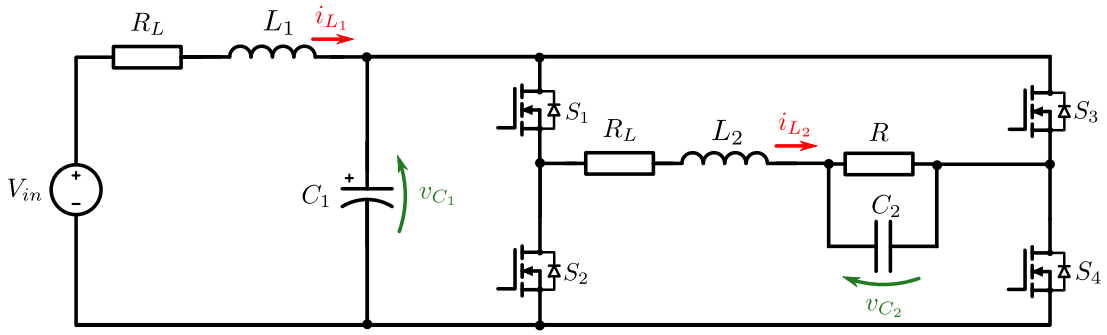

Figure 7. Single phase inverter

5.1. FORMATION OF EGAM MODEL FOR SINGLE-PHASE INVERTER

Based on the schematic, four state equations can be written for the converter in the time domain for the dynamic elements L_1, C_1, L_2, and C_2 having state variables i_{L_1}, v_{C_1}, i_{L_2}, and v_{C_2} which are given by

$$\begin{aligned}
\frac{di_{L_1}(t)}{dt} &= -\frac{R_L}{L_1} i_{L_1}(t) - \frac{v_{C_1}(t)}{L_1} + \frac{V_{in}}{L_1} \\
\frac{dv_{C_1}(t)}{dt} &= \frac{i_{L_1}(t)}{C_1} - \frac{i_{L_2}(t)}{C_1}(q_+(t) - q_-(t)) \\
\frac{di_{L_2}(t)}{dt} &= \frac{v_{C_1}(t)}{L_2}(q_+(t) - q_-(t)) - \frac{R_L}{L_2} i_{L_2}(t) - \frac{v_{C_2}(t)}{L_2} \\
\frac{dv_{C_2}(t)}{dt} &= \frac{i_{L_2}(t)}{C_2} - \frac{v_{C_2}(t)}{RC_2}
\end{aligned} \tag{30}$$

In (30) $q_+(t)$, and $q_-(t)$ are the switching functions originating from the SPWM of the H-bridge. In the switching expression, the symbols $\overline{f}$ and $\hat{f}$ represent the modulation frequency and the switching frequency respectively. Similarly, the symbols, p, and r denote the harmonic indices of $\overline{f}$, and $\hat{f}$. The DFS expansion consists of the modulation frequency and its harmonics (i.e., $p\overline{f}$), switching frequency, and its harmonics (i.e., $r\hat{f}$).

The DFS expansion for the SPWM signal is presented in (31), wherein the coefficients $q_{p,r}$ are provided in [23], which are repeated in (32).

$$q(t) = \sum_{p,r\in\mathbb{Z}} q_{p,r} e^{i(p\omega_1 t + r\omega_2 t)} \tag{31}$$

$$
\begin{aligned}
q_{0,0} &= \frac{1}{2} \\
q_{1,0c} &= \frac{1}{2} m_{1,0c} \\
q_{1,0s} &= \frac{1}{2} m_{1,0s} \\
q_{p,rc} &= \frac{2}{p\pi} \sin\left(\frac{\pi(p+q)}{2}\right) J_p(y_r) \cos\left(p\bar{\phi} + r\hat{\phi}\right) \\
q_{p,rs} &= -\frac{2}{p\pi} \sin\left(\frac{\pi(p+q)}{2}\right) J_p(y_r) \sin\left(p\bar{\phi} + r\hat{\phi}\right) \\
y_x &= \frac{x\pi}{2} \sqrt{m_{1,0c}^2 + m_{1,0s}^2} \\
\bar{\phi} &= \arg(m_{1,0c} - j m_{1,0s}) \\
m_{1,0} &= \sqrt{m_{1,0c}^2 + m_{1,0s}^2}
\end{aligned}
\tag{32}
$$

$q_{0,0}$, $q_{1,0c/s}$ are the dc and modulation frequency components of the SPWM signal. $m_{1,0c}$, $m_{1,0s}$ are the cos and sin projections of the modulation index $m_{1,0}$ along the angle $\bar{\phi}$, which is the phase of the modulation signal. The cos and sin coefficients of switching frequency and sideband components of the switching signal are computed in $q_{p,rc}$, and $q_{p,rs}$, respectively. $J_\bullet(\bullet)$ is the Bessel function of the first kind.

Now, the time domain equations for the inverter system in (30) are rewritten in the frequency domain using the already existing relation (9) for derivatives and the newly proposed DFI convolution equation in (24) for products yield

$$
\frac{d\mathbf{i}_{L_1}}{dt} = -\left(\frac{R_L}{L_1}\mathbf{I} + \mathbf{T}\right)\mathbf{i}_{L_1} - \frac{1}{L_1}\mathbf{v}_{C_1} + \frac{V_{in}}{L_1}\mathbf{\Gamma} \tag{33}
$$

$$
\frac{d\mathbf{v}_{C_1}}{dt} = \frac{1}{C_1}\mathbf{i}_{L_1} - \frac{1}{C_1}(2\mathbf{i}_{L_2} \circledast\circledast \mathbf{q}_+ - \mathbf{i}_{L_2} \circledast\circledast \mathbf{\Gamma}) - \mathbf{T}\mathbf{v}_{C_1} \tag{34}
$$

$$
\frac{d\mathbf{i}_{L_2}}{dt} = \frac{1}{L_2}(2\mathbf{v}_{C_1} \circledast\circledast \mathbf{q}_+ - \mathbf{v}_{C_1} \circledast\circledast \mathbf{\Gamma}) - \left(\frac{R_L}{L_2}\mathbf{I} + \mathbf{T}\right)\mathbf{i}_{L_2} - \frac{1}{L_2}\mathbf{v}_{C_2} \tag{35}
$$

$$
\frac{d\mathbf{v}_{C_2}}{dt} = \frac{\mathbf{i}_{L_2}}{C_2} - \left(\frac{1}{RC_2}\mathbf{I} + \mathbf{T}\right)\mathbf{v}_{C_2} \tag{36}
$$

where $\mathbf{\Gamma} = \begin{bmatrix} 1 & 0 & 0 & \cdots & 0 \end{bmatrix}^{\mathrm{T}}$ and $\mathbf{I}$ is the identity matrix. As the input voltage V_{in} is dc, it only operates over the dc terms. Also, the switching terms $\mathbf{q}_+$ and $\mathbf{q}_-$ are complementary and therefore, $(\mathbf{q}_+ - \mathbf{q}_-)$ is replaced by $(2\mathbf{q}_+ - \mathbf{\Gamma})$[23].

As the inverter has both an input and an output filter, even harmonics of the modulation frequency are also to be considered for accurately capturing the dynamics of L_1 and C_1. In this work, one switching harmonic, and four modulation harmonics are considered, resulting in the Fourier vectors for each state $\mathbf{x}$.

$$\begin{aligned} \mathbf{x} = [&x_{0,0},\ x_{1,0c},\ x_{1,0s}\ x_{2,0c},\ x_{2,0s},\ x_{3,0c},\ x_{3,0s}\ x_{4,0c},\ x_{4,0s} \\ &x_{1,1c},\ x_{1,1s}\ x_{-1,1c},\ x_{-1,1s}\ x_{2,1c},\ x_{2,1s}\ x_{-2,1c},\ x_{-2,1s} \\ &x_{3,1c},\ x_{3,1s}\ x_{-3,1c},\ x_{-3,1s}\ x_{4,1c},\ x_{4,1s}\ x_{-4,1c},\ x_{-4,1s}] \end{aligned}$$

The resulting DFI for the vector $\mathbf{x}$ turns out to be $\mathbf{F_x}$ given by

$$\mathbf{F_x} = \begin{bmatrix} \alpha_{-4,1} & \alpha_{-3,1} & \alpha_{-2,1} & \alpha_{-1,1} & \alpha_{0,1} & \alpha_{1,1} & \alpha_{2,1} & \alpha_{3,1} & \alpha_{4,1} \\ \alpha^*_{4,0} & \alpha^*_{3,0} & \alpha^*_{2,0} & \alpha^*_{1,0} & \alpha_{0,0} & \alpha_{1,0} & \alpha_{2,0} & \alpha_{3,0} & \alpha_{4,0} \\ \alpha^*_{4,1} & \alpha^*_{3,1} & \alpha^*_{2,1} & \alpha^*_{1,1} & \alpha^*_{0,1} & \alpha^*_{-1,1} & \alpha^*_{-2,1} & \alpha^*_{-3,1} & \alpha^*_{-4,1} \end{bmatrix} \tag{37}$$

5.2. HARDWARE SETUP

An Imperix power test bench was used to test the validity of the EGAM model. The laboratory setup of the system is shown in Figure 8. A rapid prototyping controller sends the switching modules' gate drive signals via optical channels. The inverter comprises two half-bridge switching modules with Silicon Carbide MOSFETs rated for 800 V and

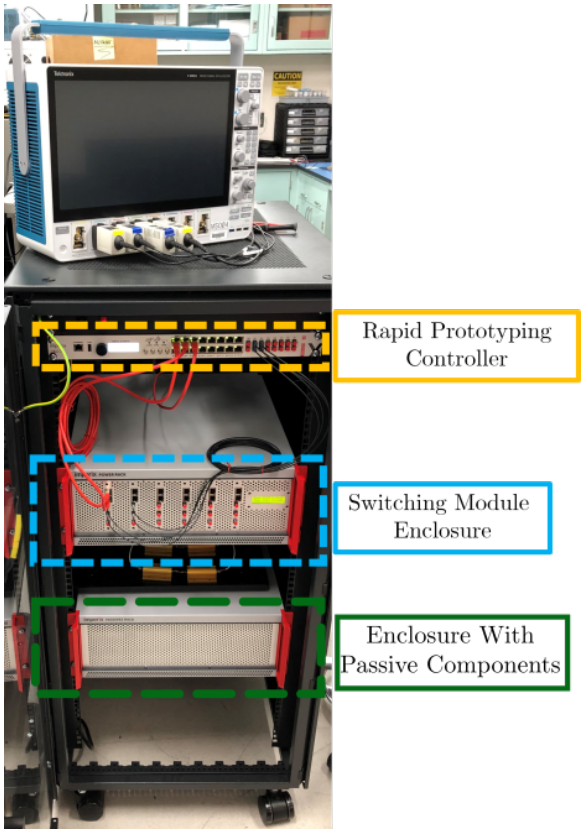

Figure 8. Imperix system setup for a single phase inverter experimentation

24 A. Table 3 presents the parameters of the inverter system test-bed. The components were chosen so that hardware dynamics and mathematical dynamics would coincide without being influenced by the values used to obtain the results.

Two tests are performed on the inverter. These are:

1. The Start-up test
2. Modulation index step test

Details are provided for the tests mentioned above in the following two subsections.

Table 3. Inverter system parameters

Input filter inductor, L_1	2.2 mH
Output filter inductor, L_2	2.2 mH
Input filter capacitor, C_1	520 µF
Output filter capacitor, C_2	10 µF
Load resistance, R	45 Ω
Inductor resistance, R_L	87 mΩ
Modulation frequency $\bar{f}$	50 Hz
Switching frequency, $\hat{f}$	10 kHz
Modulation signal phase, $\bar{\phi}$	Dependent on hardware test phase
Carrier signal phase, $\hat{\phi}$	0 rad

5.3. THE START-UP TEST

Table 4 provides the startup test parameters. The input voltage is first given on the dc side. A step enable causes the SPWM signals to be applied to the inverter model. The subsequent dynamics are shown in Figure 9a - Figure 9d.

The DFI in the EGAM model accounts for four harmonics on the modulation side and one on the switching side. Therefore, both the dc and ac side harmonics are visible. The dc side is expected to have even order harmonics visible on the dc side. The experimental results show excellent congruence with the results obtained by the EGAM and PLECS models. Thus, the effectiveness of the proposed EGAM model is demonstrated.

Table 4. Startup test parameters

Parameter	Value
V_{in}	50 V
Modulation Index	0.75
ω_1 harmonic count	4
ω_2 harmonic count	1

Table 5. Modulation step test parameters

Parameter	Value
V_{in}	50 V
Modulation index initial	0.75
Modulation index final	0.85
ω_1 harmonic count	4
ω_2 harmonic count	1

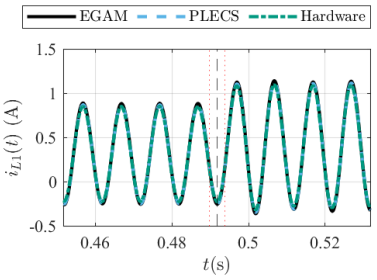

(a) dc side inductor current

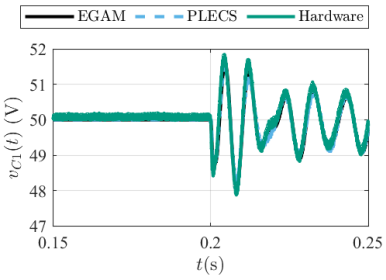

(b) dc side capacitor voltage

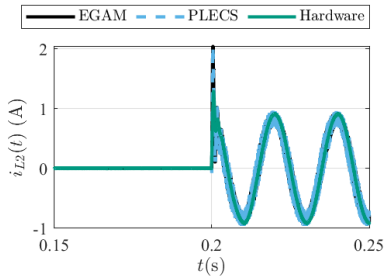

(c) ac side inductor current

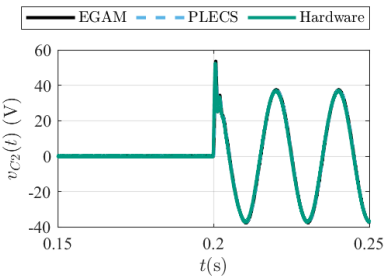

(d) ac side capacitor voltage

Figure 9. EGAM, PLECS, and hardware comparison results for startup transient test

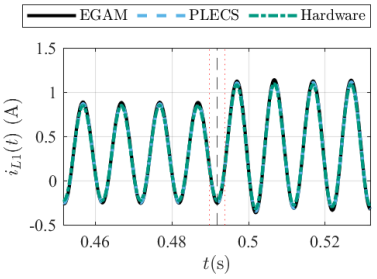

(a) dc side inductor current

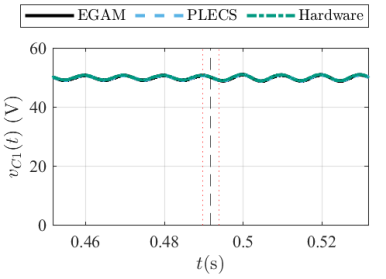

(b) dc side capacitor voltage

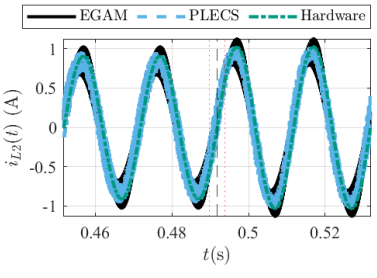

(c) ac side inductor current

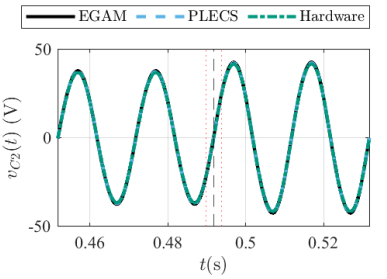

(d) ac side capacitor voltage

Figure 10. EGAM, PLECS, and hardware comparison for modulation step transient test

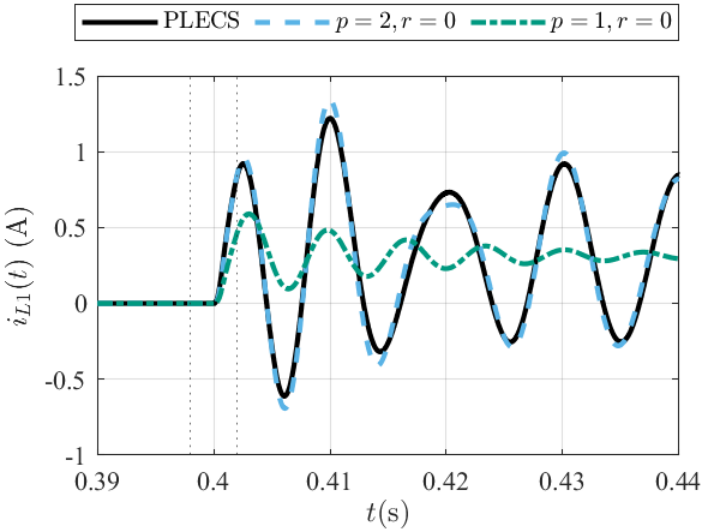

Figure 11. Harmonic truncation effects on dc inductor current

5.4. MODULATION STEP TEST

Table 5 shows the modulation step test parameters. After attaining a steady state with an initial value of the modulation index, a step change is applied to it. The subsequent dynamics are presented in Figure 10a - Figure 10d. Again, the results obtained with the EGAM model are a very good agreement with those obtained with the PLECS and hardware models.

5.5. EFFECT OF HARMONIC TRUNCATION

Two cases with different levels of harmonic truncation are used to demonstrate the importance of choosing the correct truncation sizes for attaining appropriate modeling accuracy, as explained in Section 4. Switching harmonics are neglected in this test to focus on the modulation signal's performance. The startup test results of the dc side inductor L_1 are shown in Figure 11 to do a deeper study on harmonic truncation effects.

The dc side inductor current in an inverter is known to have components at twice the modulation frequency. If the harmonics in EGAM are considered for $p = 1, r = 0$, the resulting dynamic performance is very poor and does not match the actual PLECS simulation. This poor performance is attributed to harmonic truncation, which leads to the loss of features in the state variable at twice the modulation frequency, thereby underscoring the detrimental effects of harmonic truncation. As the DFI in the EGAM for this case at least has the dc component, the waveform is seen to track the average behavior of the PLECS simulation waveform.

On the other hand, when EGAM is rerun for $p = 2, r = 0$, the harmonic truncation encompasses the components at twice the modulation frequency. The features are preserved in the state variables, thereby making harmonic truncation a good approximation. The same behavior can be shown for the dc side capacitor as well.

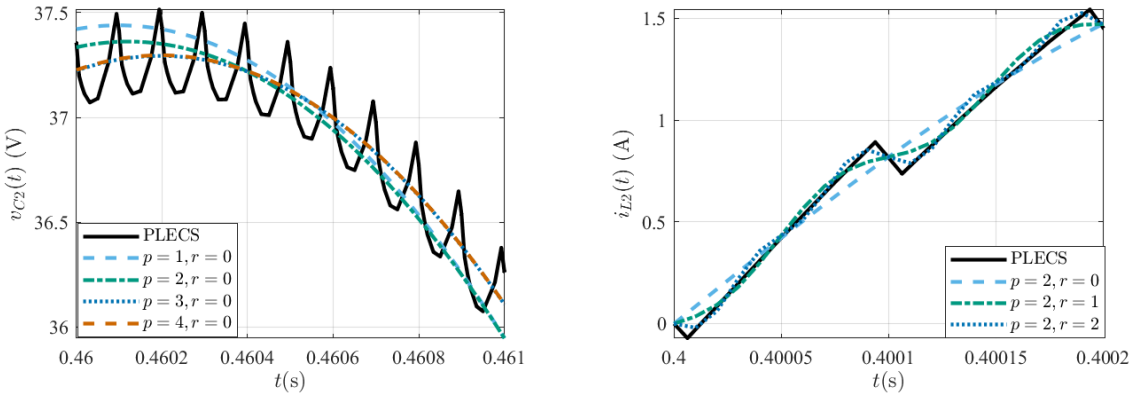

(a) Modulation harmonics' performance

(b) Switching harmonics' performance

Figure 12. Effect of increasing harmonics in EGAM simulation

Table 6. EGAM performance comparison to increase in modulation harmonics

Case	**MAE (PLECS vs EGAM)**	**% improvement over first case**
$p = 1, r = 0$	0.18020	0
$p = 2, r = 0$	0.17272	4.151
$p = 3, r = 0$	0.12563	30.285
$p = 4, r = 0$	0.12570	30.242

5.6. HARMONIC EFFECTS ON MODEL ACCURACY

EGAM increases model accuracy if more harmonics are included. Two examples show an increase in model accuracy as more harmonics are included individually in each axis of the DFI. To compare EGAM simulations analytically, *Mean Absolute Error* (MAE) is computed between PLECS-simulated (baseline) and the EGAM-simulated outputs. MAE is given by

$$\text{MAE} = \frac{\sum_{i=1}^{L} \mid u_i - v_i \mid}{L} \tag{38}$$

where u is the predicted value, v is the baseline value, and L is the length of the window for comparison.

Table 7. EGAM performance comparison to increase in switching harmonics

Case	**MAE (PLECS vs EGAM)**	**% improvement over first case**
$p = 2, r = 0$	0.15474	0
$p = 2, r = 1$	0.12660	18.184
$p = 2, r = 2$	0.11698	24.399

In the first example in Figure 12a, the inverter's ac side filter capacitor's voltage waveform is shown for a snapshot in a steady state where different EGAM models are overlayed on top of the PLECS model. As the modulation signal's harmonics are increased on the p axis, EGAM's accuracy increases. Table 6 shows the MAE for different EGAM models and their improvement. As the ac side of the inverter responds more strongly with odd harmonics of the modulation signal, a significant improvement is found in model accuracy for $p = 3, r = 0$ compared to $p = 1, r = 0$ case. EGAM for $p \geq 3$ tracks the cycle average of the PLECS waveform more closely.

In the second example shown in Figure 12b, the startup transient of the inverter is shown with emphasis on the switching ripple performance. As r-axis harmonics increase, EGAM matching with PLECS simulation increases. The model for $r = 0$ tracks the cycle

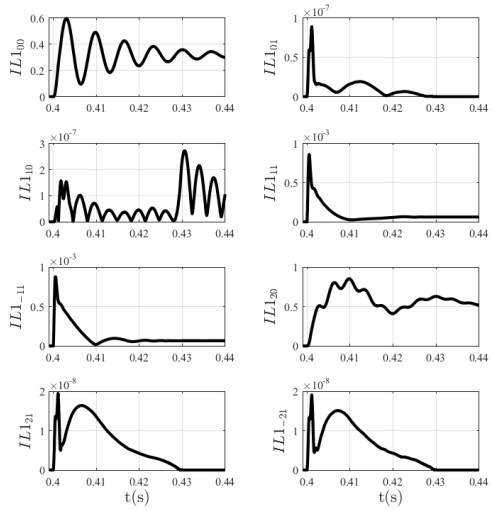

(a) DC side inductor Fourier plane plots for startup simulation

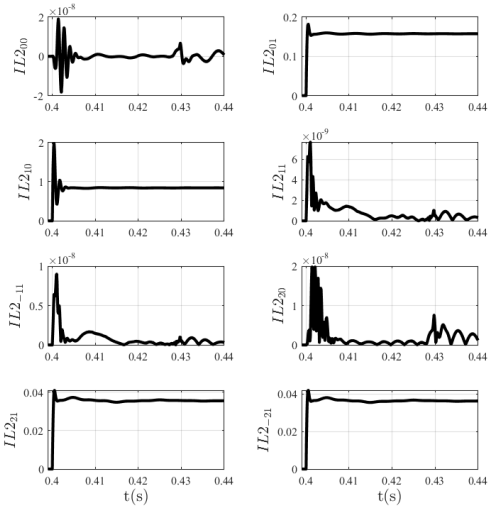

(b) AC side inductor Fourier plane plots for startup simulation

Figure 13. Frequency decomposition of state variables obtained from EGAM simulation data

average of the PLECS simulation due to harmonic truncation, whereas the more complex EGAM simulations exhibit the switching behaviors as well. MAE performance of EGAM compared to PLECS simulation for Figure 12b is shown in Table. 7

5.7. FOURIER PLANE PLOTS OF HARMONIC COMPONENTS

EGAM simulations also give insights into how each Fourier coefficient vector in the state variables performs at different frequencies. Figure 13a, and 13b show the time progression of the state variables in the frequency domain for the dc and ac side inductors, respectively. The dc side inductor states are predominantly subjected to even harmonics, so the components x_{10} have negligible values (as noted by the y-axis magnitudes). On the other hand, the AC side components have insignificant values of x_{20} while having significant values of x_{10}.

6. CONCLUSION

This article proposes a novel modeling technique to extend the capabilities of the conventional GAM by handling the DFS products using the DFI representation of signals in the frequency domain. The problem of multiplying two DFS signals is investigated using the proposed theory. Furthermore, an algorithm is proposed to resolve the resulting two-dimensional convolutions for implementation in numerical ODE solvers and is shared as a MATLAB toolbox in Appendix 1.6. To balance mathematical modeling and practicality, a single-phase inverter is used as a test example to show the validity of the proposed method, and an excellent correlation is observed between the detailed model and EGAM. In the future, EGAM can model the dynamics of more complicated systems such as an ac-ac DAB [20, 21, 22], wherein state variables are subjected to two different frequencies of excitation. Thus, the proposed technique offers a systematic way of easily incorporating many harmonic components in an averaged model to accurately capture the system dynamics at existing and evolving system harmonics. The harmonic truncation phenomenon plays an important role in model accuracy, and its selection was shown using the inverter example. It was also shown that increasing the number of harmonics in the EGAM simulations improved the matching with the detailed simulation model.

REFERENCES

[1] S. Sanders, J. Noworolski, X. Liu, and G. Verghese, "Generalized averaging method for power conversion circuits," *IEEE Transactions on Power Electronics*, vol. 6, no. 2, pp. 251–259, 1991.

[2] V. Caliskan, O. Verghese, and A. Stankovic, "Multifrequency averaging of dc/dc converters," *IEEE Transactions on Power Electronics*, vol. 14, no. 1, pp. 124–133, 1999.

[3] H. Alrajhi, "A generalized state space average model for parallel dc-to-dc converters," *Computer Systems Science and Engineering*, vol. 41, no. 2, pp. 717–734, 2022.

[4] H. Qin and J. W. Kimball, "Generalized average modeling of dual active bridge dc–dc converter," *IEEE Transactions on Power Electronics*, vol. 27, no. 4, pp. 2078–2084, 2012.

[5] M. Monika, M. Rane, S. Wagh, A. Stanković, and N. Singh, "Development of dynamic phasor based higher index model for performance enhancement of dual active bridge," *Electric Power Systems Research*, vol. 168, pp. 305–312, 2019.

[6] G. Brando, A. Del Pizzo, and S. Meo, "Model-reference adaptive control of a dual active bridge dc-dc converter for aircraft applications," in *2018 International Symposium on Power Electronics, Electrical Drives, Automation and Motion (SPEEDAM)*, 2018, pp. 502–506.

[7] M. Berger, I. Kocar, H. Fortin-Blanchette, and C. Lavertu, "Hybrid average modeling of three-phase dual active bridge converters for stability analysis," *IEEE Transactions on Power Delivery*, vol. 33, no. 4, pp. 2020–2029, 2018.

[8] Z. U. Zahid, Z. M. Dalala, C. Zheng, R. Chen, W. E. Faraci, J.-S. J. Lai, G. Lisi, and D. Anderson, "Modeling and control of series–series compensated inductive power transfer system," *IEEE Journal of Emerging and Selected Topics in Power Electronics*, vol. 3, no. 1, pp. 111–123, 2015.

[9] H. Fang, H. Xiang, S. Li, Y. Xin, J. Zhou, and Y. Wang, "Dynamic phasor modeling of mmc-hvdc systems," in *2022 IEEE 5th International Conference on Information Systems and Computer Aided Education (ICISCAE)*, 2022, pp. 988–995.

[10] O. C. Sakinci and J. Beerten, "Generalized dynamic phasor modeling of the mmc for small-signal stability analysis," *IEEE Transactions on Power Delivery*, vol. 34, no. 3, pp. 991–1000, 2019.

[11] A. Francés, R. Asensi, O. García, R. Prieto, and J. Uceda, "Modeling electronic power converters in smart dc microgrids—an overview," *IEEE Transactions on Smart Grid*, vol. 9, no. 6, pp. 6274–6287, 2018.

[12] S. K. Gurumurthy, M. Mirz, B. S. Amevor, F. Ponci, and A. Monti, "Hybrid dynamic phasor modeling approaches for accurate closed-loop simulation of power converters," *IEEE Access*, vol. 10, pp. 101 643–101 655, 2022.

[13] A. Nazari, Y. Xue, J. K. Motwani, I. Cvetkovic, D. Dong, and D. Boroyevich, "Dynamic phasor modeling of three phase voltage source inverters," in *2021 6th IEEE Workshop on the Electronic Grid (eGRID)*, 2021, pp. 1–6.

[14] U. C. Nwaneto and A. M. Knight, "Dynamic phasor-based modeling and simulation of a reduced-order single-phase inverter in voltage-controlled and current-controlled modes," in *2020 IEEE Texas Power and Energy Conference (TPEC)*, 2020, pp. 1–6.

[15] ——, "Dynamic phasor-based modeling and simulation of a single-phase diode-bridge rectifier," *IEEE Transactions on Power Electronics*, vol. 38, no. 4, pp. 4921–4936, 2023.

[16] Z. Shuai, Y. Peng, J. M. Guerrero, Y. Li, and Z. J. Shen, "Transient response analysis of inverter-based microgrids under unbalanced conditions using a dynamic phasor model," *IEEE Transactions on Industrial Electronics*, vol. 66, no. 4, pp. 2868–2879, 2019.

[17] A. Bendib, A. Kherbachi, A. Chouder, H. Ahmed, and K. Kara, "Advanced control scheme and dynamic phasor modelling of grid-tied droop-controlled inverters," *IET Renewable Power Generation*, vol. n/a, no. n/a. [Online]. Available: https://ietresearch.onlinelibrary.wiley.com/doi/abs/10.1049/rpg2.12610

[18] J. Mahdavi, A. Emaadi, M. Bellar, and M. Ehsani, "Analysis of power electronic converters using the generalized state-space averaging approach," *IEEE Transactions on Circuits and Systems I: Fundamental Theory and Applications*, vol. 44, no. 8, pp. 767–770, 1997.

[19] J. A. Mueller and J. W. Kimball, "An improved generalized average model of dc–dc dual active bridge converters," *IEEE Transactions on Power Electronics*, vol. 33, no. 11, pp. 9975–9988, 2018.

[20] K. J. Veeramraju, A. Sharma, and J. W. Kimball, "A comprehensive analysis on complex power flow mechanism in an ac-ac dual active bridge," in *2022 IEEE Power and Energy Conference at Illinois (PECI)*, 2022, pp. 1–6.

[21] A. Sharma, K. J. Veeramraju, and J. W. Kimball, "Power flow control of a single-stage ac-ac solid-state transformer for ac distribution system," in *2022 IEEE Power and Energy Conference at Illinois (PECI)*, 2022, pp. 1–6.

[22] H. Qin and J. W. Kimball, "Solid-state transformer architecture using ac–ac dual-active-bridge converter," *IEEE Transactions on Industrial Electronics*, vol. 60, no. 9, pp. 3720–3730, 2013.

[23] X. Liu, A. M. Cramer, and F. Pan, "Generalized average method for time-invariant modeling of inverters," *IEEE Transactions on Circuits and Systems I: Regular Papers*, vol. 64, no. 3, pp. 740–751, 2017.

[24] X. Liu and A. M. Cramer, "Three-phase inverter modeling using multifrequency averaging with third harmonic injection," in *2016 IEEE Energy Conversion Congress and Exposition (ECCE)*, 2016, pp. 1–6.

[25] S. Sen, P. L. Evans, and C. Mark Johnson, "Multi-frequency averaging (mfa) model of a generic electric vehicle powertrain suitable under variable frequency of averaging developed f or remote operability," *IET Electrical Systems in Transportation*, vol. 10, no. 3, pp. 268–274, 2020.

[26] S. Sen, P. L. Evans, and C. M. Johnson, "Multi-frequency averaging (mfa) model of electric-hybrid powertrain suitable for variable frequency operation applied in geographically-distributed power hardware-in-the-loop (gd-phil) simulation," in *2018 IEEE Vehicle Power and Propulsion Conference (VPPC)*, 2018, pp. 1–6.

[27] A. V. Oppenheim, A. S. Willsky, and S. H. Nawab, *Signals & Systems (2nd Ed.)*. USA: Prentice-Hall, Inc., 1996.

[28] P. Shamsi, "Extended averaging method for power supply systems with multiple switching frequencies," in *2014 IEEE Applied Power Electronics Conference and Exposition - APEC 2014*, 2014, pp. 2842–2846.

[29] X. Liu, "Improvements in inverter modeling and control," Ph.D. dissertation, University of Kentucky, 2017.

[30] K. J. Prasad Veeramraju and J. W. Kimball, "Multidimensional extensions to generalized averaged models for multi-frequency-excited dynamic systems," in *2021 IEEE 22nd Workshop on Control and Modelling of Power Electronics (COMPEL)*, 2021, pp. 1–8.

III. DYNAMIC MODEL OF AC-AC DUAL ACTIVE BRIDGE CONVERTER USING THE EXTENDED GENERALIZED AVERAGE MODELING FRAMEWORK

Kartikeya Jayadurga Prasad Veeramraju and Jonathan W. Kimball
Department of Electrical and Computer Engineering
Missouri University of Science and Technology
Rolla, MO 65401 USA
Email: kvkhh@mst.edu; kimballjw@mst.edu

ABSTRACT

The ac-ac Dual Active Bridge (DAB) converter is an advanced bidirectional two-port grid interface converter that facilitates active and reactive power flow control between two grids without the need for a dc-link capacitor. This paper presents a novel modeling approach for the ac-ac DAB converter using the Extended Generalized Average Modeling (EGAM) technique. Unlike the conventional Generalized Average Modeling (GAM) framework, the ac-ac DAB converter's dynamic state variables, including the leakage inductor current and ac grid side LC-filters, exhibit grid and switching frequency components, making the standard GAM framework unsuitable for dynamic modeling involving two distinct excitation frequencies. Furthermore, the two-dimensional GAM (2D-GAM) framework, although capable of capturing the dynamics of two frequencies and their cross-interactions, fails to handle product terms involving Double Fourier Series (DFS) states resulting from the switching terms in the ac-ac DAB converter. To address these challenges, the EGAM technique is proposed, which involves transforming the DFS product terms in the time domain into the 2D-convolution of their Discrete Fourier Images (DFI) in the frequency domain. The effectiveness of the EGAM modeling framework is demonstrated through extensive simulation and hardware experiments, and the results are compared with PLECS domain waveforms, validating the accuracy and efficacy of the proposed approach.

Keywords: Generalized Averaged Models, Multi Frequency Averaging, Dynamic Phasor Modeling, Power Electronic Converters, Inverters.

1. INTRODUCTION

Solid State Transformers (SST) are becoming prevalent as the stability and power requirements for power distribution systems increase [1]. For the distribution level, reliable and straightforward circuit topologies are desired. A comprehensive review of the design challenges of SST can be found in [1, 2, 3, 4]. SSTs of the first category [5, 6, 7, 3, 8, 9, 10] are generally simpler in construction and interface two ac grids without an intermediate dc link. A matrix converter-type topology is proposed in [7], where 54 switches are needed to realize a three-phase power flow. However, reaching a 95 – 98 % efficiency in this SST can be very challenging due to the high switch count [1]. Some other three-phase topologies employing DABs are also proposed in [8, 11, 5, 9] to reduce the switch count.

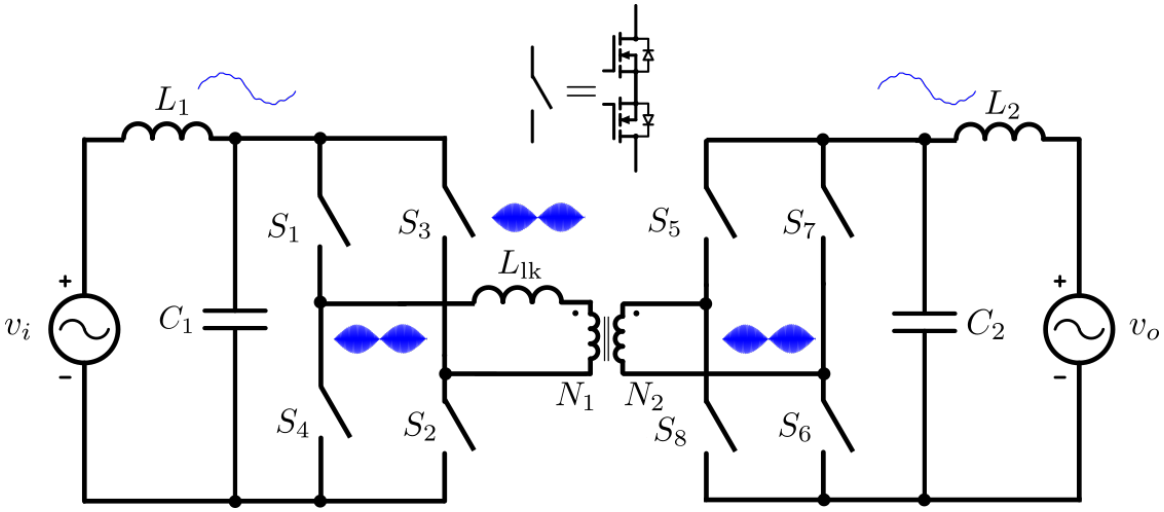

Figure 1. AC-AC DAB Schematic showing frequency components

There are other conventional SST types [12, 13, 14, 15, 16] which are classified as cascaded-type architectures and often employ an ac-dc-ac or ac-dc-dc-ac stages. In one of these categories, the isolated side sees a high-voltage ac while the dc-link sees a low-voltage dc, which is further inverted. The availability of dc-link makes these classes of SSTs versatile

and facilitates the integration of renewable resources operating at different voltage levels but it also poses challenges due to the higher number of power stages and corresponding circuit complexity [17].

An SST in a DAB configuration referred to as the ac-ac DAB in this article is shown in Figure 1 [18, 17, 19, 6]. This particular topology is an attractive alternative to the cascaded converter architecture [17, 18, 1] because of the following:

- fewer passive components
- better reliability
- smaller footprint and lower cost
- soft-switching capability
- higher efficiency
- bidirectional active and reactive power flow capability
- higher safety from galvanic isolation between grids.

Switches S_1-S_4 comprise the primary bridge and S_5-S_8 comprise secondary side bridge. Each switch is a four-quadrant switch [20] with anti-series connected solid-state switches. Two power quality conditioning LC filters comprising capacitors L_1, C_1 on the input side and L_2, C_2 on the output side are used. The High-Frequency Transformer provides the isolation and voltage boost/buck actions to interface two different voltage grids. N_1 and N_2 are the HFT primary and secondary turns, respectively. The DAB inductance L_{lk} is a critical parameter for the power transfer between both bridges.

Modeling the dynamic performance of power converters leads to interesting insights into the inner workings of the converters and aids in better understanding. Also, an accurate converters model helps design an appropriate controller for the converter. There are various methods for dynamical system modeling in power electronics: the State Space Averaging

(SSA) technique, the Generalized Average Modeling technique (GAM), the two-dimensional GAM (2D-GAM) technique, and the Extended GAM (EGAM) technique. SSA applies when Small Ripple Approximation (SRA) applies to the state variables as is the case with buck, boost, and buck-boost topologies. GAM technique, on the other hand, can model systems whose state variables violate SRA, like the dc-dc DAB converters and resonant converters. 2D-GAM is applicable where two frequencies of excitations are present like the sine pulse width modulated inverter with dynamic elements on ac side [21].

All the aforementioned dynamic modeling techniques approximate the state variables as Fourier series expansions with varying depths of complexity. For example, the SSA technique is a subset of GAM that only tracks the cycle average of state variables and therefore only captures the dc terms in Fourier series representation. GAM on the other hand also captures the fundamental harmonics of the switching functions represented as one dimensional Fourier series representation and the ripple behaviors. The popular Synchronous Reference Frame Modeling (SRFM) technique used in three-phase inverters is a subset of the GAM and disjoints from the SSA technique. SRFM considers the fundamental harmonic components of the state variables involved in the system. Finally, the 2D-GAM technique expands the GAM technique on a second dimension to capture two-frequency behaviors by modeling the state variables as Double Fourier Series (DFS) representations. Therefore 2D GAM is a superset modeling technique encompassing GAM and SSA techniques. Therefore, instead of explicitly capturing the time domain behavior of the signals, all these techniques capture the time evolution of Fourier coefficients of the state variables.

Although 2D-GAM effectively captures two-frequency dynamic phenomena, it does not include the multiplication of two DFS variables. Therefore, the authors of past works neglected these DFS product interactions and made the systems simple to circumvent the problem of DFS multiplications. The EGAM technique includes these terms and avoids

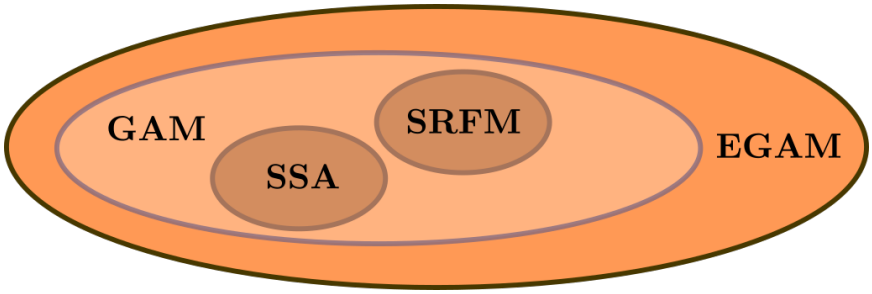

Figure 2. Various Modeling Techniques

oversimplification. The EGAM framework uses a Discrete Fourier Image (DFI) signal to capture the DFS coefficient terms and makes multiplication operations feasible. Figure 2 shows a Venn diagram of various modeling techniques.

In the past, the 2D-GAM and EGAM techniques were used to model the behaviors of single-phase and three-phase inverters [22, 21, 23, 24, 25, 26, 27]. However, the applicability of the EGAM technique for modeling an ac-ac DAB is yet to be explored. The ac-ac DAB also has multi-frequency interactions as shown in Figure 1, which lead to DFS modeling requirements in the state variables. The inductors L_1 and L_2 and capacitors C_1 and C_2 predominantly experience grid level harmonics while L_{lk} experiences both grid level and switching level harmonics as shown by the enveloped sinusoidal waveforms in Figure 1. This article explores the EGAM technique implementation on the ac-ac DAB and compares the results' efficacy with simulation and hardware results. Also, the various insights on the results will be interpreted. This article is organized as follows: a review of the GAM, 2D-GAM, and EGAM is first presented in Section 2. Equipped with the background, the article then models the ac-ac DAB converter in 3 and formulates the EGAM model of the converter. The simulation results are compared with PLECS simulations in Section 4. A hardware converter is designed, and the EGAM results are compared with the hardware results in Section 5.

Table 1. EGAM operations set

Operation	Time Domain	Frequency Domain
Scalar Product	$ax(t)$	$a\mathbf{x}$
Summation	$x(t) + y(t)$	$\mathbf{x} + \mathbf{y}$
Differentiation	$\frac{dx(t)}{dt}$	$\left(\frac{d\mathbf{x}}{dt} + \mathbf{T}\mathbf{x}\right)$
Multiplication	$x(t)y(t)$	$\mathbf{x}\circledast \circledast\mathbf{y}$

2. REVIEW OF GAM

In conventional GAM, the time-dependent state variables are transformed to the Fourier coefficients written as Single Fourier Series (SFS) expansions; that is, a periodic signal $x(t)$ in the time domain can be written as

$$x(t) = \sum_{k=-\infty}^{+\infty} x_k e^{jk\omega_0 t} \tag{1}$$

$$\mathbf{C}(t) = \begin{bmatrix} 1 & \cos(\bar{\omega}t) & \sin(\bar{\omega}t) & \cdots & \cos(n\bar{\omega}t) & \sin(n\bar{\omega}t) \end{bmatrix} \tag{2}$$

$$x(t) = \mathbf{C}(t) \cdot \mathbf{x}_k^{\mathsf{T}} \tag{3}$$

where $\mathbf{x}_k$ is the vector of Fourier coefficients

$$\mathbf{x}_k = \begin{bmatrix} x_0 & x_{1c} & x_{1s} & \cdots & x_{nc} & x_{ns} \end{bmatrix} \tag{4}$$

With these base relationships, the framework can be extended for other operators [28, 29, 21] given by

$$\frac{d}{dt}\langle x\rangle_k(t) = \left\langle \frac{d}{dt}x \right\rangle_k (t) - jk\omega_0\langle x\rangle_k(t) \tag{5}$$

$$\langle xy\rangle_k = \sum_{i=-\infty}^{\infty} \langle x\rangle_{k-i}\langle y\rangle_i \tag{6}$$

the operator $\langle\bullet\rangle_k$ represents the k^{th} harmonic Fourier coefficient of a time domain signal and (6) is a discrete 1D convolution [30].

If the system of interest has two distinct excitation frequencies, namely ω_1, ω_2, the state variable $x(t)$ in the time domain is represented using DFS given by

$$x(t) = \sum_{p\in\mathbb{Z},r\in\mathbb{W}} \mathrm{x}_{p,r} e^{i(p\omega_1 t + r\omega_2 t)} \tag{7}$$

then it can be converted to the vector containing the Fourier coefficients for a finite number of harmonics as

$$\mathbf{x} = \begin{bmatrix} \mathrm{x}_{0,0} & \mathrm{x}_{1,0c} & \mathrm{x}_{1,0s} & \cdots & \mathrm{x}_{0,1c} & \mathrm{x}_{0,1s} & \cdots & \mathrm{x}_{p,rc} & \mathrm{x}_{p,rs} \end{bmatrix} \tag{8}$$

where, $\mathrm{x}_{p,0c}$, $\mathrm{x}_{p,0s}$ belong to the Fourier coefficients of the harmonics of ω_1; $\mathrm{x}_{0,rc}$, $\mathrm{x}_{0,rs}$ belong to coefficients of the harmonics of ω_2, and $\mathrm{x}_{p,rc}$, $\mathrm{x}_{p,rs}$ belong to coefficients of the harmonics of $p\omega_1 + r\omega_2$ components. The subscripts c and s correspond to the cos and sin terms of the DFS expansion in rectangular form.

In order to extend the GAM framework to 2D-GAM, (5) is rewritten as

$$\frac{dx(t)}{dt} = \mathbf{C}(t)\left(\frac{d\mathbf{x}}{dt} + \mathbf{T}\mathbf{x}\right) \tag{9}$$

where the DFS coefficients of the expansion are stored in the state variable $\mathbf{x}$ (8) and the matrix $\mathbf{T}$ stores the frequency information at the state variable $\mathrm{x}_{p,r}$. Therefore, $\mathbf{T}$ is the matrix version of the second term of GAM (5) given by

$$\mathbf{T}_{(2k,2k+1)} = (\mathbf{m}_{k+1}\omega_1 + \mathbf{n}_{k+1}\omega_2) \tag{10}$$

$$\mathbf{T}_{(2k+1,2k)} = -(\mathbf{m}_{k+1}\omega_1 + \mathbf{n}_{k+1}\omega_2) \tag{11}$$

where $k \in \mathbb{N}^O$, indexes the vectors $\mathbf{m} \in \mathbb{Z}^{O+1}$,and $\mathbf{n} \in \mathbb{W}^{O+1}$. Dimensionally, $\mathbf{T}$ is a $(2O+1)\times(2O+1)$ sparse matrix [23]. O is the total number of distinct frequencies and harmonic combinations considered, excluding the dc term and $k \in \{1, 2, \cdots O\}$. Vectors $\mathbf{m}$

and **n** have an order of one more than the distinct frequencies (O) to account for the dc term, which is always the first entry from an indexing viewpoint. With these base equations, a first-order differential equation of the form

$$\frac{dx(t)}{dt} = ax(t) + by(t) \tag{12}$$

can be rewritten in the Fourier coefficients and using (3)

$$\left\langle \frac{dx(t)}{dt} \right\rangle = a\langle x(t)\rangle + b\langle y(t)\rangle \tag{13}$$

$$\frac{d\mathbf{x}}{dt} = (a\mathbf{I} - \mathbf{T})\mathbf{x} + b\mathbf{y} \tag{14}$$

where **x**, **y** are Fourier coefficient vectors at the same frequencies. Applying the same procedure on a more complicated base first-order ordinary differential equation

$$\frac{dx(t)}{dt} = ax(t) + bx(t)y(t) \tag{15}$$

$$\frac{d\mathbf{x}}{dt} = (a\mathbf{I} - \mathbf{T})\mathbf{x} + b(\mathbf{x} * \mathbf{y}[\ell]) \tag{16}$$

Eq. (16) can then be expanded for the desired number of harmonics (by writing for each harmonic order, $\ell \in (1, 2, \cdots, O)$) to finally give

$$\frac{d}{dt}\begin{bmatrix} x_0 \\ x_{1c} \\ x_{1s} \\ \vdots \\ x_{lc} \\ x_{ls} \end{bmatrix} = \begin{bmatrix} a & 0 & 0 & 0 & \cdots & 0 \\ 0 & a & -\omega_1 & 0 & \cdots & 0 \\ 0 & \omega_1 & a & 0 & \cdots & 0 \\ \vdots & \vdots & \vdots & \ddots & \vdots & \vdots \\ 0 & 0 & 0 & 0 & a & -\omega_l \\ 0 & 0 & 0 & 0 & \omega_l & a \end{bmatrix} \begin{bmatrix} x_0 \\ x_{1c} \\ x_{1s} \\ \vdots \\ x_{lc} \\ x_{ls} \end{bmatrix} + b \begin{bmatrix} \sum_{u=-\infty}^{\infty} x[u]y[-u] \\ \Re\left\{\sum_{u=-\infty}^{\infty} x[u]y[1-u]\right\} \\ \Im\left\{\sum_{u=-\infty}^{\infty} x[u]y[1-u]\right\} \\ \vdots \\ \Re\left\{\sum_{u=-\infty}^{\infty} x[u]y[l-u]\right\} \\ \Im\left\{\sum_{u=-\infty}^{\infty} x[u]y[l-u]\right\} \end{bmatrix} \tag{17}$$

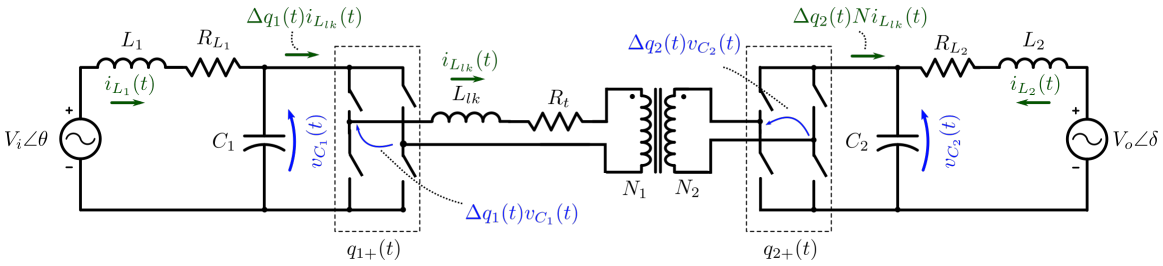

Figure 3. ACAC DAB Schematic for EGAM formulation

In (15), the product of two SFS terms, $x(t)y(t)$, translated to 1D discrete convolution on the frequency plane for the Fourier coefficient vectors **x**, **y** [28, 31, 29, 24, 25]. The translation from the time domain to the frequency domain for the multiplication of two terms expressed as DFS is performed using the 2D convolution of Discrete Fourier Image Signals [26]. The 2D-GAM [23], along with the addition of the DFI convolution algorithm, forms the Extended Generalized Average Modeling (EGAM) framework.

Referring back to (15), and assuming $x(t)$ and $y(t)$ to be DFS expansions instead of SFS, (16) can be expanded into the second dimension by

$$\frac{d\mathbf{x}}{dt} = (a\mathbf{I} - \mathbf{T})\mathbf{x} + b(\mathbf{x} \circledast \circledast \mathbf{y}) \tag{18}$$

where $\bullet\circledast\ \circledast\bullet$ operator signifies the 2D DFI convolution algorithm [26] operation. This completes the EGAM formulation that is capable of handling DFS products. A complete set of the time domain to EGAM translations is shown in Table 1 for clarity.

3. DYNAMIC MODEL OF AC-AC DAB

3.1. SWITCHING FUNCTION FOURIER SERIES REPRESENTATION FOR PHASE SHIFT MODULATION

Before proceeding with the dynamic equations of the ac-ac DAB converter, the switching function $q_+(t)$ for the phase shift modulated PWM must be realized. The switching function for a switching angular frequency of $\omega_s = 2\pi f_s$ and phase shift angle ϕ rad is given

by

$$q_+(t) = \begin{cases} 1, & -\pi < \omega_s t < -\pi + \phi \\ 0, & -\pi + \phi < \omega_s t < \phi \\ 1, & \phi < \omega_s t < \pi \end{cases} \tag{19}$$

The periodic signal $q_+(t)$ can be expanded as a Fourier series representation as

$$q_+(t) = a_0 + \sum_{n=1}^{\infty} a_n \cos(nt) + \sum_{n=1}^{\infty} b_n \sin(nt) \tag{20}$$

where a_0, a_n, b_n are the Fourier coefficients given by

$$\begin{aligned} a_0 &= \frac{1}{2} \\ a_n(\phi) &= -\frac{\sin(n\pi - n\phi)}{n\pi} - \frac{\sin(n\phi)}{n\pi} \\ b_n(\phi) &= -\frac{\cos(n\pi - n\phi)}{n\pi} + \frac{\cos(n\phi)}{n\pi} \end{aligned} \tag{21}$$

3.2. TIME DOMAIN DYNAMIC EQUATIONS

The schematic of the ac-ac DAB is shown in Figure 3. The input voltage $v_i(t)$ and output voltage $v_o(t)$ are grid voltages with a peak value of V_i and V_o, respectively. The input and output voltages have phase angles θ and δ, respectively. An LC filter comprising the inductor L_1 and capacitor C_1 is used on the primary side. The secondary side is comprised of another LC filter with the inductor L_2 and capacitor C_2. Both the inductors have internal resistances R_{L_1} and R_{L_2}. A transformer links the primary side H-bridge with the secondary side H-bridge. The transformer has a leakage inductance L_{lk} and a winding resistance R_t. The transformer has a turns ratio given by $N = N_1/N_2$ where N_1 and N_2 are the transformer's primary and secondary turns count, respectively.

Five dynamic equations can be written as there are five dynamical elements in the system. By writing the node and mesh equations for the circuit, the dynamic equations turn out to be

$$\frac{di_{L_1}(t)}{dt} = \frac{1}{L_1}v_i(t) - \frac{R_L}{L_1}i_{L_1}(t) - \frac{1}{L_1}v_{C_1}(t) \tag{22}$$

$$\frac{dv_{C_1}(t)}{dt} = \frac{1}{C_1}i_{L_1}(t) - \frac{1}{C_1}i_{L_{lk}}(t)\Delta q_1(t) \tag{23}$$

$$\frac{di_{L_{lk}}(t)}{dt} = \frac{v_{C_1}(t)}{L_{lk}}\Delta q_1(t) - \frac{Nv_{C_2}(t)}{L_{lk}}\Delta q_2(t) - \frac{R_t}{L_{lk}}i_{lk}(t) \tag{24}$$

$$\frac{di_{L_2}(t)}{dt} = \frac{1}{L_2}v_o(t) - \frac{R_{L_2}}{L_2}i_{L_2}(t) - \frac{1}{L_2}v_{C_2}(t) \tag{25}$$

$$\frac{dv_{C_2}(t)}{dt} = \frac{i_{L_2}(t)}{C_2} + \frac{Ni_{lk}(t)}{C_2}\Delta q_2(t) \tag{26}$$

where $\Delta q_1(t)$ and $\Delta q_2(t)$ are the primary and secondary side H-Bridge actions respectively. The function $\Delta q_x(t)$ is expanded as $q_{x+}(t) - q_{x-}(t)$ for $x \in \{1, 2\}$. The complement of $q_{x+}(t)$ is denoted by $q_{x-}(t)$. The H-bridge is modeled as a transformer with a turns ratio of $\Delta q_x(t)$, and the currents and voltages across the H-bridge are related by energy equivalence.

3.3. EGAM DYNAMIC EQUATIONS

For transforming the time domain differential equations to the frequency domain, the EGAM operators in Table 1 are used. The terms $q_{x+}(t) - q_{x-}(t)$ transform to $\mathbf{q}_{x+} - \mathbf{q}_{x-}$ which can be further simplified to $2\mathbf{q}_{x+} - \Upsilon$, where Υ is a sparse vector given by

$$\Upsilon = \begin{bmatrix} 1 & 0 & 0 & \cdots & 0 \end{bmatrix} \tag{27}$$

For $\mathbf{q}_{1+}$, the relationships in (21) with $\phi = 0$ is used, as $\mathbf{q}_{1+}$ is the primary side switching function, which serves as the zero reference. For secondary side, $\mathbf{q}_{2+}$ is written for $\phi \in \{-\pi/2, +\pi/2\}$. The $\mathbf{q}_{x+}$ switching vectors are given by

$$\mathbf{q}_{x+} = \begin{bmatrix} a_0 & a_1(\phi) & b_1(\phi) & \cdots & a_n(\phi) & b_n(\phi) \end{bmatrix} \tag{28}$$

Using these transformations, the frequency domain dynamic equations are given by

$$\frac{d\mathbf{i}_{L_1}}{dt} = -\left(\frac{R_{L_1}}{L_1} + \mathbf{T}\right)\mathbf{i}_{L_1} + \frac{1}{L_1}\Gamma - \frac{1}{L_1}\mathbf{v}_{C_1} \tag{29}$$

$$\frac{d\mathbf{v}_{C_1}}{dt} = -\mathbf{T}\mathbf{v}_{C_1} + \frac{1}{C_1}\mathbf{i}_{L_1} - \frac{1}{C_1}(2\mathbf{i}_{L_{lk}} \circledast \circledast \mathbf{q}_1 - \mathbf{i}_{L_{lk}} \circledast \circledast \Upsilon) \tag{30}$$

$$\begin{aligned} \frac{d\mathbf{i}_{L_{lk}}}{dt} = &-\left(\frac{R_t}{L_{lk}} + \mathbf{T}\right)\mathbf{i}_{lk} + \frac{1}{L_{lk}}(2\mathbf{v}_{C_1} \circledast \circledast \mathbf{q}_1 \\ &- \mathbf{v}_{C_1} \circledast \circledast \Upsilon) - \frac{N_1}{N_2}\frac{1}{L_{lk}}(2\mathbf{v}_{C_2} \circledast \circledast \mathbf{q}_2 - \mathbf{v}_{C_2} \circledast \circledast \Upsilon) \end{aligned} \tag{31}$$

$$\frac{d\mathbf{i}_{L_2}}{dt} = -\left(\mathbf{T} + \frac{R_{L_2}}{L_2}\right)\mathbf{i}_{L_2} + \frac{1}{L_2}\Lambda - \frac{1}{L_2}\mathbf{v}_{C_2} \tag{32}$$

$$\frac{d\mathbf{v}_{C_2}}{dt} = -\mathbf{T}\mathbf{v}_{C_2} + \frac{\mathbf{i}_{L_2}}{C_2} + \frac{1}{C_2}(2\mathbf{i}_{lk} \circledast \circledast \mathbf{q}_{2+} - \mathbf{i}_{lk} \circledast \circledast \Upsilon) \tag{33}$$

where Γ and Λ are referred to as excitation vectors, which carry the information of the grid voltage excitation. These vectors are sparse, with values populated only at frequency indices where excitations are present. The excitation vectors for an input peak voltage V_i and input phase angle θ and output peak voltage V_o with phase angle δ are given by

$$\begin{aligned} \Gamma &= \begin{bmatrix} 0 & \cdots & V_i \sin(\theta) & V_i \cos(\theta) & \cdots & 0 \end{bmatrix} \\ \Lambda &= \begin{bmatrix} 0 & \cdots & V_o \sin(\delta) & V_o \cos(\delta) & \cdots & 0 \end{bmatrix} \end{aligned} \tag{34}$$

Table 2. ACAC DAB Experimental Parameters

Parameter	Value
f_{sw}	30 kHz
f_g	60 Hz
$L_1 = L_2$	270 µH
$R_{L_1} = R_{L_2}$	100 mΩ
$C_1 = C_2$	40 µF
L_{lk}	10 µF
R_t	10 mΩ
$N_1 = N_2$	1

4. SIMULATION VERIFICATION

In this section, a PLECS model is created to act as a baseline to compare the performance of various EGAM models of the ac-ac DAB. The EGAM model developed in the earlier section is used, and simulations are run for the same conditions in the PLECS and EGAM simulations. The parameters used in simulation studies are given in Table 2.

The DFI convolution algorithm is developed using the EGAM toolbox [32] and is used to simulate the ac-ac DAB converter. A startup sequence is first simulated for a ϕ value of 25° is applied between the H-bridges for a pre-excited system with an RMS voltage of 30 V for v_i and v_o.

Initially, the simulation results for $p = 1, r = 1$ are performed. Figures 4a show v_{C_1} voltages for the startup sequence for the aforementioned harmonic components. The current $i_{L_1}(t)$ is shown in Figures 4b. Although the capacitor voltage shows a good match between PLECS and EGAM simulations, slight mismatches can be seen in the zoomed versions of the same plots shown below the main plots. The inductor currents also show appreciable congruence between PLECS and EGAM simulations. As power flows from the primary to the secondary side due to a positive phase shift, the currents in inductors are anti-phase. However, the steady-state amplitude of the inductor currents for EGAM results is slightly less than their PLECS counterparts. This mismatch in current is associated with the harmonics considered in the EGAM simulation. As the fundamental switching harmonic is the only

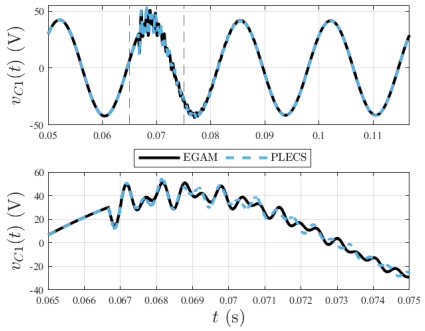

(a) C_1 voltage for startup sequence, $p = 1, r = 1$.

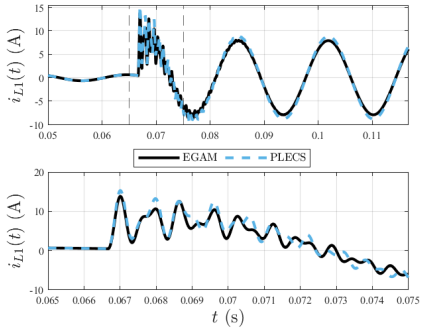

(b) L_1 current for startup sequence, $p = 1, r = 1$.

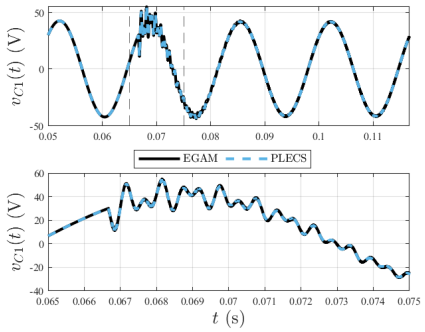

(c) C_1 voltage for startup sequence, $p = 1, r = 3$.

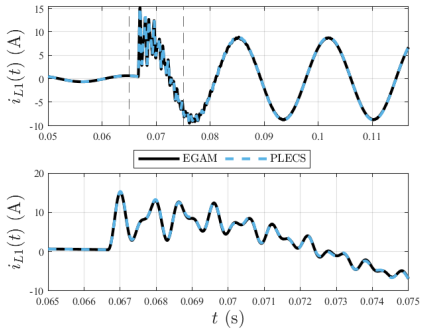

(d) L_1 current for startup sequence, $p = 1, r = 3$.

Figure 4. Grid side filter dynamics comparison for startup sequence of ac-ac DAB converter

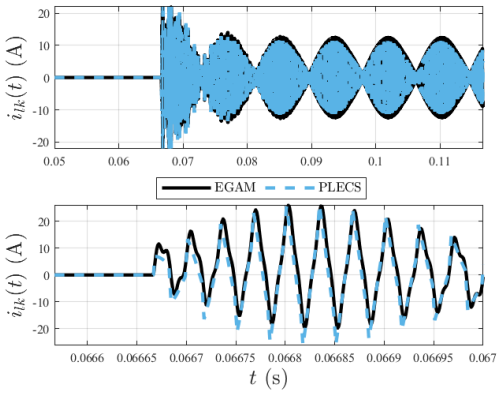

(a) Leakage inductor current startup performance for $p = 1, r = 3$ EGAM simulation overlayed on PLECS simulation

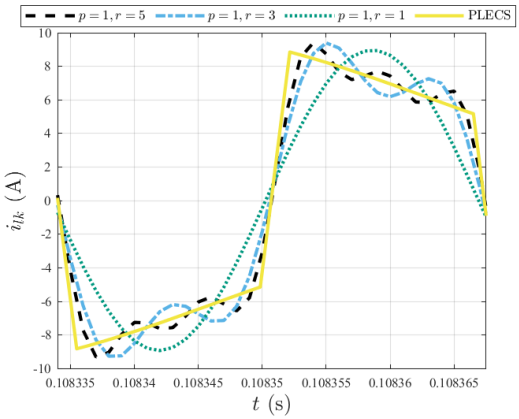

(b) Leakage inductor current steady state performance for EGAM simulation overlayed on PLECS simulation for various orders of harmonic truncation

Figure 5. Leakage inductor Current waveforms

component considered for simulation, the power transfer at the fundamental harmonic is only shown in the filter inductors at the grid level. Therefore, higher-order harmonics must be considered to improve model matching.

In order to achieve higher matching accuracy in the EGAM and PLECS results, simulations are performed for $p = 1, r = 3$ model so that the third harmonic switching actions are also considered. Therefore, the harmonic truncation [26] boundary expands until the third harmonic, leading to better features in the state variables. The results in Figure 4c show better matching characteristics after startup in the capacitor state. Figure 4d on the other hand, show better model accuracy in transient and steady-state behaviors. The third harmonic power transfer at the switching frequency improves current matching in the filter inductor currents.

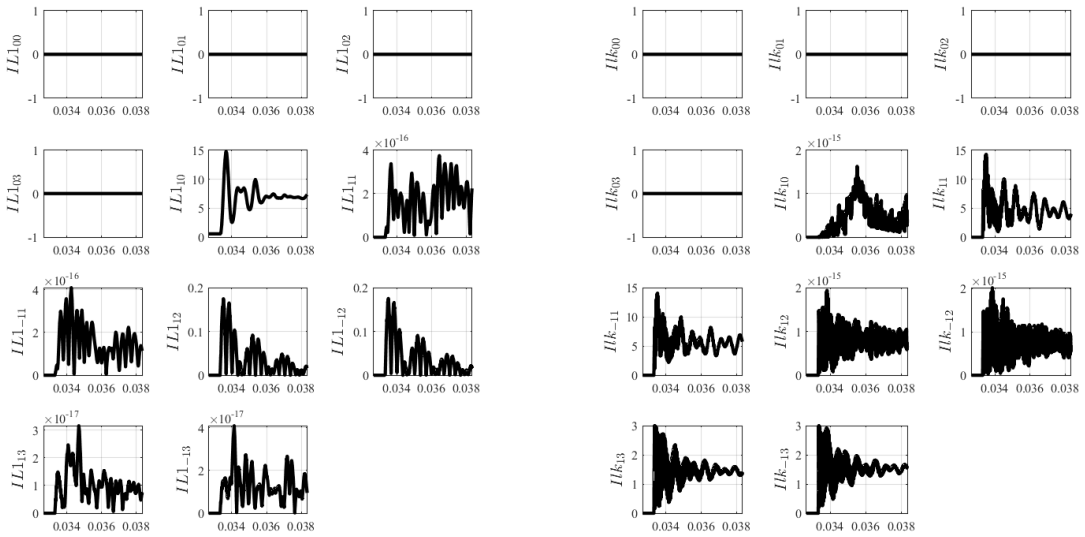

(a) Harmonic components of $\mathbf{i}_{L_1}$ (b) Harmonic components in $\mathbf{i}_{lk}$

Figure 6. Harmonic decomposition of state variables

The leakage inductor current waveform for PLECS and EGAM simulations is shown in Figure 5a. The waveforms show an excellent match with the PLECS simulation and thereby prove the efficacy of the EGAM framework for modeling multi-frequency excitations.

Additionally, Figure 5b shows the performance of EGAM for various harmonic truncation boundaries enforced inside the EGAM model. As the number of switching (r axis) harmonics increases, the EGAM performance approaches closer to the PLECS benchmark waveform.

To quantify the improvements of EGAM models with various levels of harmonic depths, *Mean Absolute Error* (MAE) is computed between PLECS-simulated (baseline) and the EGAM-simulated outputs. MAE is given by

$$\text{MAE} = \frac{\sum_{i=1}^{L} \mid u_i - v_i \mid}{L} \tag{35}$$

where u is the predicted value, v is the baseline value, and L is the length of the window for comparison. The comparisons are made between the EGAM model and the PLECS model and the MAE is calculated.

Table 3. EGAM performance improvement to increase in switching harmonics

Case	MAE (PLECS vs EGAM)	% improvement over first case
$p = 1, r = 1$	1.1	0
$p = 1, r = 3$	0.681	38.12
$p = 1, r = 5$	0.411	62.68

4.1. FREQUENCY PLANE PLOTS

The vectors in the frequency domain time progression matrix $\mathbf{x}$ are transformed into the time domain using the frequency to time domain transformation (3). To understand the harmonic nature of the state variables, each component of $\mathbf{x}$ is plotted over time. As the harmonic components other than the dc term have both the sine and the cosine coefficients, their magnitude is computed to get the behavior of the state variable at each frequency of interest.

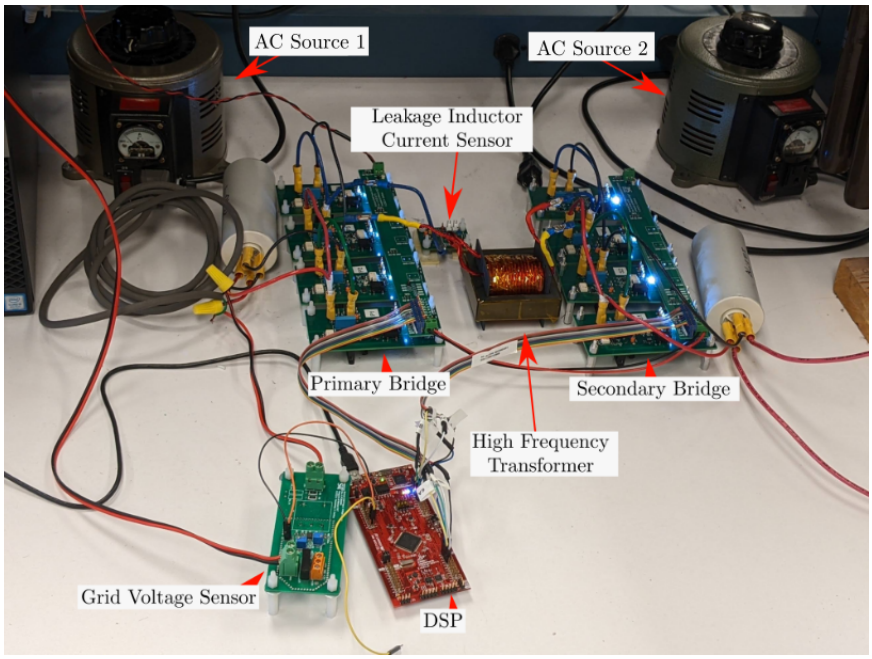

Figure 7. ACAC DAB Hardware Setup

The ac-ac DAB's state variables are plotted against time to understand the harmonic behaviors of the state variables. The results for inductor L_1 current in frequency plane $\mathbf{i}_{L_1}$ are shown in Figure 6a. The simulation for one grid harmonic and three switching harmonics is performed. The first number subscript on the y-axis label on each plot indicates the grid frequency harmonic while the second index indicates the switching frequency harmonics. The EGAM plots indicate no activity in the dc and pure switching frequency harmonics. This is associated with the absence of excitation voltages in the switching frequency indices in the excitation vectors (34). The grid frequency component ($IL1_{10}$) is the most significant harmonic in the plots. Additionally, Figure 6b plots the current characteristics at different harmonic indices for the leakage inductance current waveform. Like the grid side inductor, the leakage inductor harmonic waveforms show no activity at the dc component. However, it is interesting to note that there are no switching frequency components present in $i_{lk}(t)$. This is associated with the convolution operations and the emergence of new frequency components. This explains the significant activity in the Ilk_{11},

Ilk_{-11}, Ilk_{13} and Ilk_{-13} components where the new behaviors are seen. The $i_{lk}(t)$ waveform is an amplitude-modulated waveform where the switching frequency component is enveloped by the grid frequency leading to the $f_g \pm f_s$ components having the dominant behavior.

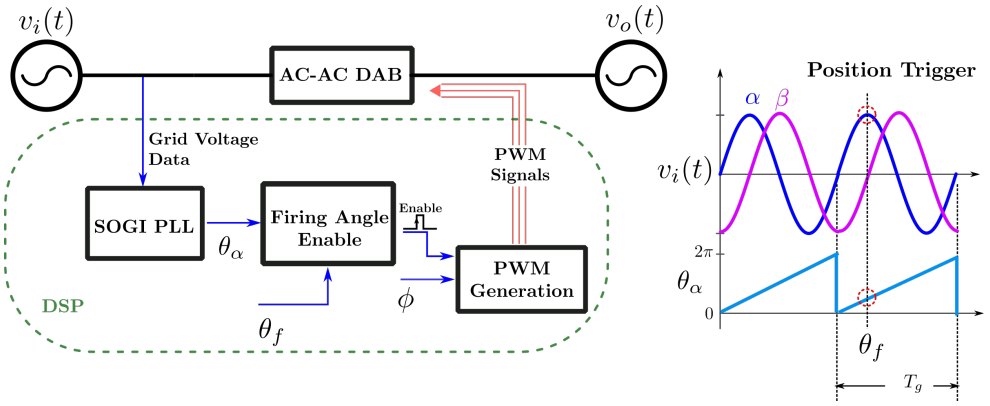

Figure 8. ACAC DAB Hardware Implementation in DSP

5. HARDWARE IMPLEMENTATION

In this section, a hardware model is built and tests similar to those done in Section 4 will be repeated to understand the correctness of the models. For this purpose, an ac-ac DAB prototype is designed as shown in Figure 7 with the specifications in Table. 2. To synchronize the trigger of the hardware model at the same time as that of the EGAM and PLECS models, a SOGI PLL [33] based positional trigger is implemented in a TMS320F28377S Digital Signal Processor (DSP) as shown in Figure 8. The SOGI PLL synchronizes with the grid frequency to get the phase information θ_α. If the position trigger's firing angle θ_f is desired, the θ_α and its match with θ_f is used to set the enable signal. The enable signal is then directed to the DSP's Pulse Width Modulation (PWM) module. The PWM module is configured to perform the phase shift modulation for the DAB stage switches for a preset value of ϕ.

A test is performed with input voltages of 26 V_{RMS} on both sides of the DAB are used. Two variable auto transformers serve as the ac sources; ac-source-1 and ac source-2. A ϕ of 21.5° is enforced on the DAB. The voltages are converted to peak values and enforced

on the excitation vectors (34) with $\theta = \delta = 90°$. The PLECS and EGAM models are run subsequently. The hardware model on the other hand is started at a θ_f of 90°. The acquired results are plotted in Figures 9a-9b.

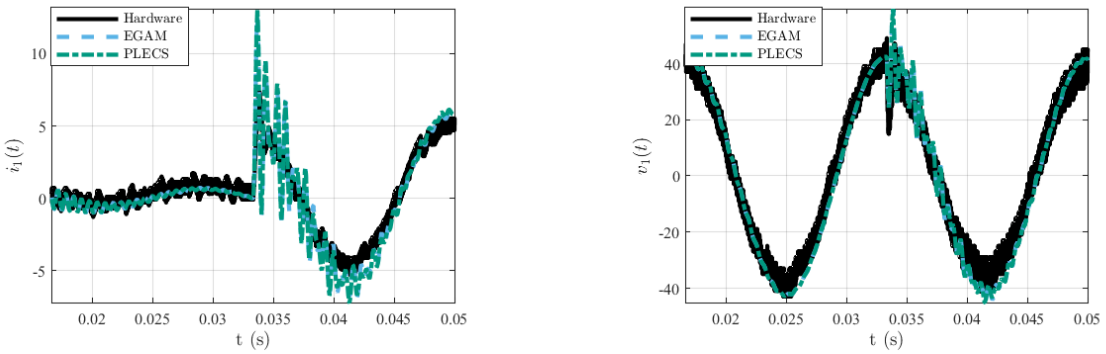

(a) Inductor L_1 current

(b) Capacitor C_1 voltage

Figure 9. EGAM, PLECS, and hardware comparison results for modulation step transient test

6. CONCLUSION

This paper uses the EGAM modeling framework to model the dynamics of the ac-ac DAB converter. After a brief review of the existing GAM modeling techniques and the EGAM technique, this article uses the EGAM technique to form the dynamic model of the ac-ac DAB. After this, the simulation tests are performed, and the PLECS and EGAM models are overlayed on top of each other. Higher matches with the PLECS waveforms are observed by adding more switching frequency harmonics in the EGAM model leading to progressively lower MAE values signifying excellent accuracies. The frequency plane magnitude vs. time graph shows the harmonics present at all excitation frequencies and new frequencies in the region of interest. The leakage inductor current is an amplitude-modulated waveform enveloped by the grid frequencies, showing negligible grid frequency and dominant sideband components. Finally, the hardware model of the ac-ac DAB converter is constructed, and

the state variables are plotted against the EGAM. The model matching is observed, thereby validating the correctness of the EGAM framework and its ability to capture two frequency dynamics.

REFERENCES

[1] X. She, A. Q. Huang, and R. Burgos, "Review of solid-state transformer technologies and their application in power distribution systems," *IEEE Journal of Emerging and Selected Topics in Power Electronics*, vol. 1, no. 3, pp. 186–198, 2013.

[2] F. Bignucolo, M. Bertoluzzo, and C. Fontana, "Applications of the solid state transformer concept in the electrical power system," in *2015 AEIT International Annual Conference (AEIT)*, 2015, pp. 1–6.

[3] Q. Zhu, L. Wang, D. Chen, L. Zhang, and A. Q. Huang, "Design and implementation of a 7.2kv single stage ac-ac solid state transformer based on current source series resonant converter and 15 kv sic mosfet," in *2017 IEEE Energy Conversion Congress and Exposition (ECCE)*, 2017, pp. 1288–1295.

[4] F. Ruiz, M. A. Perez, J. R. Espinosa, T. Gajowik, S. Stynski, and M. Malinowski, "Surveying solid-state transformer structures and controls: Providing highly efficient and controllable power flow in distribution grids," *IEEE Industrial Electronics Magazine*, vol. 14, no. 1, pp. 56–70, 2020.

[5] H. Chen and D. Divan, "Soft-switching solid-state transformer (s4t)," *IEEE Transactions on Power Electronics*, vol. 33, no. 4, pp. 2933–2947, 2018.

[6] R. Rahmoun and M. Patt, "High efficiency single-phase dual-active-bridge ac/ac converter," in *2019 21st European Conference on Power Electronics and Applications (EPE '19 ECCE Europe)*, 2019, pp. P.1–P.10.

[7] K. Mohapatra and N. Mohan, "Matrix converter fed open-ended power electronic transformer for power system application," in *2008 IEEE Power and Energy Society General Meeting - Conversion and Delivery of Electrical Energy in the 21st Century*, 2008, pp. 1–6.

[8] H. Keyhani, H. A. Toliyat, M. Harfman-Todorovic, R. Lai, and R. Datta, "An isolated resonant ac-link three-phase ac–ac converter using a single hf transformer," *IEEE Transactions on Industrial Electronics*, vol. 61, no. 10, pp. 5174–5183, 2014.

[9] K. Basu, A. Shahani, A. K. Sahoo, and N. Mohan, "A single-stage solid-state transformer for pwm ac drive with source-based commutation of leakage energy," *IEEE Transactions on Power Electronics*, vol. 30, no. 3, pp. 1734–1746, 2015.

[10] A. Sharma, K. J. P. Veeramraju, and J. W. Kimball, "Power flow control of a single-stage ac-ac solid-state transformer for ac distribution system," in *2022 IEEE Power and Energy Conference at Illinois (PECI)* [Accepted], 2022.

[11] A. Prasai, H. Chen, R. Moghe, Z. Wolanski, K. Chintakrinda, A. Zhou, J. C. Llambes, and D. Divan, "Dyna-c: Experimental results for a 50 kva 3-phase to 3-phase solid state transformer," in *2014 IEEE Applied Power Electronics Conference and Exposition - APEC 2014*, 2014, pp. 2271–2277.

[12] J. Ai-juan, L. Hang-tian, and L. Shao-long, "A new matrix type three-phase four-wire power electronic transformer," in *2006 37th IEEE Power Electronics Specialists Conference*, 2006, pp. 1–6.

[13] M. Sabahi, A. Y. Goharrizi, S. H. Hosseini, M. B. B. Sharifian, and G. B. Gharehpetian, "Flexible power electronic transformer," *IEEE Transactions on Power Electronics*, vol. 25, no. 8, pp. 2159–2169, 2010.

[14] E. Ronan, S. Sudhoff, S. Glover, and D. Galloway, "A power electronic-based distribution transformer," *IEEE Transactions on Power Delivery*, vol. 17, no. 2, pp. 537–543, 2002.

[15] S. Bhattacharya, T. Zhao, G. Wang, S. Dutta, S. Baek, Y. Du, B. Parkhideh, X. Zhou, and A. Q. Huang, "Design and development of generation-i silicon based solid state transformer," in *2010 Twenty-Fifth Annual IEEE Applied Power Electronics Conference and Exposition (APEC)*, 2010, pp. 1666–1673.

[16] D. Gonzalez-Agudelo, A. Escobar-Mejía, and H. Ramirez-Murrillo, "Dynamic model of a dual active bridge suitable for solid state transformers," in *2016 13th International Conference on Power Electronics (CIEP)*, 2016, pp. 350–355.

[17] H. Qin and J. W. Kimball, "Solid-state transformer architecture using ac–ac dual-active-bridge converter," *IEEE Transactions on Industrial Electronics*, vol. 60, no. 9, pp. 3720–3730, 2013.

[18] ——, "Ac-ac dual active bridge converter for solid state transformer," in *2009 IEEE Energy Conversion Congress and Exposition*, 2009, pp. 3039–3044.

[19] G. G. Facchinello, L. L. Brighenti, S. L. Brockveld, D. C. Martins, and W. M. Dos Santos, "Closed-loop operation and control strategy for the dual active half bridge ac-ac converter," in *2017 IEEE 8th International Symposium on Power Electronics for Distributed Generation Systems (PEDG)*, 2017, pp. 1–7.

[20] G. Venkataramanan and N. Kogalur, "A hybrid 4-quadrant switch for ac power conversion," in *2019 IEEE Energy Conversion Congress and Exposition (ECCE)*, 2019, pp. 5487–5493.

[21] X. Liu and A. M. Cramer, "Three-phase inverter modeling using multifrequency averaging with third harmonic injection," in *2016 IEEE Energy Conversion Congress and Exposition (ECCE)*, 2016, pp. 1–6.

[22] X. Liu, "Improvements in inverter modeling and control," Ph.D. dissertation, University of Kentucky, 2017.

[23] X. Liu, A. M. Cramer, and F. Pan, "Generalized average method for time-invariant modeling of inverters," *IEEE Transactions on Circuits and Systems I: Regular Papers*, vol. 64, no. 3, pp. 740–751, 2017.

[24] S. Sen, P. L. Evans, and C. M. Johnson, "Multi-frequency averaging (mfa) model of electric-hybrid powertrain suitable for variable frequency operation applied in geographically-distributed power hardware-in-the-loop (gd-phil) simulation," in *2018 IEEE Vehicle Power and Propulsion Conference (VPPC)*, 2018, pp. 1–6.

[25] S. Sen, P. L. Evans, and C. Mark Johnson, "Multi-frequency averaging (mfa) model of a generic electric vehicle powertrain suitable under variable frequency of averaging developed f or remote operability," *IET Electrical Systems in Transportation*, vol. 10, no. 3, pp. 268–274, 2020.

[26] K. J. Prasad Veeramraju, J. A. Mueller, and J. W. Kimball, "An extended generalized average modeling framework for power converters," *IEEE Transactions on Power Electronics*, pp. 1–13, 2023.

[27] K. J. Prasad Veeramraju and J. W. Kimball, "Multidimensional extensions to generalized averaged models for multi-frequency-excited dynamic systems," in *2021 IEEE 22nd Workshop on Control and Modelling of Power Electronics (COMPEL)*, 2021, pp. 1–8.

[28] S. Sanders, J. Noworolski, X. Liu, and G. Verghese, "Generalized averaging method for power conversion circuits," *IEEE Transactions on Power Electronics*, vol. 6, no. 2, pp. 251–259, 1991.

[29] V. Caliskan, O. Verghese, and A. Stankovic, "Multifrequency averaging of dc/dc converters," *IEEE Transactions on Power Electronics*, vol. 14, no. 1, pp. 124–133, 1999.

[30] A. V. Oppenheim, A. S. Willsky, and S. H. Nawab, *Signals & Systems (2nd Ed.)*. USA: Prentice-Hall, Inc., 1996.

[31] P. Shamsi, "Extended averaging method for power supply systems with multiple switching frequencies," in *2014 IEEE Applied Power Electronics Conference and Exposition - APEC 2014*, 2014, pp. 2842–2846.

[32] K. J. P. Veeramraju and J. Kimball, "EGAMToolbox," Apr. 2023. [Online]. Available: https://github.com/KartikeyaVeeramraju/EGAMToolbox

[33] J. Xu, H. Qian, Y. Hu, S. Bian, and S. Xie, "Overview of sogi-based single-phase phase-locked loops for grid synchronization under complex grid conditions," *IEEE Access*, vol. 9, pp. 39 275–39 291, 2021.

SECTION

2. CONCLUSIONS AND FUTURE WORK

2.1. CONCLUSIONS

In this work, a novel solid-state transformer topology is investigated. The work first investigates different types of SSTs and their configurations. Then a new type of Type A SST based on the Dual Active Bridge (DAB) converter is proposed. The phase shift between the primary and secondary bridge serves as the parameter that controls the power flow between the primary and secondary sides. The phase shift required by the DAB to transfer the instantaneous power is solved as quadratic equations. Also, a soft switching algorithm is developed for all voltage and current combinations. The ac-ac DAB hardware prototype with integrated leakage inductance transformer is tested for power transfer in both directions. Also, the reactive power flow is tested using the derived solutions.

As the ac-ac DAB converter has multi-frequency interactions, a need for a new generalized average modeling framework is recognized and proposed. The 2D convolution-based Extended Generalized Average Modeling (EGAM) framework is proved to be a viable technique after validating its capability to model the multiple frequency interactions in a sine pulse width modulated single-phase inverter. The model matching is rigorously verified on both simulation and hardware fronts, where excellent model matching with EGAM models is observed.

The EGAM technique is then finally applied to an ac-ac DAB converter and its correctness is tested against simulation and hardware fronts. Excellent matching between EGAM and PLECS simulated waveforms is observed when higher-order switching harmonics are included, proving the power transfer in multiple harmonics of the switching frequency. The Fourier decomposition of the state variables shows that the grid side dynamic components

predominantly see the grid harmonics, which is expected. The leakage inductor current, on the other hand, is seen not to have a switching frequency harmonic; rather, it is observed to have the grid and switching frequency side band harmonics. This phenomenon is further clarified when the leakage inductor current waveform in the ac-ac DAB is seen as an amplitude-modulated waveform, which is known to have sideband harmonics of the two exciting frequencies.

2.2. FUTURE WORK

Although the ac-ac DAB is shown to have many attractive features, the study assumes the integration of two grids with same voltage, phase and frequency. Violating any of these aforementioned grid parameters significantly complicates the power transfer mechanism in the standard ac-ac DAB. Additionally, the zero-voltage crossover regions in the ac-ac DAB cause current harmonics at twice the grid frequency. Due to these problems, improvements on the ac-ac DAB topology must be proposed.

One reason for the above-mentioned problems is the lack of energy storage in the ac-ac DAB. Off late, Multi-Active Bridges (MABs) are being proposed for integrating many dc sources with a single high-frequency multi winding-transformer. One subset of the MABs: a Triple Active Bridge (TAB) may serve as a candidate topology for addressing the issues of the ac-ac DAB topology in future research works. The TAB interfaces two ac ports and one dc port with a three-winding transformer. The phase deployment at the two bridges and the H-bridge voltage pulse width modulation can be calculated to meet the instantaneous power waveforms at each port. This should be accomplished by either conventional root-finding techniques that model the power flow mechanisms or by machine learning algorithms. It is realized that for future-generation power converters, higher computational capacities may be necessary to run the advanced algorithms needed to realize power flow.

The EGAM framework proposed in this work excellently captures the dynamic phenomenon involving two-frequency excited systems. The EGAM framework directly leads to large signal models of the converters. In future, techniques need to be devised in order to simplify these complicated models into simpler forms that enable power designers to form simpler reduced-order models and small-signal models necessary to use classical control techniques.

APPENDIX

1. 2D DFI CONVOLUTION

This section provides the proof for Corollary 3.2. But before starting with the actual proof for the corollary, some important identities and functions are given for clarity.

1.1. AN INTEGRAL IDENTITY

$$\int_{-\pi}^{\pi}\int_{-\pi}^{\pi}\sum_{p,q\in\mathbb{Z}}\sum_{r,s\in\mathbb{Z}} e^{j(k_1\omega_1 t+k_2\omega_2 t)}\, d\omega_1 t\, d\omega_2 t = \begin{cases} 4\pi^2 & k_1=0, k_2=0 \\ 0 & k_1=0, k_2\in\mathbb{Z} \\ 0 & k_1\in\mathbb{Z}, k_2=0 \\ 0 & k_1\in\mathbb{Z}, k_2\in\mathbb{Z} \end{cases} \tag{1}$$

1.2. TWO-DIMENSIONAL SIFTING PROPERTY

$$x(n_1,n_2)=\sum_{k_1=-\infty}^{\infty}\sum_{k_2=-\infty}^{\infty} x(k_1,k_2)\delta(n_1-k_1,n_2-k_2) \tag{2}$$

1.3. MULTIDIMENSIONAL DISCRETE CONVOLUTION

$$\begin{aligned} x(n_1,n_2,\cdots,n_M) *^{M}\cdots* h(n_1,n_2,\cdots,n_M) \triangleq \\ \sum_{k_1=-\infty}^{\infty}\sum_{k_2=-\infty}^{\infty}\cdots\sum_{k_M=-\infty}^{\infty} h(k_1,k_2,\cdots,k_M) \\ x(n_1-k_1,n_2-k_2,\cdots,n_M-k_M) \end{aligned} \tag{3}$$

1.4. DOUBLE FOURIER SERIES SIGNALS

$$x(\omega_1 t, \omega_2 t) = \sum_{j,k \in \mathbb{Z}} a_{j,k} e^{i(m\omega_1 t + n\omega_2 t)} \tag{4}$$

$$y(\omega_1 t, \omega_2 t) = \sum_{j,k \in \mathbb{Z}} b_{j,k} e^{i(m\omega_1 t + n\omega_2 t)} \tag{5}$$

1.5. FOURIER COEFFICIENTS IN 2D

$$\overline{C}_{mn} = \frac{1}{4\pi^2} \int_{-\pi}^{\pi} \int_{-\pi}^{\pi} f(p,q)\, e^{-j(mp+nq)}\, dp\, dq \tag{6}$$

Proof

$$\overline{C}_{mn} = \frac{1}{4\pi^2} \int_{-\pi}^{\pi} \int_{-\pi}^{\pi} x(\omega_1 t, \omega_2 t) y(\omega_1 t, \omega_2 t)\, e^{-j(m\omega_1 t + n\omega_2 t)}\, d\omega_1 t\, d\omega_2 t$$

$$= \frac{1}{4\pi^2} \int_{-\pi}^{\pi} \int_{-\pi}^{\pi} \sum_{p,q \in \mathbb{Z}} a_{p,q} e^{j(p\omega_1 t + q\omega_2 t)} \sum_{r,s \in \mathbb{Z}} b_{r,s} e^{j(r\omega_1 t + s\omega_2 t)}\ e^{-j(m\omega_1 t + n\omega_2 t)}\, d\omega_1 t\, d\omega_2 t$$

$$= \frac{1}{4\pi^2} \sum_p \sum_q \sum_r \sum_s a_{p,q} b_{r,s} \int_{-\pi}^{\pi} \int_{-\pi}^{\pi} e^{-j((m-p-r)\omega_1 t + (n-q-s)\omega_2 t)}\, d\omega_1 t\, d\omega_2 t$$

$$\overset{(1)}{=} \sum_p \sum_q \sum_r \sum_s a_{p,q} b_{r,s}\, \delta((m-p)-r, (n-q)-s)$$

$$= \sum_p \sum_q a_{p,q} \sum_r \sum_s b_{r,s}\, \delta((m-p)-r, (n-q)-s)$$

$$\overset{(2)}{=} \sum_p \sum_q a_{p,q} b_{m-p,n-q}$$

$$\overline{C}_{mn} \overset{(3)}{=} a ** b$$

1.6. EGAM TOOLBOX

A toolbox is developed for MATLAB to perform the EGAM simulations for power converters and is shared as a GitHub project (`https://github.com/KartikeyaVeeramraju/EGAMToolbox.git`). The toolbox includes functions for applying the 2D convolution algorithm for ODE solvers.

REFERENCES

[1] X. She, A. Q. Huang, and R. Burgos, "Review of solid-state transformer technologies and their application in power distribution systems," *IEEE Journal of Emerging and Selected Topics in Power Electronics*, vol. 1, no. 3, pp. 186–198, 2013.

[2] J. Falck, C. Felgemacher, A. Rojko, M. Liserre, and P. Zacharias, "Reliability of power electronic systems: An industry perspective," *IEEE Industrial Electronics Magazine*, vol. 12, no. 2, pp. 24–35, 2018.

[3] "Energy conservation program: Energy conservation standards for distribution transformers," Office of Energy Efficiency and Renewable Energy, Department of Energy, Standard, Oct. 2007.

[4] F. Bignucolo, M. Bertoluzzo, and C. Fontana, "Applications of the solid state transformer concept in the electrical power system," in *2015 AEIT International Annual Conference (AEIT)*, 2015, pp. 1–6.

[5] Q. Zhu, L. Wang, D. Chen, L. Zhang, and A. Q. Huang, "Design and implementation of a 7.2kv single stage ac-ac solid state transformer based on current source series resonant converter and 15 kv sic mosfet," in *2017 IEEE Energy Conversion Congress and Exposition (ECCE)*, 2017, pp. 1288–1295.

[6] F. Ruiz, M. A. Perez, J. R. Espinosa, T. Gajowik, S. Stynski, and M. Malinowski, "Surveying solid-state transformer structures and controls: Providing highly efficient and controllable power flow in distribution grids," *IEEE Industrial Electronics Magazine*, vol. 14, no. 1, pp. 56–70, 2020.

[7] H. Chen and D. Divan, "Soft-switching solid-state transformer (s4t)," *IEEE Transactions on Power Electronics*, vol. 33, no. 4, pp. 2933–2947, 2018.

[8] R. Rahmoun and M. Patt, "High efficiency single-phase dual-active-bridge ac/ac converter," in *2019 21st European Conference on Power Electronics and Applications (EPE '19 ECCE Europe)*, 2019, pp. P.1–P.10.

[9] K. Mohapatra and N. Mohan, "Matrix converter fed open-ended power electronic transformer for power system application," in *2008 IEEE Power and Energy Society General Meeting - Conversion and Delivery of Electrical Energy in the 21st Century*, 2008, pp. 1–6.

[10] H. Keyhani, H. A. Toliyat, M. Harfman-Todorovic, R. Lai, and R. Datta, "An isolated resonant ac-link three-phase ac–ac converter using a single hf transformer," *IEEE Transactions on Industrial Electronics*, vol. 61, no. 10, pp. 5174–5183, 2014.

[11] K. Basu, A. Shahani, A. K. Sahoo, and N. Mohan, "A single-stage solid-state transformer for pwm ac drive with source-based commutation of leakage energy," *IEEE Transactions on Power Electronics*, vol. 30, no. 3, pp. 1734–1746, 2015.

[12] A. Sharma, K. J. P. Veeramraju, and J. W. Kimball, "Power flow control of a single-stage ac-ac solid-state transformer for ac distribution system," in *2022 IEEE Power and Energy Conference at Illinois (PECI)* [Accepted], 2022.

[13] M. A. Hannan, P. J. Ker, M. S. H. Lipu, Z. H. Choi, M. S. A. Rahman, K. M. Muttaqi, and F. Blaabjerg, "State of the art of solid-state transformers: Advanced topologies, implementation issues, recent progress and improvements," *IEEE Access*, vol. 8, pp. 19 113–19 132, 2020.

[14] A. Prasai, H. Chen, R. Moghe, Z. Wolanski, K. Chintakrinda, A. Zhou, J. C. Llambes, and D. Divan, "Dyna-c: Experimental results for a 50 kva 3-phase to 3-phase solid state transformer," in *2014 IEEE Applied Power Electronics Conference and Exposition - APEC 2014*, 2014, pp. 2271–2277.

[15] H. Qin and J. W. Kimball, "Solid-state transformer architecture using ac–ac dual-active-bridge converter," *IEEE Transactions on Industrial Electronics*, vol. 60, no. 9, pp. 3720–3730, 2013.

[16] ——, "Generalized average modeling of dual active bridge dc–dc converter," *IEEE Transactions on Power Electronics*, vol. 27, no. 4, pp. 2078–2084, 2012.

[17] S. Sanders, J. Noworolski, X. Liu, and G. Verghese, "Generalized averaging method for power conversion circuits," *IEEE Transactions on Power Electronics*, vol. 6, no. 2, pp. 251–259, 1991.

[18] J. Mahdavi, A. Emaadi, M. Bellar, and M. Ehsani, "Analysis of power electronic converters using the generalized state-space averaging approach," *IEEE Transactions on Circuits and Systems I: Fundamental Theory and Applications*, vol. 44, no. 8, pp. 767–770, 1997.

[19] X. Liu, A. M. Cramer, and F. Pan, "Generalized average method for time-invariant modeling of inverters," *IEEE Transactions on Circuits and Systems I: Regular Papers*, vol. 64, no. 3, pp. 740–751, 2017.

[20] K. J. Prasad Veeramraju and J. W. Kimball, "Multidimensional extensions to generalized averaged models for multi-frequency-excited dynamic systems," in *2021 IEEE 22nd Workshop on Control and Modelling of Power Electronics (COMPEL)*, 2021, pp. 1–8.

[21] J. Ai-juan, L. Hang-tian, and L. Shao-long, "A new matrix type three-phase four-wire power electronic transformer," in *2006 37th IEEE Power Electronics Specialists Conference*, 2006, pp. 1–6.

[22] M. Sabahi, A. Y. Goharrizi, S. H. Hosseini, M. B. B. Sharifian, and G. B. Gharehpetian, "Flexible power electronic transformer," *IEEE Transactions on Power Electronics*, vol. 25, no. 8, pp. 2159–2169, 2010.

[23] E. Ronan, S. Sudhoff, S. Glover, and D. Galloway, "A power electronic-based distribution transformer," *IEEE Transactions on Power Delivery*, vol. 17, no. 2, pp. 537–543, 2002.

[24] S. Bhattacharya, T. Zhao, G. Wang, S. Dutta, S. Baek, Y. Du, B. Parkhideh, X. Zhou, and A. Q. Huang, "Design and development of generation-i silicon based solid state transformer," in *2010 Twenty-Fifth Annual IEEE Applied Power Electronics Conference and Exposition (APEC)*, 2010, pp. 1666–1673.

[25] D. Gonzalez-Agudelo, A. Escobar-Mejía, and H. Ramirez-Murrillo, "Dynamic model of a dual active bridge suitable for solid state transformers," in *2016 13th International Conference on Power Electronics (CIEP)*, 2016, pp. 350–355.

[26] H. Qin and J. W. Kimball, "Ac-ac dual active bridge converter for solid state transformer," in *2009 IEEE Energy Conversion Congress and Exposition*, 2009, pp. 3039–3044.

[27] G. G. Facchinello, L. L. Brighenti, S. L. Brockveld, D. C. Martins, and W. M. Dos Santos, "Closed-loop operation and control strategy for the dual active half bridge ac-ac converter," in *2017 IEEE 8th International Symposium on Power Electronics for Distributed Generation Systems (PEDG)*, 2017, pp. 1–7.

[28] K. J. Veeramraju, A. Sharma, and J. W. Kimball, "A comprehensive analysis on complex power flow mechanism in an ac-ac dual active bridge," in *2022 IEEE Power and Energy Conference at Illinois (PECI)*, 2022, pp. 1–6.

[29] G. Venkataramanan and N. Kogalur, "A hybrid 4-quadrant switch for ac power conversion," in *2019 IEEE Energy Conversion Congress and Exposition (ECCE)*, 2019, pp. 5487–5493.

[30] Magnetics inc. p-type material. [Online]. Available: https://www.mag-inc.com/Products/Ferrite-Cores/P-Materialhttp://link.com

[31] A. Sharma and J. W. Kimball, "Transformer leakage inductance design methodology," in *2023 IEEE Applied Power Electronics Conference and Exposition (APEC)*, 2023, pp. 1572–1578.

[32] J. Xu, H. Qian, Y. Hu, S. Bian, and S. Xie, "Overview of sogi-based single-phase phase-locked loops for grid synchronization under complex grid conditions," *IEEE Access*, vol. 9, pp. 39 275–39 291, 2021.

[33] V. Caliskan, O. Verghese, and A. Stankovic, "Multifrequency averaging of dc/dc converters," *IEEE Transactions on Power Electronics*, vol. 14, no. 1, pp. 124–133, 1999.

[34] H. Alrajhi, "A generalized state space average model for parallel dc-to-dc converters," *Computer Systems Science and Engineering*, vol. 41, no. 2, pp. 717–734, 2022.

[35] M. Monika, M. Rane, S. Wagh, A. Stanković, and N. Singh, "Development of dynamic phasor based higher index model for performance enhancement of dual active bridge," *Electric Power Systems Research*, vol. 168, pp. 305–312, 2019.

[36] G. Brando, A. Del Pizzo, and S. Meo, "Model-reference adaptive control of a dual active bridge dc-dc converter for aircraft applications," in *2018 International Symposium on Power Electronics, Electrical Drives, Automation and Motion (SPEEDAM)*, 2018, pp. 502–506.

[37] M. Berger, I. Kocar, H. Fortin-Blanchette, and C. Lavertu, "Hybrid average modeling of three-phase dual active bridge converters for stability analysis," *IEEE Transactions on Power Delivery*, vol. 33, no. 4, pp. 2020–2029, 2018.

[38] Z. U. Zahid, Z. M. Dalala, C. Zheng, R. Chen, W. E. Faraci, J.-S. J. Lai, G. Lisi, and D. Anderson, "Modeling and control of series–series compensated inductive power transfer system," *IEEE Journal of Emerging and Selected Topics in Power Electronics*, vol. 3, no. 1, pp. 111–123, 2015.

[39] H. Fang, H. Xiang, S. Li, Y. Xin, J. Zhou, and Y. Wang, "Dynamic phasor modeling of mmc-hvdc systems," in *2022 IEEE 5th International Conference on Information Systems and Computer Aided Education (ICISCAE)*, 2022, pp. 988–995.

[40] O. C. Sakinci and J. Beerten, "Generalized dynamic phasor modeling of the mmc for small-signal stability analysis," *IEEE Transactions on Power Delivery*, vol. 34, no. 3, pp. 991–1000, 2019.

[41] A. Francés, R. Asensi, O. García, R. Prieto, and J. Uceda, "Modeling electronic power converters in smart dc microgrids—an overview," *IEEE Transactions on Smart Grid*, vol. 9, no. 6, pp. 6274–6287, 2018.

[42] S. K. Gurumurthy, M. Mirz, B. S. Amevor, F. Ponci, and A. Monti, "Hybrid dynamic phasor modeling approaches for accurate closed-loop simulation of power converters," *IEEE Access*, vol. 10, pp. 101 643–101 655, 2022.

[43] A. Nazari, Y. Xue, J. K. Motwani, I. Cvetkovic, D. Dong, and D. Boroyevich, "Dynamic phasor modeling of three phase voltage source inverters," in *2021 6th IEEE Workshop on the Electronic Grid (eGRID)*, 2021, pp. 1–6.

[44] U. C. Nwaneto and A. M. Knight, "Dynamic phasor-based modeling and simulation of a reduced-order single-phase inverter in voltage-controlled and current-controlled modes," in *2020 IEEE Texas Power and Energy Conference (TPEC)*, 2020, pp. 1–6.

[45] ——, "Dynamic phasor-based modeling and simulation of a single-phase diode-bridge rectifier," *IEEE Transactions on Power Electronics*, vol. 38, no. 4, pp. 4921–4936, 2023.

[46] Z. Shuai, Y. Peng, J. M. Guerrero, Y. Li, and Z. J. Shen, "Transient response analysis of inverter-based microgrids under unbalanced conditions using a dynamic phasor model," *IEEE Transactions on Industrial Electronics*, vol. 66, no. 4, pp. 2868–2879, 2019.

[47] A. Bendib, A. Kherbachi, A. Chouder, H. Ahmed, and K. Kara, "Advanced control scheme and dynamic phasor modelling of grid-tied droop-controlled inverters," *IET Renewable Power Generation*, vol. n/a, no. n/a. [Online]. Available: https://ietresearch.onlinelibrary.wiley.com/doi/abs/10.1049/rpg2.12610

[48] J. A. Mueller and J. W. Kimball, "An improved generalized average model of dc–dc dual active bridge converters," *IEEE Transactions on Power Electronics*, vol. 33, no. 11, pp. 9975–9988, 2018.

[49] K. J. Veeramraju, A. Sharma, and J. W. Kimball, "A comprehensive analysis on complex power flow mechanism in an ac-ac dual active bridge," in *2022 IEEE Power and Energy Conference at Illinois (PECI)*, 2022, pp. 1–6.

[50] A. Sharma, K. J. Veeramraju, and J. W. Kimball, "Power flow control of a single-stage ac-ac solid-state transformer for ac distribution system," in *2022 IEEE Power and Energy Conference at Illinois (PECI)*, 2022, pp. 1–6.

[51] H. Qin and J. W. Kimball, "Solid-state transformer architecture using ac–ac dual-active-bridge converter," *IEEE Transactions on Industrial Electronics*, vol. 60, no. 9, pp. 3720–3730, 2013.

[52] X. Liu, A. M. Cramer, and F. Pan, "Generalized average method for time-invariant modeling of inverters," *IEEE Transactions on Circuits and Systems I: Regular Papers*, vol. 64, no. 3, pp. 740–751, 2017.

[53] X. Liu and A. M. Cramer, "Three-phase inverter modeling using multifrequency averaging with third harmonic injection," in *2016 IEEE Energy Conversion Congress and Exposition (ECCE)*, 2016, pp. 1–6.

[54] S. Sen, P. L. Evans, and C. Mark Johnson, "Multi-frequency averaging (mfa) model of a generic electric vehicle powertrain suitable under variable frequency of averaging developed f or remote operability," *IET Electrical Systems in Transportation*, vol. 10, no. 3, pp. 268–274, 2020.

[55] S. Sen, P. L. Evans, and C. M. Johnson, "Multi-frequency averaging (mfa) model of electric-hybrid powertrain suitable for variable frequency operation applied in geographically-distributed power hardware-in-the-loop (gd-phil) simulation," in *2018 IEEE Vehicle Power and Propulsion Conference (VPPC)*, 2018, pp. 1–6.

[56] A. V. Oppenheim, A. S. Willsky, and S. H. Nawab, *Signals & Systems (2nd Ed.)*. USA: Prentice-Hall, Inc., 1996.

[57] P. Shamsi, "Extended averaging method for power supply systems with multiple switching frequencies," in *2014 IEEE Applied Power Electronics Conference and Exposition - APEC 2014*, 2014, pp. 2842–2846.

[58] X. Liu, "Improvements in inverter modeling and control," Ph.D. dissertation, University of Kentucky, 2017.

[59] K. J. Prasad Veeramraju and J. W. Kimball, "Multidimensional extensions to generalized averaged models for multi-frequency-excited dynamic systems," in *2021 IEEE 22nd Workshop on Control and Modelling of Power Electronics (COMPEL)*, 2021, pp. 1–8.

[60] K. J. Prasad Veeramraju, J. A. Mueller, and J. W. Kimball, "An extended generalized average modeling framework for power converters," *IEEE Transactions on Power Electronics*, pp. 1–13, 2023.

[61] K. J. P. Veeramraju and J. Kimball, "EGAMToolbox," Apr. 2023. [Online]. Available: https://github.com/KartikeyaVeeramraju/EGAMToolbox

VITA

Kartikeya Jayadurga Prasad Veeramraju earned his B.Tech in Electrical and Electronics Engineering from Kakatiya University, India, in 2017 and his MS in Electrical Engineering from Missouri University of Science and Technology, Rolla, MO, in 2020. In July 2023, he received his PhD in Electrical Engineering from Missouri University of Science and Technology. His research interests included the design, modeling, and embedded control of power converters, microgrids, EV chargers, and high-voltage aerospace power converters. He was a key member of the Missouri S&T satellite team, where he developed power converters for satellites. Additionally, he worked as a graduate teaching assistant, teaching power systems and electromechanics laboratory courses to undergraduate students while at Missouri S&T.